WHC-EP--0042

DE90 007935

PORFLO-3: A Mathematical Model for Fluid Flow, Heat, and Mass Transport in Variably Saturated Geologic Media

Theory and Numerical Methods, Version 1.0

B. Sagar
Pacific Northwest Laboratory

A. K. Runchal
Analytic and Computational Research, Inc.

Date Published
March 1990

Prepared for the U.S. Department of Energy
Assistant Secretary for Environment, Safety and Health

Westinghouse Hanford Company
P.O. Box 1970
Richland, Washington 99352

Hanford Operations and Engineering Contractor for the
U.S. Department of Energy under Contract DE-AC06-87RL10930

Available from
U.S. Department of Commerce
National Technical Information Service
5285 Port Royal Road
Springfield, VA 22161

NTIS Price Codes:

Microfiche Copy: A01

Printed Copy:

Pages	Price Codes	Pages	Price Codes
001-025	A02	301-325	A14
026-050	A03	326-350	A15
051-075	A04	351-375	A16
076-100	A05	376-400	A17
101-125	A06	401-425	A18
126-150	A07	426-450	A19
151-175	A08	451-475	A20
176-200	A09	476-500	A21
201-225	A10	501-525	A22
226-250	A11	526-550	A23
251-275	A12	551-575	A24
276-300	A13	576-600	A25

Printed in the United States of America

DISCLM-1 CHP (2-89)

RECORD OF REVISION	(1) Document Number WHC-EP-0042	Page 1 of 1

(2) Title

PORFLO-3: A Mathematical Model for Fluid Flow, Heat, and Mass Transport in Variably Saturated Geologic Media -- Theory and Numerical Methods, Version 1.0

CHANGE CONTROL RECORD

(3) Revision	(4) Description of Change – Replace, Add, and Delete Pages	Authorized for Release		
		(5) Cog./Proj. Engr.	(6) Cog./Proj. Mgr.	Date
1	(7) Delete, add, and rearrange paragraphs 2 & 3 of Section 1.1 of p.1-1.	J. D. Davis	J W Cammann	4/7/90

ABSTRACT

This computer program was developed in support of environmental remediation activities being conducted at the Hanford Site to comply with the Resource Conservation and Recovery Act of 1976; the Comprehensive Environmental Response, Compensation and Liability Act of 1980; and the Hanford Federal Facility Agreement and Consent Order (Ecology et al. 1989).* The results of analyses made using the computer program will be used in remedial investigations and feasibility studies and to predict the environmental consequences associated with evaluating alternative remediation methods.

This document provides details of the theory of the PORFLO-3 computer program. Instructions for using the computer program are available in a companion volume.**

PORFLO-3 is based on a mathematical formulation of the processes of fluid flow, heat transfer, and mass transport in variably saturated geologic media. The geologic media may be heterogeneous and anisotropic and may contain linear and planar features such as boreholes and fractures. The program can be used to analyze three-dimensional problems involving partially and fully saturated media with various types of fluid, heat, and mass sources. However, Version 1 is limited to the analysis of a single fluid.

The three partial differential equations that govern fluid flow, heat transfer, and mass transport through porous media are derived in Chapter 3.0. Assumptions are stated to make obvious the limitations on the applicability of these equations. Application of the method of "Nodal Point Integration" to obtain discrete analogues of the governing equations is discussed in Chapter 4.0. The various methods employed to solve the discrete analogues also are discussed in Chapter 4.0.

Two applications of PORFLO-3 to realistic problems are given in Chapter 5.0. The first problem tracks three-dimensional transient plumes of contaminated groundwater from a distributed, time-dependent source. The second application is for unsaturated flow in geologic media intersected by a fault that is included as a planar feature in the model.

Keywords: Variably Saturated Flow, Heat and Mass Transport in Porous Media, Three-dimensional Modeling, Numerical Modeling, Fracture Flow Modeling.

---

*Ecology, EPA, and DOE, 1989, *Hanford Federal Facility Agreement and Consent Order*, Washington State Department of Ecology, U.S. Environmental Protection Agency, and U.S. Department of Energy, Olympia, Washington.

**Runchal, A. K. and B. Sagar, 1989, *PORFLO-3: A Mathematical Model for Fluid Flow, Heat, and Mass Transport in Variably Saturated Geologic Media: Users Manual, Version 1.0*, WHC-EP-0041, Westinghouse Hanford Company, Richland, Washington.

ACKNOWLEDGMENT

Several individuals have contributed to the development of the PORFLO-3 software package. These include many users who provided suggestions for improving the computer program. We believe that such improvements have enhanced the utility of this software package. Specifically, we are grateful to Dr. Jerry D. Davis of Westinghouse Hanford Company who provided invaluable support throughout the development process and detailed critique of this document. We are also thankful to Mike P. Connelly (Westinghouse Hanford Company), Mark L. Rockhold (Pacific Northwest Laboratory), and John L. Smoot (Pacific Northwest Laboratory) for the example simulations included in Chapter 5.0.

CONTENTS

FIGURES

TABLES

MATHEMATICAL NOTATION

All symbols are defined where they first occur in the text. Definitions of the important symbols are listed below to facilitate easy reference.

Symbol	Meaning	Dimensions	SI units[a]	FPS units[b]
B	Buoyancy parameter	----	----	----
c_f	Specific heat of fluid	$L^2\ t^{-2}\ T^{-1}$	J/(kg•K)	Btu/(lbm°F)
c_s	Specific heat of solid	$L^2\ t^{-2}\ T^{-1}$	J/(kg•K)	Btu/(lbm°F)
C	Species concentration in fluid	$M\ L^{-3}$	kg/m^3	lbm/ft^3
C_e	Species concentration in fluid+solid matrix	$M\ L^{-3}$	kg/m^3	lbm/ft^3
C_s	Species concentration in solid	$M\ L^{-3}$	kg/m^3	lbm/ft^3
$\underset{\approx}{D}$	Dispersion tensor	$L^2\ t^{-1}$	m^2/s	ft^2/s
D_M	Molecular diffusivity	$L^2\ t^{-1}$	m^2/s	ft^2/s
e	Internal energy of fluid	$L^2\ t^{-2}$	J/kg	Btu/lbm
e_e	Equivalent internal energy of fluid+solid matrix	$L^2\ t^{-2}$	J/kg	Btu/lbm
F	State variable (P, T, or C)	----- Variable dependent -----		
g	Gravitational acceleration	$L\ t^{-2}$	m/s^2	ft/s^2
$\vec{J}_C$	Species diffusional flux	$M\ L^{-2}\ t^{-1}$	$kg/(m^2•s)$	$lbm/(ft^2•s)$
$\vec{J}_D$	Species dispersive flux	$M\ L^{-2}\ t^{-1}$	$kg/(m^2•s)$	$lbm/(ft^2•s)$
$\underset{\approx}{k}$	Intrinsic permeability tensor	L^2	m^2	ft^2
k_r	Relative intrinsic permeability	L^2	m^2	ft^2
k_f	Thermal fluid conductivity	$M\ L\ t^{-3}\ T^{-1}$	W/(m°K)	BTU/(ft•s°F)
k_e	Effective thermal conductivity of fluid+solid matrix	$M\ L\ t^{-3}\ T^{-1}$	W/(m•K)	Btu/(ft•s°F)
k_s	Solid thermal conductivity	$M\ L\ t^{-3}\ T^{-1}$	W/(m•K)	Btu/(ft•s°F)
k_d	Sorption coefficient	$M^{-1}\ L^3$	m^3/kg	ft^3/lbm
$\underset{\approx}{K}$	Hydraulic conductivity tensor	$L\ t^{-1}$	m/s	ft/s
m	Rate of injection of fluid	$M\ L^{-3}\ t^{-1}$	$kg/(m^3•s)$	$lbm/(ft^3•s)$
m_v	Fluid injection rate	t^{-1}	$m^3/(m^3•s)$	$ft^3/(ft^3•s)$
n_E	Effective or flow porosity	----	----	----
n_D	Diffusive or connected porosity	----	----	----
n_T	Total porosity	----	----	----
N	Normal coordinate	L	m	ft
p	Thermodynamic pressure	$M\ L^{-1}\ t^{-2}$	N/m^2	lbf/ft^2
P	Pressure head at reference fluid density	L	m	ft

MATHEMATICAL NOTATION (Continued)

Symbol	Meaning	Dimensions	SI units[a]	FPS units[b]
$\vec{q}_D$	Dispersive energy flux	$M\ t^{-3}$	$W/(m^2)$	$Btu/(ft^2 \cdot s)$
$\vec{q}_T$	Conductive energy flux	$M\ t^{-3}$	$W/(m^2)$	$Btu/(ft^2 \cdot s)$
r	Radial coordinate	L	m	ft
R	Density ratio	----	----	----
R_d	Retardation factor	----	----	----
S	Area of a bounding surface	L^2	m^2	ft^2
S_C	Injection rate of species	$M\ L^{-3}\ t^{-1}$	$kg/(m^3 \cdot s)$	$lbm/ft^3 \cdot s)$
S_S	Specific storativity	L^{-1}	$1/m$	$1/ft$
S_T	Injection rate of heat	$M\ L^{-1}\ t^{-3}$	$W/(m^3)$	$Btu/(ft^3 \cdot s)$
t	Time	t	s	s
T	Thermodynamic temperature	T	K	$°F$
T_c	Critical temperature	T	K	$°F$
U	Darcy velocity in x- or r-direction	$L\ t^{-1}$	m/s	ft/s
V	Darcy velocity in y- or θ-direction	$L\ t^{-1}$	m/s	ft/s
$\vec{V}$	Total velocity vector	$L\ t^{-1}$	m/s	ft/s
V	Volume	L^3	m^3	ft/s
W	Darcy velocity in z-direction	$L\ t^{-1}$	m/s	ft/s
x	x coordinate	L	m	ft
y	y coordinate	L	m	ft
z	z coordinate	L	m	ft

Greek Symbol	Meaning	Dimensions	SI units[a]	FPS units[b]
α_f	Fluid compressibility	$M^{-1}\ L\ t^2$	m^2/N	ft^2/lbf
α_S	Solid compressibility	$M^{-1}\ L\ t^2$	m^2/N	ft^2/lbf
α_L	Longitudinal dispersivity	L	m	ft
α_T	Transverse dispersivity	L	m	ft
β_f	Thermal expansion coefficient for fluid	T^{-1}	$1/K$	$1/°F$
μ	Dynamic viscosity of fluid	$M\ L^{-1}\ t^{-1}$	$kg/(m \cdot s)$	$lbm/(ft \cdot s)$
ρ	Density of fluid	$M\ L^{-3}$	kg/m^3	lbm/ft^3
ρ_S	Density of solid	$M\ L^{-3}$	kg/m^3	lbs/ft^3
θ	Volumetric moisture content	----	----	----
∂	Partial derivative	----	----	----
$\vec{\nabla}$	Gradient operator	----	----	----

MATHEMATICAL NOTATION (Continued)

q	Soil-water potential	L	m	ft
λ	Radioactive decay coefficient	t^{-1}	s^{-1}	s^{-1}
η	porosity	----	----	----

Superscripts & Subscripts	Meaning
e	Equivalent or effective value of a soil matrix property
s	Pertaining to the solid phase
x	Pertaining to x-direction
y	Pertaining to y-direction
z	Pertaining to z-direction
t	Pertaining to time
$\approx$	Tensor or matrix
*	Pertaining to a reference state of the system
$\rightarrow$	Vector

[a]SI = International System of Units.
[b]FPS = Foot, Pound, Second Units.

1.0 INTRODUCTION

1.1 MOTIVATION FOR MODEL DEVELOPMENT

Discharging radioactive and chemical wastes to the subsurface has been a widespread and common waste disposal practice at U.S. Department of Energy (DOE) installations. Some of the discharges of wastes have been planned; others have been accidental. Needs have been identified for future discharges. For example, future disposal of commercially derived, high-level nuclear wastes is planned at the Yucca Mountain Site in southern Nevada. Disposal of low-level radioactive and mixed (radioactive and chemical) wastes is planned at the Hanford Site in south-central Washington State and at other DOE sites.

To evaluate the safety of the proposed actions and the effectiveness of methods slated for cleanup of sites contaminated by past disposal practices, predictions of the future performance of waste isolation systems must be made. Mathematical models are analytical tools used to make these predictions and evaluations. The PORFLO-3 is one such mathematical model, the theory of which is the subject of this report.

This computer program was developed in support of environmental remediation activities being conducted at the Hanford Site to comply with the Resource Conservation and Recovery Act of 1976; the Comprehensive Environmental Response, Compensation and Liability Act of 1980; and the Hanford Federal Facility Agreement and Consent Order. The results of analyses made using the computer program will be used in remedial investigations and feasibility studies and to predict the environmental consequences of alternative remediation methods.

The current and earlier versions of the PORFLO software were developed by Analytic and Computational Research, Inc., (ACRI) under contract to Rockwell Hanford Operations and its successor, Westinghouse Hanford Company, the current operating contractor of the Hanford Site for the DOE (Runchal et al. 1985; Kline et al. 1983; Eyler and Budden 1984; Sagar and Runchal 1989). The objective of the development work was to achieve the ability to assess the performance of nuclear and hazardous chemical waste disposal facilities and remediation programs to prevent contamination of soil and groundwater that could be harmful to the environment and human health.

On October 26, 1989, the DOE granted a request by ACRI that title to the copyright of PORFLO-3 be waived by the DOE to allow ACRI to claim that right to all versions of PORFLO-3 developed with DOE support. In accordance with the conditions of release, ACRI has deposited read-only copies of each version of the software with the National Energy Software Center, Argonne National Laboratory, Argonne, Illinois. The U.S. Government retains a paid-up, nonexclusive, irrevocable worldwide license for use by the government.

The Hanford Site, located in south-central Washington, has been dedicated to nuclear research and defense materials production, nuclear materials processing, and storage and disposal of nuclear and chemical process wastes since the early 1940's. During this time, the chemical processing of spent nuclear fuel for the recovery of plutonium, uranium, and neptunium has

produced the world's largest identified inventory of defense-related waste. This waste contains fission products, relatively small quantities of actinides, and process chemicals. Some of the waste products were originally stored below the surface as liquids contained in 149 single-shell, steel-lined concrete tanks. Other liquid wastes with low-level radioactivity were disposed of to the soil column by ponds, cribs, trenches, and french drains. In addition, radioactively contaminated solids, such as equipment, paper, and clothing, have been buried in soil-covered trenches.

Leakage of a single-shell tank was first detected in 1956. Starting in the early 1960's, work was initiated to convert the single-shell tank wastes to a stable, semisolid form consisting of salt cake and sludge that contains residual liquids trapped in the pore space of the solids. Transfer of pumpable liquids from the single-shell tanks to underground double-shell tanks is part of an ongoing program of waste stabilization. The low-level fraction of the double-shell tank waste will be finally disposed of as grout monoliths enclosed in buried concrete vaults.

Because of the extensive work at the Hanford Site in developing PORFLO-3, additional references to this Site will be made in other chapters of this report. However, PORFLO-3 embodies the basic physical principles of fluid flow, heat transfer, and mass transport in variably saturated geologic media, and its potential use is not limited to a specific site. It can easily be adapted to solve diverse problems related to groundwater flow and quality.

In developing the PORFLO-3 program based on an accepted theory of fluid flow, heat transfer, and mass transport, two steps were taken to ensure that the program is appropriate for diverse uses: (1) the program structure was made modular so that each module could readily be replaced to customize the program to solve specific problems and (2) numerous user-selected options were provided to help solve a diversity of problems. The theoretical basis and features of PORFLO-3 are described in this report; detailed instructions for use of the computer program are provided in another report (Runchal and Sagar 1989).

1.2 REPORT CONTENT

A brief summary of the principal features of the model is provided in Section 1.3. The concept of the hydrologic environment simulated by PORFLO-3 is discussed in Chapter 2.0. For purposes of analyzing groundwater flow and contaminant migration through geologic media, flow may be considered to occur wholly through porous sediment or soil (i.e., neglecting flow through discrete features, such as fracture zones), entirely by means of discrete fractures, or by means of a combination of flow through porous media and fractures. Each of these concepts is discussed in Chapter 2.0.

In Chapter 3.0, a reasonably complete derivation of the governing equations of the PORFLO-3 model is provided. There are three primary governing equations--one each for fluid flow, heat transfer, and mass transport. In addition, auxiliary equations of state, constitutive relations, and applicable boundary conditions are described. The ways in which the three equations are coupled are also explained.

Chapter 4.0 is devoted to describing the numerical solution methods for the governing equations. Details of the nodal point integration method for obtaining discretized equations are provided. Methods for solving the discretized set of equations are described. Stability and convergence properties of the solution methods are discussed.

Application of PORFLO-3 to two selected problems is discussed in Chapter 5.0. More detailed, independent benchmark and verification testing of PORFLO-3 is underway.

1.3 MAIN FEATURES OF PORFLO-3

Equations describing fluid flow, heat transfer, and mass transport in variably saturated, porous media form the mathematical framework for PORFLO-3. In addition to the governing equations, several auxiliary equations describing fluid and solid properties also are used. By choosing a particular set of these equations, the model can be used to solve problems of varying complexity. A brief description of some of these features is provided in the following sections.

1.3.1 Spatial Dimensionality

The program is designed to solve three-dimensional problems. However, it can be adapted to solve one- and two-dimensional problems by specifying a grid size(s) of three in the direction(s) that is (are) to be omitted. In effect, this specification results in the solution of a pseudo-three-dimensional problem.

1.3.2 Problem Geometry

A problem can be defined in terms of either Cartesian or cylindrical coordinates. In both coordinate systems, z is the direction of the vertical coordinate. The horizontal plane is represented by x-y in the Cartesian system and by r-θ in the cylindrical system. In a one-dimensional problem, any of the three axes (x, y, or z) can be selected as the direction of interest. Two-dimensional problems can be solved in the x-y, x-z, or y-z plane. The computational elements can vary in size across the coordinate system, but their geometry is restricted to that of a rectangular parallelepiped.

1.3.3 Time Dependence

Either transient or steady-state problems can be solved. Except for the spatial grid, all problem parameters can change with time. The values of some parameters, such as the source terms for fluid, heat, and mass, can be assumed to change continuously with time. Such quantities can be specified in the form of tables. For other parameters, such as boundary conditions and properties of the media, the input data deck can be designed to change the data values after the time intervals specified.

1.3.4 Space Dependence

The values of most parameters are allowed to vary over the spatial grid. The model domain can be divided into zones, each having a distinct feature such as a material property or concentration. The material properties can also be anisotropic.

1.3.5 Coupling of Equations

There are three main equations in PORFLO-3, one each for fluid flow, heat transfer, and mass transport. The state variables of the equations are the hydraulic head (P), temperature (T), and concentration (C). These equations can be solved either independently or in various coupled modes. Consequently, problems related only to fluid flow, heat transfer, or mass transport can be solved, or problems in which fluid flow is coupled to heat transfer or mass transport can be solved, or all three equations can be solved in a coupled mode. Depending on the specific problem, some of the couplings can be switched on or off (e.g., the effects of thermal buoyancy, fluid density, and viscosity on hydraulic properties).

1.3.6 Boundary Conditions

Varied types of boundary conditions can be specified in PORFLO-3. Dirichlet (specified values of hydraulic head, temperature, or concentration), Neumann (specified fluxes of fluid, heat, or mass), or mixed (a combination of specified values and fluxes) boundary conditions can be stipulated. Different types of boundary conditions can be designated at different parts of a boundary. Combined with the time-dependence feature discussed in Section 1.3.3, this feature can be used to solve a large variety of problems with space- and time-dependent boundary conditions.

Occasionally, solution of the heat and mass transport equations is required within a large domain. In such cases, if heat and mass are transported at a slow rate, an option may be used to solve these equations in grids that are smaller than the total domain. With this option, a user can specify a location between the source and external boundary of the domain to be a temporary subdomain. This temporary subdomain is automatically expanded or eliminated when a specified condition is satisfied. This option can save computational time for problems that are characterized by large domain sizes and heat and/or mass sources concentrated in a small portion of the overall domain.

1.3.7 Methods for Solving Governing Equations

The governing equations are solved by first discretizing them over the spatial grid and time steps and then solving the resulting system of linear algebraic equations. The fluid flow equation is discretized based on quadratic approximating functions; these functions are equivalent to a central difference scheme. The second-order partial differential terms in the heat transfer and mass transport equations are also discretized through quadratic approximating functions. However, the first-order partial terms in these

equations can be discretized either by a hybrid or an exponential scheme. The nature of these schemes is described in Chapter 4.0. The discretization method used in PORFLO-3 is based on integrating the approximating functions for each grid element. This method results in solutions that automatically conserve fluid, heat, and mass locally within every grid element, as well as for the entire domain.

Alternative solution methods for the linear systems of algebraic equations are provided. These include the explicit method of point successive over-relaxation and the implicit methods of alternating direction implicit, Cholesky decomposition, Gauss elimination, and conjugate gradients.

1.3.8 Operational and Output Control

Through design of the input data deck, the user can exert extensive control over the operation of PORFLO-3. For example, the execution of the program can be stopped to examine the output at any convenient point and can be restarted later from the point at which it was stopped. The user also has considerable control over the extent and nature of output. Output can be obtained as a tabulation or written in a file for post-PORFLO-3 processing in graphic form. The variables to be tabulated, the size of the tables, and the times at which they are to be obtained can all be controlled by input commands.

1.3.9 Variable Saturation

Problems in which the geologic media are either fully or partially saturated, or in which some parts are fully saturated while others are partially saturated, can be solved with PORFLO-3. In the partially saturated phase, liquid (water) and gas (air) are assumed to exist. However, only the movement of the liquid phase is addressed; i.e., vapor transport is not considered. Consequently, PORFLO-3 is a "single-phase" computer program.

As part of the solution of problems, the degree of saturation is determined at each grid node of the domain. The boundary between the partially and fully saturated portions of the geologic media is the water table. The water table can be moved up and/or down only from grid node to grid node; no adjustment for water table position can be made that does not coincide exactly with node locations.

1.3.10 Special Geologic Features

In addition to the capability to consider heterogeneity and anisotropy of the porous geologic media, as noted in Section 1.3.4, an option is included in PORFLO-3 that permits the user to consider planar geologic features such as fractures, faults, and clastic dikes. These features are distinguished from those of the parent media (soil and/or rock) by their distinctively different length scale and properties. For example, one of the three dimensions of fractures, faults, and clastic dikes is so small relative to the other two that these features behave essentially as two-dimensional (planar) elements that are embedded in the three-dimensional domain.

Similarly, boreholes or small man-made excavations are essentially one-dimensional features.

As indicated in Section 1.3.4, it is possible to treat all of these features as distinct, three-dimensional zones. However, because of the different length scales involved, this treatment may result in exceedingly large grid sizes. An alternative option, to consider such features as two- or one-dimensional elements that are embedded within three-dimensional media, is available in PORFLO-3. The choice of this option reduces the required grid sizes and computational time, but only approximates the solutions of the equations in close proximity to the embedded features.

1.3.11 Pore Structure

The user can define up to three types of porosities in PORFLO-3. The smallest of these is the effective or flow porosity, which consists of the pores through which fluid flow occurs. The second is the diffusive porosity. Diffusive porosity is greater than, or equal to, the effective porosity. It includes the dead-end pores that are assumed not to contribute to fluid flow, but that are assumed to facilitate the diffusion of heat and mass. The third porosity is the total porosity. Total porosity is greater than, or equal to, the diffusive porosity. In addition to the pores that comprise the effective and diffusive porosities, total porosity includes the isolated pores that are assumed to be inert to fluid flow and diffusion. These pores, however, are assumed to contribute to the conduction of heat.

1.3.12 Sources and Sinks

Several options are provided in PORFLO-3 for describing sources and/or sinks of fluid, heat, and mass. Spatially variable sources and/or sinks can be specified by identifying their zones of occurrence. The strength of a source and/or sink can either be constant or vary with time. For mass, a source can be limited by its inventory, solubility, or both.

1.3.13 Format-Free Input

The input to PORFLO-3 is provided in a manner that is free of any format requirements. This feature is a major step towards making the program "user friendly." All input to PORFLO-3 is provided through the use of a keyword followed by alphanumeric data. Although the numerical data, after a keyword, must be entered in a specified sequence, it can be entered in any convenient format (I, E, or F) at any column location of the eighty-column input-data card. In general, an input record can be designed to read like an easily understood complete sentence. A preprocessor is employed to interpret this input for internal use in the program. Details of the input structure are provided in Runchal and Sagar (1989).

2.0 CONCEPTUAL FRAMEWORK

A mathematical model, like PORFLO-3, can provide only a simplified representation of a complex hydrogeologic system. A variably saturated groundwater system, which is the focus of PORFLO-3, can be viewed at different scales--from the very small (molecular) to the very large (regional). Its description would vary according to the scale of choice. Even when a scale has been selected, several assumptions must be made regarding (1) the processes to be treated by the model, (2) the constitutive equations that represent these processes, (3) the level of detail at which coupling occurs between or among the processes, (4) geometric representation of the physical system, and (5) the spatial and temporal variations of the parameters and boundary conditions.

Decisions on all of these factors result in what can be called a "conceptual model." A conceptual model of a given physical system is not unique; rather, it depends on the objective(s) of the model. For a numerical model to work reasonably well for a given problem, the conceptual model embodied by it should be compatible with the user's concept of a particular problem. For this reason, it is important to describe the conceptual framework of PORFLO-3. Factors affecting conceptual models are discussed first; these factors are then related to features specific to the Hanford Site.

2.1 GENERAL CONSIDERATIONS

2.1.1 Scale of Representation

Geologic media, the groundwater or other fluids contained within those media, and the entities transported by the groundwater (e.g., heat energy and mass of chemicals and radionuclides) can be represented at many scales. These scales may be as small as that of a molecule or as large as that of an entire geologic region. Obviously, as the scale becomes smaller, some of the details that are important at larger scales are lost. Consequently, the mathematical representation depends on the scale of the problem.

In PORFLO-3, the characteristic scale can be termed "macroscopic" (i.e., much larger than a molecule but much smaller than most areas characterized by a common set of geologic features). At this scale, both the media and the contained fluid are considered to be continua. In the context of heat or mass transport through geologic media, this means that individual pores are not distinguished and that the media and their contained fluid are treated as if they simultaneously occupied the same space. As a consequence, pressure, temperature, and concentration can be defined at any point in space, irrespective of whether that point is occupied by a solid or a fluid. Obviously, such an assumption is not valid at molecular or microscopic scales.

Another scale of interest is that at which the properties of the continua vary. In the most general case, these properties can vary continuously in space. In practice, when numerical solutions are used, as is the case with PORFLO-3, it is common to assume that the properties are continuous

in a piecewise sense; e.g., they vary from computational cell to computational cell, but are constant within a cell. In this regard, the model is highly flexible, and the user may choose any scale of property variation that is consistent with the capabilities of the computer used. Consequently, the porous media can be assumed to consist of layers or strata, with each layer having distinct properties. Alternatively, the properties of the media can be assumed to vary continuously in a piecewise fashion. Similarly, fluid properties such as density can be varied in a piecewise fashion. However, once the computational domain is discretized, the scale of variation of all parameters is limited to the scale defined by that discretization.

In addition to being treated as heterogeneous, material properties also can also be considered to be anisotropic in the PORFLO-3 model. However, consideration of anisotropy in PORFLO-3 is limited to problems in which the coordinate axes coincide with the principal directions of the anisotropy. In other words, instances in which the direction(s) of anisotropy vary arbitrarily in space are excluded from the model.

2.1.2 Fractures, Joints, Faults, and Clastic Dikes

Of special interest to evaluation of the potential for transport of contaminants in groundwater are the effects of features such as fracture and fault zones, joints, and clastic dikes. From the perspective of simulating groundwater flow and contaminant transport, these features can be important because they have properties that are distinctive from those of their surroundings. Hence, an option has been included in PORFLO-3 that permits their simulation as separate elements. Inclusion of these features in the model is effective only if their hydrologic properties are well known.

If these features are numerous, small, discontinuous, and without pronounced preferential orientation, they can be treated as equivalent to the pores of geologic media (i.e., treated piecewise as geologic continua). However, if their hydrologic effects are large relative to those of their surroundings, they can be treated as a distinct zone or stratum in the model.

In some areas, faults or clastic dikes occur relatively infrequently, have properties that are distinctive from those of their surroundings, and/or are smaller than the scale at which the properties of the surrounding porous media vary, but are much larger than the pores of those surrounding media. In such instances, the disparate scales that need to be included in the model can lead to numerical difficulties. In PORFLO-3, features of this type can be represented as two-dimensional planar elements that are embedded in the porous, three-dimensional continua. The model allows the properties within such planar elements to be anisotropic.

Two limitations are imposed by the model for depicting embedded planar elements. First, the elements must be aligned with the grid used for discretization of the domain. Second, the interchange of fluid or mass between the planar features and their surroundings can occur only at grid nodes. In other words, within an element, only one value of pressure, temperature, and

mass concentration is calculated. This value is applied to both the porous continua and the discrete planar feature. Consequently, sharply focused resolution of the state variables of interest cannot be obtained in close proximity to such discrete features.

The methods used for in situ measurement of properties important to evaluation of groundwater movement and contaminant transport in geologic media are also an important consideration in deciding whether specific geologic features should be treated discretely in the PORFLO-3 model. In saturated media, most hydraulic properties are measured by conducting pumping tests that stress a specified volume and then observing the effects of the imposed stress. The values of the hydrologic parameters obtained by such tests are assumed to be representative of the volume stressed.

However, the volume may include discrete features as well as the porous continua because it is difficult, if not impossible, to strictly limit the volume stressed so that all discrete features are excluded. Consequently, it may not always be possible to determine the in situ properties that are specific to discrete hydrogeologic features. In such cases, the inclusion of discrete features in the conceptual model may not be productive.

2.1.3 Boreholes, Shafts, and Drifts

It has been common practice to drill boreholes and excavate shafts and drifts during hydrogeologic evaluation of sites for the potential disposal of radioactive and hazardous chemical wastes. Occasionally it is important to account for these features in modeling the groundwater flow and contaminant transport processes at a site. Hence, depiction of these man-made features can be included as distinct, fully three-dimensional elements in PORFLO-3. An additional provision has been made for permitting simulation of such features as one-dimensional elements embedded in the three-dimensional rock or soil. The mathematical treatment of these elements is the same as that of the two-dimensional fractures; details of this treatment are discussed in Chapter 3.0.

2.1.4 Porosity

Three different porosities for the rock or soil matrix are used in PORFLO-3. Total porosity is composed of all pore space enclosed within the rock or soil matrix. This porosity affects heat transfer by conduction and is important only when conductive heat transfer is a significant consideration. Effective or flow porosity is composed of pores that are interconnected so that fluid movement can occur through them. This porosity is an important consideration in calculating fluid velocity and convective transport of heat and mass. The third type of porosity is termed diffusional porosity. Diffusional porosity is greater than, or equal to, the effective porosity. It includes, in addition to the flow porosity, interconnected pores in which the contained fluid is stagnant. This porosity is of primary importance in heat and mass transfer by molecular diffusion. In general, the total porosity is greater than, or equal to, the diffusional porosity, which is, in turn, greater than, or equal to, the effective porosity.

The pore space that is representative of the difference between the total porosity and diffusional porosity is assumed by the PORFLO-3 conceptual model to be filled with liquid, even in partially saturated media. An alternative concept would be to assume that these pores are filled with air; this alternative is not considered in PORFLO-3.

The liquid contained within pores that are representative of the difference between diffusional porosity and effective porosity is assumed to be immobile. Consequently, for problems involving groundwater flow in the unsaturated zone, these pores contain the residual moisture that does not drain, even for conditions of extreme soil-moisture tension. During mass transport, this residual porosity would contribute to the retardation of a contaminant pulse.

2.1.5 Sources and Sinks

For most waste management problems, sources and/or sinks of fluid, heat energy, and chemical species are present in the domain of interest. Considerable effort is typically required to depict these sources (sinks) in a form suitable for a mathematical model. The sources (sinks) may be distributed in space and may be functions of either time or space. Special discretization of the governing equations, with respect to space and time, may be required to accommodate such sources (sinks).

The simplest sources (sinks) are constant with respect to time and are specified at only a few discrete locations. Somewhat more complex are those sources (sinks) that vary with time. Time-varying sources (sinks) vary in accordance with a regular function. For example, they may vary exponentially, as is the case for radioactively decaying sources. Arbitrary variations may be approximated in the form of a table.

The most complex type of source (sink) for chemical species that is available for depiction by the operator of PORFLO-3 is specified in terms of inventory (or initial mass) and solubility. The simulation of this type of source requires that the concentration of contaminant mass in the source region be maintained at a level that is consistent with a mass that depletes continuously as a function of time. Consequently, with a sufficiently large initial mass, the mass concentration of the source region will be equal to the solubility constant of the species of concern and will remain at this level until the mass is depleted to the extent that this concentration can no longer be maintained. At this time, the concentration at the source will decrease as a function of time.

2.2 CONCEPTS FOR FLUID FLOW

2.2.1 Geologic Media and Fluid Compressibility

In geologic media, the transfer of mechanical stresses between the fluid contained in the pore space and the rock or soil matrix occurs slowly. Mechanical equilibrium under applied stresses is maintained by a sharing of

the stress load by the fluid and the rock. If the rock or soil are appreciably compressible, resulting in significant strains, the deformation of matrix elements may have to be explicitly considered in modeling fluid flow and mass transport.

In PORFLO-3, the matrix (rock or soil) is considered to be only slightly compressible; consequently, the deformation is assumed to be sufficiently small that the positions of matrix elements are assumed to be static. However, the compressibility of rock or soil is not entirely neglected. Its effect is included in the "specific storage" term that represents the quantity of fluid expelled by a unit volume of the saturated media when the stress on it is increased by a unit amount.

2.2.2 Darcy Flow

The flow of fluids in all physical elements (i.e., rock or soil matrix, planar fractures, boreholes, shafts, and drifts) of the geologic media is described by the Darcy equation. In the mathematical treatment of the conceptual model, details of which are provided in Chapter 3.0, the Darcy equation is substituted for more complex momentum-transfer equations. This substitution considerably simplifies the mathematical description of flow.

Only the flow of liquids is considered explicitly in Version 1 of PORFLO-3; that is, in unsaturated media, the gas phase is considered to be at ambient pressure at all times and locations. This assumption is reasonable in most cases. It may not be valid for conditions in which either the escape routes of the gas are blocked or the gas is moving rapidly. In such instances, a multiphase version of PORFLO-3, which is currently under development, should be used.

For conditions of partially saturated flow, the volumetric moisture content and hydraulic conductivity are assumed to be functions of the soil-moisture tension. In many soils and rocks, these relationships vary, depending on whether the soil or rock is imbibing or draining liquid (i.e., on its wetting and drying history). These effects of hysteresis are not considered in the current formulation of PORFLO-3.

2.2.3 Thermal Buoyancy

In nonisothermal fluid flow, particularly in the presence of heat sources, a driving force on the fluids present is created because of the buoyancy of a warmer (and therefore lighter) fluid within a region of relatively cooler fluid. This buoyancy effect is a function of fluid density variation resulting from a variation in temperature. A term to describe the effect of buoyancy on fluid movement (but not on vapor movement) is included in PORFLO-3.

2.3 CONCEPTS FOR HEAT TRANSFER

2.3.1 Thermal Equilibrium

In PORFLO-3, heat exchange between the fluid and the rock or soil matrix is assumed to be sufficiently rapid that the fluid and the matrix are in thermal equilibrium at all times. The effects of this assumption are that the fluid and the rock are depicted as being in intimate thermal contact, and the fluid is represented as moving slowly compared to the rate of heat transfer. For the purpose of calculations, this concept of the process of heat transfer treats the saturated rock or soil matrix as a composite (i.e., consisting of two phases, solid and fluid), with thermal properties that are weighted averages of the properties of the fluid and the matrix. This results in a single temperature value that represents the temperature of the solid and the fluid at a point.

2.3.2 Thermo-Mechanical Stresses

Mechanical stresses created by thermal loading are considered to be small and consequently are neglected in PORFLO-3. The basis for this assumption is similar to that discussed in Section 2.2.1; i.e., the thermal rock modulus is small and, therefore, rock deformation caused by thermal loading, as far as its effect on fluid flow is concerned, is small.

2.3.3 Coupling Between Fluid Flow and Heat Transfer

A two-way coupling between fluid flow and heat transfer is provided for in PORFLO-3. Transfer of heat in saturated media can alter fluid flow by (1) a change in the density and viscosity of the fluid and (2) a transient change of temperature, creating a time-dependent source term for the fluid properties. Consideration of both effects is included in PORFLO-3. Depiction of the first effect is manifested through temperature-dependent hydraulic conductivity and thermal buoyancy terms. Depiction of the second effect is proportional to the time-rate-of-change of temperature. Similarly, the effect of the fluid flow on heat transfer is included as a convective term.

2.4. CONCEPTS FOR MASS TRANSPORT

2.4.1 Sorption by the Rock or Soil

A linear relationship for partitioning the mass of the contaminant species between the fluid and the rock or soil matrix is included in PORFLO-3. The partitioning is assumed to occur instantaneously; i.e., all kinetics are neglected. In addition, a perfect balance between sorption and desorption is assumed; i.e., hysteresis is not considered. These assumptions admittedly result in a highly simplified representation of the actual chemical phenomena. Provision is made in PORFLO-3 for sorption properties of the soil or rock that may be different from those of the discrete features embedded in the porous media.

2.4.2 Chain Decay

Transport of only single radionuclides is considered in PORFLO-3. Although decay of a single radionuclide is allowed, the effects of daughter products are neglected. This limitation restricts application of the program to those radionuclides whose presence does not derive from the decay of other radionuclides. Many radionuclides of interest for the safe disposal of commercial, high-level nuclear waste, such as iodine-129, carbon-14, technetium-99, and selenium-76, are not affected by this restriction.

2.4.3 Contaminant Source Term

Three options for depicting the contaminant source term are included in the model. The most general option is the specification of either a time-constant or piecewise (i.e., discretized) variance of the source term with time. The other two options are for solubility-limited and inventory-limited source terms. If these options are exercised, the concentration at the source is maintained at the limit provided by the solubility of the species. An account is then kept of the mass moving away from the source until all of the inventory is depleted. At that time, the concentration is allowed to decrease from the solubility limit. Currently, an option to depict congruent solubility is not provided.

The dissolution of waste constituents into the fluid is considered to be instantaneous; i.e., when the waste comes into contact with the fluid, it dissolves in accordance with the solubility limit for the species of interest.

2.5 DOMINANT HYDROGEOLOGIC FEATURES OF THE HANFORD SITE

As stated previously, obtaining a better means of evaluating current and proposed waste management practices at the Hanford Site has been the primary motivation for developing PORFLO-3. For this reason, the major hydrogeologic features of the Hanford Site that would influence the solution of the governing and auxiliary equations of the PORFLO-3 model were taken into consideration in the model development. A brief discussion of these features follows.

2.5.1 River Boundary

Figure 2-1 shows the location of the Hanford Site. Most of the Hanford Site occupies a terrace of the Columbia River (COE 1970). The elevation of the terrace increases gradually from about 112 m above mean sea level at Richland, Washington, to about 270 m in the northwest and decreases to about 150 m in the northern part of the Site. The so-called Hanford Reach of the Columbia River, extending downstream from Priest Rapids Dam at River Mile 397 to the backwaters of McNary Dam, is free flowing. The flow of the Columbia River in the Hanford Reach is regulated by releases from Priest Rapids Dam.

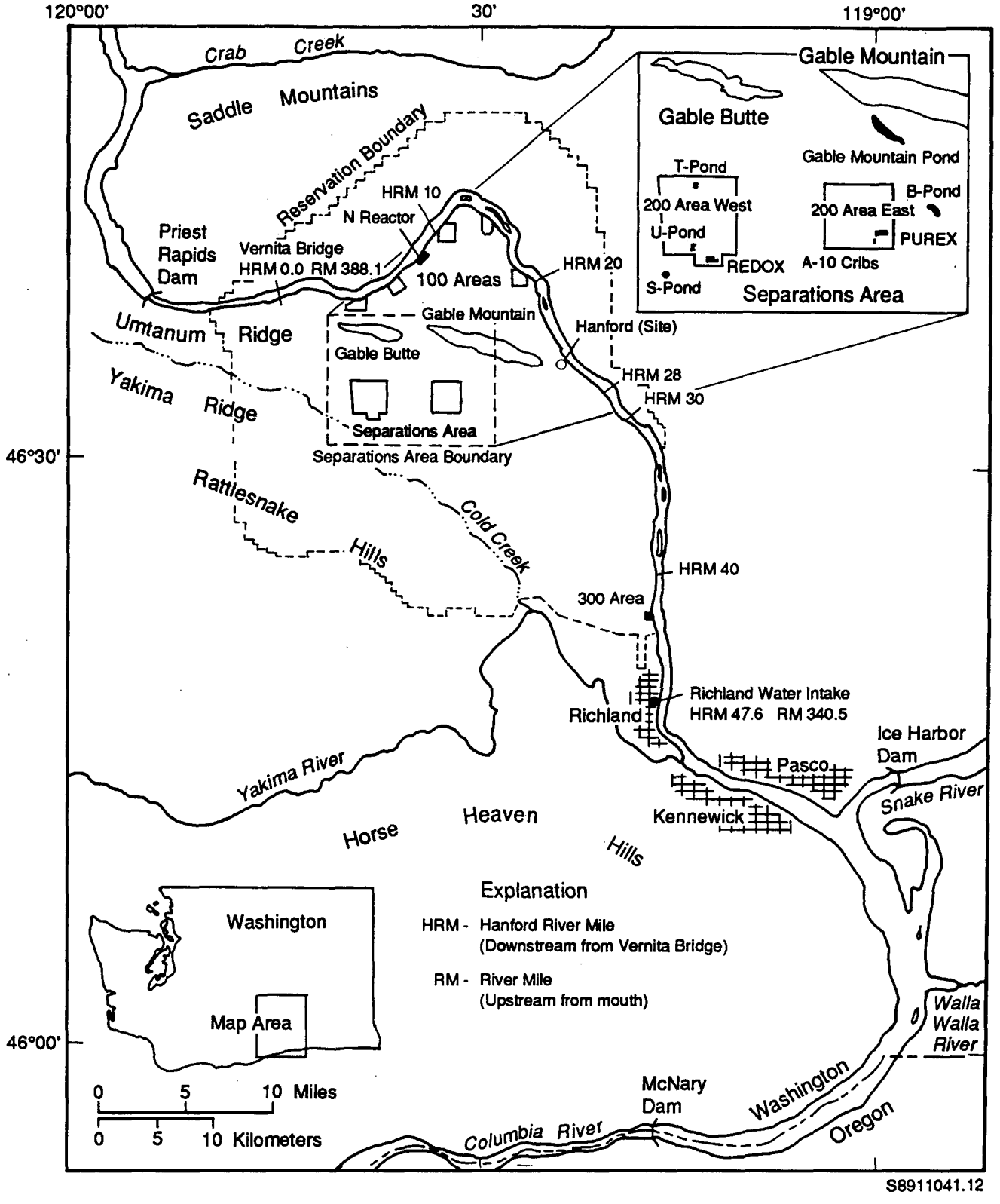

Figure 2-1. Location of the Hanford Site.

In concept, the river is normally included in the model as a boundary where pressures (or hydraulic heads) are known. The hydraulic head is equal to the river stage measured from a common datum. Geometrically, the river is represented in a piecewise manner as a planar or linear boundary of a three- or two-dimensional model, respectively. Depending on the available data, the hydraulic pressures at the river boundary may be treated as constant or as varying with respect to space and/or time.

2.5.2 Recharge Boundary

The Hanford Site has a semiarid climate, with approximately 15 cm of annual precipitation and sparse vegetation. A fraction of the annual precipitation enters the vadose zone at the ground surface as natural recharge; this surface is typically represented as a recharge boundary in the model. The actual recharge depends on meteorologic conditions, soil properties, and vegetation and may vary both spatially and temporally. Algorithms for estimating recharge are not provided in PORFLO-3. The UNSAT-H model (Fayer et al. 1986) has been developed to estimate recharge specific to the Hanford Site, using environmental data such as precipitation, temperature, and relative humidity.

Water balance data have been collected at selected locations on the Hanford Site during the past 10 yr (Gee et al. 1988). These data indicate that coarse-textured soils (i.e., soils that contain 90% or more sand-size or larger particles) that are sparsely vegetated or are covered with shallow-rooted grasses (e.g., cheatgrass or native bluegrass) are susceptible to drainage that is a significant proportion of precipitation, especially in winter. Drainage measurements in 1988, from twelve bare-surface lysimeters in the 300 Area of the Hanford Site, ranged from 3.1 to 5.6 cm/yr from precipitation of 12.5 cm/yr (Gee et al. 1988). In contrast, no drainage was measured at another lysimeter at the same location that was covered by deep-rooted (greater than 1 m) vegetation (e.g., tumble mustard).

The recharge from the surface boundary of the model domain can be depicted either as a Neuman-type (specified flux) boundary condition or as a fluid source in the region near the surface.

In addition to the surface recharge, at the scale of the Pasco Basin, natural recharge also occurs along the periphery of the basin from precipitation and ephemeral streams. Past waste disposal activities at the Hanford Site have locally contributed to recharge. Recharge from irrigated farming occurs east and north of the Columbia River and in the synclinal valleys west of the Hanford Site (Gephart et al. 1979). Upward leakage, from confined intrabasalt aquifers to the overlying unconfined aquifer, also is thought to occur within the northern and western sections of the Hanford Site. Groundwater discharge is principally to the Columbia River.

2.5.3 Water Table Boundary

The water table forms a hydraulic boundary between the vadose zone and the aquifers below it. Extensive records of water table elevations at the Hanford Site are available (e.g., McGhan et al. 1985). If modeling of only

the vadose zone is of importance, the location of the water table may be specified as a boundary at which the hydraulic head is maintained at atmospheric pressure. However, if the saturated zones below the water table also are to be simulated, only the initial location of the water table needs to be specified. In this case, the elevation of the water table will be determined in response to the hydraulic stresses imposed on the system.

2.5.4 Other Boundary Conditions

Depending on the scale (regional versus local) and objective of the simulation, other boundary conditions may be envisioned. For example, on a local scale, at a location that is removed from the Columbia River, boundary conditions may be specified, based on measured moisture content of the vadose zone and measured hydraulic heads of the saturated zone. As a general rule, natural boundaries of groundwater basins (e.g., rivers and mountains) should be used in the simulation models. Where such boundaries do not exist, hydraulic boundaries can be imposed, based on the user's concepts. In such cases, the boundaries should be sufficiently distant from the area of interest that their influence on the flow field is minimized.

2.5.5 Vadose Zone Hydrogeology

The sediments overlying the basalts of the Hanford Site (suprabasalt sediments) were derived from a variety of sources. However, the fluvial-lacustrine Ringold Formation and glaciofluvial Hanford formation dominate (Bjornstad 1985). A brief description of these formations is given below.

2.5.5.1 Ringold Formation. The Ringold Formation overlies the Elephant Mountain Member of the Saddle Mountains Basalt (Figure 2-2) and ranges in thickness from about 110 to 215 m. Based on texture, grain size, and stratigraphic position, the Ringold Formation has been divided into four units: basal, lower, middle, and upper.

The basal Ringold unit, up to 60 m thick, has been subdivided into two subunits. The coarse-grained subunit is primarily gravelly sand, although lenses of sandy gravel and cross-bedded sand occur locally. Overlying the coarse-grained subunit is the fine-grained subunit, which is a conformable sequence of ripple-laminated micaceous muds and sands. This subunit includes, and is capped by, a well-developed paleosol sequence (Bjornstad 1985). This interval consists of a massive, bioturbated, olive-colored, clay-rich alluvial horizon. Subhorizontal stringers of light-colored, pedogenic calcium carbonate occur toward the base of the paleosol (Figure 2-3). A 2- to 5-cm layer of tephra lies at or near the top of the paleosol sequence.

Silt and clay of the lower Ringold unit, up to 16 m thick, overlie the basal Ringold unit. Sedimentary structures within the lower Ringold range from thin, rhythmic laminations at the base to generally more massive, irregular, and subhorizontal laminations upward. Occasionally, an interval of pale yellow to gray, even-laminated mud exists in the uppermost lower Ringold unit.

Period	Epoch	Group	Subgroup	Formation	Member or Sequence	Sediment Stratigraphy or Basalt Flows	Unit Thickness Ranges (m)
Quaternary	Holocene				Surficial Units	LOESS, Sand Dunes, Alluvium, Alluvial Fans, Landslide, Talus, Colluvium	< 3 [a]
	Pleistocene			Hanford	Touchet Beds / Pasco Gravels		≤ 5 [a] / ≤ 64 [a]
Tertiary	Pliocene					Plio-Pleistocene Unit	0 - 26 [a]
				Ringold		Upper Ringold	0 - 33 [a]
						Middle Ringold	55 - 100 [a]
						Lower Ringold	0 - 17 [a]
						Basal Ringold	6 - 60 [a]
	Miocene	Columbia River Basalt Group	Yakima Basalt Subgroup	Saddle Mountains Basalt	Elephant Mountain Member	Elephant Mountain Flow	0 - 39.0
						Rattlesnake Ridge Interbed	0 - 34.4
					Pomona Member	Pomona Flow	0 - 59.0
						Selah Interbed	0 - 30.8
					Esquatzel Member	Gable Mountain Flow	0 - 36.3
						Cold Creek Interbed	0 - 36.6
					Umatilla Member	Sillusi Flow (Discontinuous)	20.7 - 73.2
						Umatilla Flow	
						Mabton Interbed	25.6 - 51.8
				Wanapum Basalt	Priest Rapids Member	Lolo Flow	39.3 - 55.2
						Rosalia Flow	16.5 - 33.5
						Quincy Interbed (Discontinuous)	0 0.5
					Roza Member	Roza Flow (2 Cooling Units)	42.1 - 59.4
						Squaw Creek Interbed (Discontinuous)	0 - 0.9
					Frenchman Springs Member	Sentinel Gap Flow	50.9 - 64.6
						Sand Hollow Flows (2 Flows)	32.6 - 54.4
						Silver Falls Flows (1 to 3 Flows)	19.8 - 47.9
						Ginkgo Flows (2-3 Flows)	68.0 - 100.9
						Unnamed Interbed (Discontinuous)	0 - 3.7
						Palouse Falls Flow	9.1 - 25.0
						Vantage Interbed	0 - 9.1
				Grande Ronde Basalt	Sentinel Bluffs Sequence	Flow 1	5.3 - 25.6
						Flow 2	15.9 - 34.9
						Rocky Coulee Flow	40.2 - 57.0
						Levering Flow (Discontinuous)	0 - 28.0
						Cohassett Flow	65.8 - 81.4
						Birkett Flow	34.7 - 43.3
						Flow 7	9.0 - 18.2
						Flow 8	11.6 - 24.4
						McCoy Canyon Flow	32.3 - 45.0
					Schwana Sequence	Umtanum Flow	60.5 - 75.0
						Very High-Mg Flow	0 - 22.6
						At Least 3 Flows [b]	93.5 [a]
						N_2-R_2 Paleomagnetic Contact Greater than 10 Flows	> 1,750 to Base of Basalt

Ellensburg Formation

NOTE: To convert meters to feet, multiply by 3.28

[a] Thickness range for the reference repository location only.

[b] Value is a minimum only (only one borehole penetrated to base of lower buffer zone).

S8911041.1

Figure 2-2. Typical Stratigraphic Units at the Hanford Site.

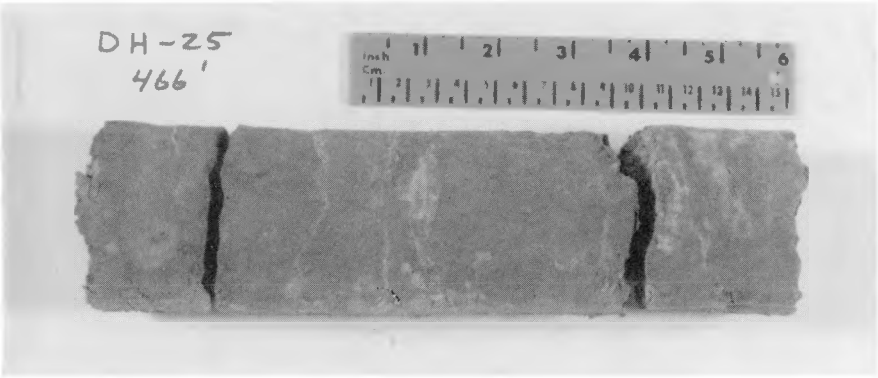

Figure 2-3. Core from a Segment of the Basal Ringold Paleosol Sequence. Light-colored, subhorizontal layers are pedogenic calcium carbonate within illustrated clay.

The middle Ringold unit is composed of stream gravels (Routson and Fecht 1979) and is the thickest of the suprabasalt units. These gravels consist mostly of quartzite, with lesser amounts of volcanic and plutonic clasts (Figure 2-4). The uniform, clast-supported texture of the middle Ringold unit is locally interrupted by thin zones of current-laminated sand and mud.

The upper Ringold unit consists of alternately bedded and laminated arkosic sand and mud that are representative of a low-energy fluvial and lacustrine environment. Its thickness varies considerably, primarily caused by erosion by post-Ringold fluvial incision and cataclysmic flooding.

2.5.5.2 Hanford Formation. Varying in thickness from 5 m to 65 m, Pleistocene cataclysmic flood deposits of the Hanford formation also have a wide range of grain size. The two recognized units of the Hanford formation are the Pasco gravels and the Touchet beds.

The Pasco gravels are composed of basaltic, massive-to-laminated coarse sand, and/or large-scale, foreset-bedded gravel. They are mainly restricted to the Pleistocene flood bars and terraces that developed along high-energy flood channelways. The Touchet beds are a rhythmically bedded and fine-grained flood facies deposited away from main flood channelways in slack-water or backflooded areas during flooding (Waitt 1980). At many locations of the Hanford Site, Holocene surficial deposits of dune and sheet sand, alluvium, loess, and colluvium overlie the Hanford formation. The thickness of these deposits is on the order of a few meters.

2.5.6 Saturated Zone Hydrogeology

The principal geologic feature of the saturated zone of the Hanford Site is the layered nature of the Columbia River basalt flows; most conceptual models of the Hanford Site include this layered aspect. The other geologic features of hydrologic interest are the cooling joints and fractures and the interaflow structures that exist within individual basalt flows. The

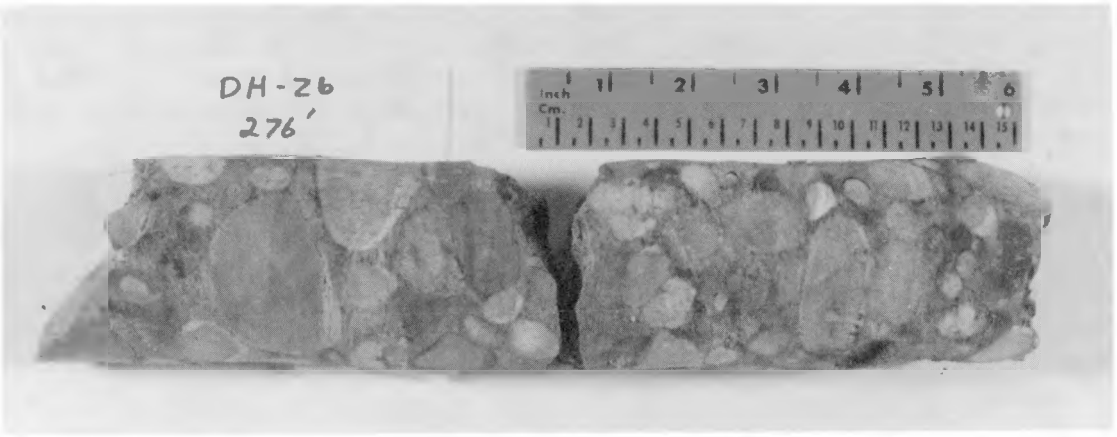

Figure 2-4. Core from Middle Ringold Unit that Consists of Semi-consolidated, Bimodel, Clast-Supported Conglomerate.

Columbia River Basalt Group is formally divided into five formations, from oldest to youngest: Imnaha Basalt, Picture George Basalt, Grande Ronde Basalt, Wanapum Basalt, and Saddle Mountains Basalt. Only the last three occur at the Hanford Site. A brief description of these three formations is provided below.

2.5.6.1 Grande Ronde Basalt. The Grande Ronde Basalt is geographically the most extensive and voluminous formation within the Columbia River Basalt Group. More than 50 flows of Grande Ronde Basalt underlie the Pasco Basin; however, relatively little is known about the hydrology of the lower 80% to 90% of the Grande Ronde Basalt. Flows of the Grande Ronde Basalt were erupted from fissures and vents throughout the eastern half of the Columbia Plateau. These basalt flows are typically aphyric, although a few flows scattered throughout the section contain sparse to abundant plagioclase phenocrysts.

Aquifers of the Grande Ronde Basalt are confined to semiconfined (with some vertical leakage). The aquifers are regionally recharged along the margins of the Columbia Plateau where the flows crop out or are near the ground surface. Portions of the Columbia River and Snake River drainage systems intersect outcrops of the Grande Ronde Basalt; hence, direct recharge or discharge of its confined aquifers can occur at these locations.

2.5.6.2 Wanapum Basalt. The Wanapum Basalt consists of up to 26 flows that were erupted from vents and fissures some 15.6 to 14.5 million yr ago. This formation is the most extensively exposed of the Columbia Plateau. It has been formally divided into five members: Eckler Mountain, Frenchman Springs, Roza, Priest Rapids, and Onaway (Swanson et al. 1979) on the basis of chemistry, paleomagnetic polarity, lithology, and stratigraphic relationships. Its contact with the overlying Saddle Mountains Basalt is generally conformable, although local angular and erosional unconformities are known.

Aquifers of the Wanapum Basalt are confined to semiconfined. Recharge to this formation is thought to occur from (1) precipitation where the

Wanapum Basalt is not overlain by thick, younger basalts, (2) leakage from adjoining formations, and (3) surface and groundwater inflows from lands adjoining the Columbia Plateau. Within the Pasco Basin, recharge also occurs along the anticlinal ridges that bound the north and west parts of the basin. Intrabasin transfer and vertical leakage from adjacent formations also are believed to contribute to recharge and discharge of the Wanapum Basalt.

2.5.6.3 Saddle Mountains Basalt. The Saddle Mountains Basalt is the youngest formation (14.5 to 6 million yr) of the Columbia River Basalt Group. It consists of 14 chemically diverse members. Up to 25% of the thickness between the top and bottom of this formation is comprised of thick sedimentary interbeds of the Ellensburg Formation or equivalent sediments. The maximum thickness of the Saddle Mountains Basalt within the Pasco Basin is approximately 290 m.

Lateral groundwater movement through flows of the Saddle Mountains Basalt occurs in a semiconfined system. Recharge and discharge of this system are thought to occur locally. Recharge occurs at the periphery of the Pasco Basin, along anticlinal ridges, and from the overlying and underlying aquifers. Significant recharge is also derived from irrigation of the Columbia Basin Project in the east and the northeast portion of the Pasco Basin (Gephart et al. 1979). Discharge is primarily to the Columbia River.

2.5.6.4 Intraflow Structures. Intraflow structures are primary, internal features that originated during the emplacement and consolidation of each basalt flow. These structures result from variation in cooling rates, degassing, thermal contraction, and interaction with surface water. Intraflow structures have groundwater flow properties that differ from those of the basalt formations as a whole. Consequently, the objectives of specific simulations may require that their hydrologic characteristics be included as distinct zones in the model.

Intraflow structures of a typical basalt flow are described according to their position in the flow: (1) flow top, (2) flow bottom, and (3) flow interior. Figure 2-5 depicts the various types of intraflow structures. The flow top is the chilled upper crust of the flow. It may consist of vesicular to scoriaceous basalt or it may be rubbly and brecciated. Flow top thicknesses are typically about 10% of the flow but may vary greatly. The flow bottom is predominantly a thin, glassy zone a few centimeters thick. The thickest flow bottoms observed in the Columbia River Basalt Group (as much as 30% of a flow) are associated with pillow-palagonite zones. Within the interior of a basalt flow, the predominant intraflow structures are zones characterized by patterns of cooling joints. These are commonly referred to as colonnade and entablature.

2.5.6.5 Cooling Joints and Tectonic Fractures. Cooling joints in the Columbia River Basalt Group result from tensional stress in response to the contraction of solidified portions of a flow as it cools at temperatures below the solidus (Spry 1962). As primary features, cooling joints are distinct from secondary tectonic fractures such as faults, shear zones, and joint sets. Tectonic fractures are typically closely spaced, occur in parallel or subparallel zones, and may have clay minerals and breccia associated with them. Fractures resulting from tectonic forces are believed to be much less prevalent than those resulting from primary cooling.

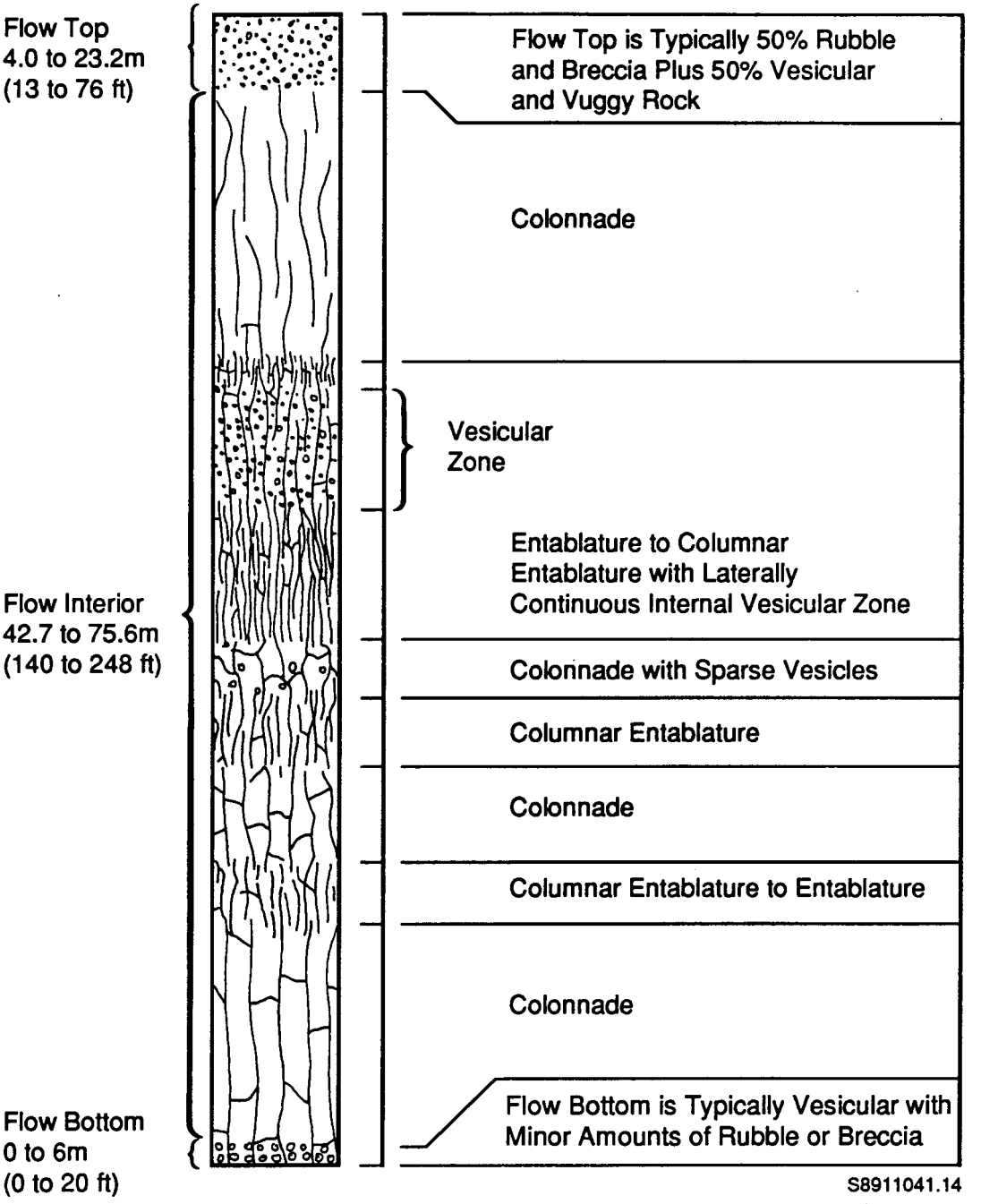

Figure 2-5. Typical Intraflow Structures of the Cohassett Flow.

At the Hanford Site, field studies (Lindberg 1986) of the primary cooling joints and fractures of the deep basalt flows have been made to collect data on width and infilling characteristics. Data on approximately 3,200 randomly selected primary cooling joints have been compiled from core samples. These data indicate that most fractures are completely filled by secondary minerals; in fact, only 19 of 3,200 were found to be at least

partially open. These observations suggest that very few discrete features need to be considered in simulating the groundwater system of the Hanford Site.

Nevertheless, some localized zones with discrete, unfilled, and extensively interconnected fractures are suspected to exist. Most of these zones may be associated with fracturing and faulting resulting from tectonic forces. Consequently, PORFLO-3 permits the program operator to include such features in the conceptual model if their properties are known.

2.5.7 Other Factors Pertaining to the Hanford Site Conceptual Model

The interior of Columbia River Basalt flows typically are very dense, with relatively low specific storage and hydraulic conductivity (DOE 1988), and low porosity (Leonhart et al. 1985). The entablature, which is generally below the flow top, is characterized by joint patterns that vary in orientation from nearly random to well-defined fanning columns. In contrast, the colonnade is composed of relatively uniform, vertically oriented, hexagonal columns (Long and WCC 1984). Because of its higher hydraulic conductivity, the basalt flow top generally forms the main pathway for groundwater movement. The amount of such detail included in a numerical simulation depends on the purpose of simulation, but for most large-scale simulations, the flow interiors and flow tops can be treated as distinct layers. For purposes of defining simulation problems at a regional scale, the combination of many flows into one composite layer would likely be appropriate.

Beneath the waste disposal areas of the Hanford Site, the basalt flows generally dip gently (less than a few degrees). Therefore, the choice of one axis of the model coordinate system as vertical and the other two as horizontal should be adequate to represent groundwater flow anisotropy.

The geology of the basalt flows beneath the Hanford Site indicates that their compressibility is small. The value of specific storage in the basalts varies between 10^{-4} and 10^{-7}. Consequently, the neglect of rock deformation will not cause appreciable error in the groundwater flow simulations.

Laboratory measurements of heat transfer parameters such as bulk density, specific heat, and thermal conductivity have been obtained from block tests and tests on intact core samples from various basalt flows from beneath the Hanford Site. These data (Sublette 1983) indicate that the average values for different basalt flows are very similar, suggesting that (1) there are no significant differences in thermal properties across a dense flow interior and (2) the average values are generally independent of horizontal location within a basalt flow. In addition, available data indicate that the thermal properties of the basalts are relatively weak functions of temperature. These considerations suggest that a relatively simple conceptual model for heat transfer is adequate.

Groundwater velocities in deep basalts with natural hydraulic gradients have been estimated to be small (Clifton 1986). This is primarily because of the small in situ hydraulic gradients and small hydraulic conductivities. Consequently, assumption of local thermal equilibrium between the geologic media and fluid is tenable, and the rate of convective heat transfer is

relatively small. In terms of numerical significance, the buoyancy term of PORFLO-3 is probably the term of most importance in coupling fluid flow and heat transfer. Next in importance is the change in hydraulic conductivity caused by changes in the fluid density and viscosity because of thermal variations. The transient source term for the fluid is of comparatively minor significance.

The buoyancy term has been found to be significant for the simulation of fluid migration in the saturated zone of the Hanford Site. The vertical hydraulic gradients of the Site in areas free of man-made heat sources are known to be small (on the order of 10^{-3} to 10^{-4}). However, thermal buoyancy can locally (close to the thermal source) create hydraulic gradients of up to two orders of magnitude greater than that of thermally undisturbed sites.

3.0 MATHEMATICAL BASIS

Three governing equations form the mathematical basis of PORFLO-3. The three dependent variables are (1) fluid pressure (or hydraulic head), (2) temperature, and (3) solute concentration. Application of the classic principles of the conservation of mass, momentum, and energy lead to these equations. Several auxiliary equations, including the equation of state and the constitutive equations, supplement the governing equations. In PORFLO-3, these equations are solved in three-dimensional Cartesian or radial coordinate systems. The theoretical basis of these equations is well known and is described in detail by several texts (e.g., Bear 1972). The specific form of the equations employed in PORFLO-3 is described in the following sections.

3.1 EQUATION FOR FLUID FLOW

3.1.1 The Equation of Continuity

Consider an arbitrary control volume, V, that is bounded by a control surface, S, as shown in Figure 3-1. The control volume is filled with rock or soil of uniform properties; it may contain regular planar (e.g., fractures and clastic dikes) or linear features (e.g., boreholes). The implication of the planar and linear features for the governing equations will be explained later.

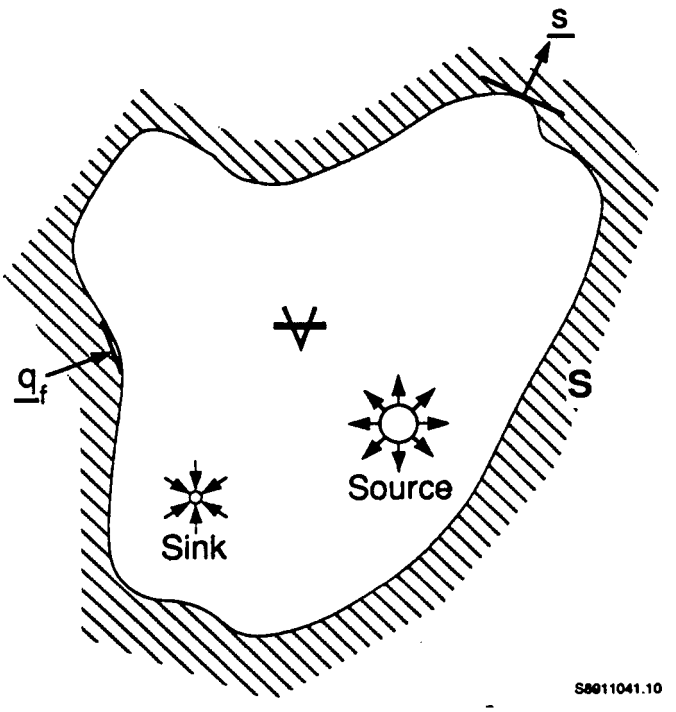

Figure 3-1. Illustration of Control Volume Concept.

The rock or soil is conceived of as having three types of pores. The first type is interconnected and permits fluid flow. Such pores constitute the effective (or flow) porosity, n_E, of the geologic media. The second type of pores does not participate in fluid flow but is nevertheless filled with liquid and does participate in heat and mass diffusion. The sum of the effective porosity and the porosity provided by these pores is termed diffusive porosity, n_D. The third type of pores is isolated from other pores and participates neither in fluid flow nor in heat and mass diffusion. These isolated pores, however, conduct heat. The sum of the effective porosity, diffusive porosity, and the porosity provided by these isolated pores is termed total porosity, n_T. The effective porosity, n_E, in the control volume is assumed to be partitioned between liquid water and air. For conditions in which all of the n_E is filled with liquid water, the medium becomes fully saturated with liquid. The solids, liquid, and air (when present) are assumed to exist as continuous phases in the control volume.

The mass of the liquid, M, at time, t, in volume, V, is given by the integral

$$M = \int_V n_E \, \sigma \, \rho \; dV, \tag{3.1-1}$$

where σ is the liquid saturation (volume of liquid water/diffusive porosity), and ρ is the liquid density. With time, M may vary either because of the liquid crossing the surface, S, or because fluid may be directly injected into, or withdrawn from, the interior of V.

The incoming fluid flux, q_f, at the bounding surface, S, can be written as

$$q_f = \int_S \rho \, \vec{V} \cdot \vec{s} \; dS, \tag{3.1-2}$$

where $\vec{V}$ is the apparent velocity vector of fluid and $\vec{s}$ is a unit vector normal to the surface, S. Note that the velocity in Equation 3.1-2 is not the real (pore) fluid velocity because flow is assumed to occur through the entire surface, S, irrespective of whether a specific point on it is occupied by a solid particle or a pore. In the following section, this velocity is identified as the Darcy velocity. By application of the Gauss divergence theorem, Equation 3.1-2 becomes

$$q_f = \int_V \vec{\nabla} \cdot (\rho \, \vec{V}) \; dV. \tag{3.1-3}$$

Assuming an internal mass injection rate of m per unit volume, the principle of mass conversion requires that

$$\partial_t \int_V \theta \, \rho \; dV + \int_V \vec{\nabla} \cdot (\rho \, \vec{V}) \; dV = \int_V m \; dV, \tag{3.1-4}$$

where $\theta = n_D \cdot \sigma$ is the volumetric moisture content. Assuming that the product $(\theta\rho)$ is at least once differentiable in time and that deformation of V is small, as discussed in Section 2.2.1 (see Abriola 1984 for a derivation with large deformations),

$$\int_V [\, \partial_t(\theta\, \rho) + \vec{\nabla} \cdot(\rho\, \vec{V}) - m] \, dV = 0. \qquad (3.1\text{-}5)$$

Because the volume, V, is assumed to be arbitrary, for Equation 3.1-5 to hold:

$$\partial_t(\theta\, \rho) + \vec{\nabla} \cdot(\rho\, \vec{V}) - m = 0. \qquad (3.1\text{-}6)$$

Equation 3.1-6 is the continuity equation for liquid water. A similar continuity equation can also be written for the gas phase. However, in the present version of PORFLO-3, the gas phase is assumed to be at atmospheric pressure and passive, and therefore, its motion is not considered.

3.1.2 Darcy's Law for Flow Dynamics

The velocity vector, $\vec{V}$, in Equation 3.1-6 must be obtained from dynamic considerations. Applications of the principle of conservation of momentum leads to the Navier Stokes equations (Bear 1972). For laminar flow with low velocities through porous media, the much simpler Darcy's equation is employed. Darcy's equation, which originated from experimental observations, has subsequently been derived from basic principles by assuming that the inertial forces are negligible (Hassanizadeh 1986a,b). This equation is

$$\vec{V} = -(\underset{\approx}{k}_S\, k_r/\mu)\, \{\vec{\nabla}\, p + \rho\, g\, \vec{\nabla}\, z\}, \qquad (3.1\text{-}7)$$

where $\underset{\approx}{k}_S$ is the saturated intrinsic permeability tensor, k_r (scalar) is the relative permeability, μ is the fluid dynamic viscosity, p is the thermodynamic pressure, g is the acceleration due to gravity, and z is the coordinate in the vertical direction. The x and y coordinates are assumed to be in the horizontal plane.

In Equation 3.1-7, $\underset{\approx}{k}_S$ is a property of the porous medium. For anisotropic media, $\underset{\approx}{k}_S$ is a tensor of the second order. For the equations in PORFLO-3, it is assumed that the coordinate directions coincide with the principal directions of $\underset{\approx}{k}_S$, so that all the off-diagonal components of the $\underset{\approx}{k}_S$ tensor are zero. On the other hand, k_r is a scalar and is unity for fully saturated media. For partially saturated media, $k_r < 1$. The estimation of k_r will be discussed in Section 3.7.3. An additional assumption is that gravitational acceleration acts in a direction opposite to the positive direction of the z-coordinate.

The limits of applicability of the Darcy flow equation for saturated flows have been explored by several investigators (e.g., Bear 1972; Cheng 1978). These researchers generally believe that Equation 3.1-7 is applicable without appreciable error for flows with a Reynold's number of less than 10, where the Reynold's number is based on a representative grain size of the equivalent porous medium.

3.1.3 Governing Equation for Hydraulic Head

Substitution of Equation 3.1-7 in Equation 3.1-6 leads to an equation for fluid pressure:

$$\partial_t(\theta\,\rho) - \vec{\nabla}\cdot\{(\underset{\approx}{k}_s\, k_r\, \rho/\mu)\,(\vec{\nabla}p + \rho\, g\, \vec{\nabla}z)\} - m = 0. \qquad (3.1\text{-}8)$$

To simplify Equation 3.1-8, a new variable, P, is defined as

$$P = (p/\rho^* g) + z - z^*, \qquad (3.1\text{-}9a)$$

or

$$P = -\psi + z - z^*, \qquad (3.1\text{-}9b)$$

where ρ^* is the reference fluid density at a reference temperature and pressure, z^* is an arbitrarily defined datum from which z is measured, and g is the gravitational acceleration. Although a datum may be arbitrarily selected, it is most convenient to assign it to the water table, ground surface, or mean sea level elevation. Although z^* may be assigned any numerical value, it is usually convenient to give it a value of zero by locating the origin of the coordinate axes at the datum.

The new variable, P (units of length), is a normalized pressure that is equivalent to hydraulic head defined with respect to the reference density ρ^*. However, P is not a true potential function because potential would be defined with respect to the local fluid density. The thermodynamic pressure, p, is negative (less than atmospheric pressure, which is taken to be zero) in partially saturated media and is positive in fully saturated media. For partially saturated systems, soil-moisture tension, ψ, is defined as indicated in Equation 3.1-9b. Soil-moisture tension is defined only when $\sigma < 1$ and is positive.

To obtain a more convenient form of Equation 3.1-8, the time derivative occurring in Equation 3.1-8 is expanded as follows:

$$\partial_t(\theta\,\rho) = \theta\,\partial_t(\rho) + \rho\,\partial_t(\theta). \qquad (3.1\text{-}10)$$

The fluid density, ρ, is, in general, a function of pressure (p), and temperature (T); i.e.,

$$\rho = \rho(p,T), \qquad (3.1\text{-}11a)$$

and, therefore,

$$\partial_t(\rho) = \partial_p(\rho)\big|_T \partial_t(p) + \partial_T(\rho)\big|_p. \qquad (3.1\text{-}11b)$$

Defining fluid compressibilities, β_p, as

$$\beta_p = (1/\rho)\, \partial_p(\rho)|_T, \tag{3.1-12a}$$

and the fluid thermal expansion coefficient, β_T, as

$$\beta_T = -(1/\rho)\, \partial_T(\rho)|_p, \tag{3.1-12b}$$

Equation 3.1-11b becomes

$$\partial_t(\rho) = \left[\beta_p\, \partial_t(p) - \beta_T\, \partial_t(T)\right] \rho, \tag{3.1-13a}$$

or, in terms of P,

$$\partial_t(\rho) = \left[\beta_p\, \rho^*\, g\, \partial_t(P) - \beta_T\, \partial_t(T)\right] \rho. \tag{3.1-13b}$$

The volumetric moisture content, θ, in Equation 3.1-10 is a product of diffusive porosity (n_D) and saturation (σ). For saturated media, $\sigma = 1$ (constant) and n_D is a much stronger function of p than it is of T. For unsaturated media, n_D remains constant and σ varies. Consequently, for saturated media ($\sigma = 1$), neglecting temperature effects on n_D, the variation of θ may be written as

$$\partial_t(\theta) = \partial_t(n_D) = \partial_p(n_D)\, \partial_t(p), \tag{3.1-14a}$$

and for unsaturated media

$$\partial_t(\theta) = n_D\, \partial_p(\sigma)\, \partial_t(p). \tag{3.1-14b}$$

Defining porous media compressibility, α_p, as

$$\alpha_p = \partial_p(n_D), \tag{3.1-15}$$

Equation 3.1-14a becomes, in terms of P,

$$\partial_t(\theta) = \alpha_p\, \rho^*\, g\, \partial_t(P), \tag{3.1-16a}$$

while Equation 3.1-14b, in terms of P, takes the form

$$\partial_t(\theta) = n_D\, \partial_p(\sigma)\, \partial_t(P). \tag{3.1-16b}$$

Substituting Equations 3.1-13b and 3.1-16a into Equation 3.1-10,

$$\partial_t(\theta\, \rho) = (\alpha_p + n_D\, \beta_p)\, \rho\, g\, \rho^*\, \partial_t(P) - n_D\, \rho\, \beta_T\, \partial_t(T) \text{ if } \sigma = 1, \tag{3.1-17a}$$

and for $\sigma < 1$, using Equation 3.1-16b,

$$\partial_t(\theta\, \rho) = n_D\, \partial_p(\sigma)\, \rho\, \partial_t(P) - \theta\, \rho\, \beta_T\, \partial_t(T),\ \sigma < 1. \tag{3.1-17b}$$

On the right-hand side of Equations 3.1-17a,b, the first term is a "storage" term; the second term depends on time variation of temperature and couples the pressure equation to the temperature equation. For fully saturated media ($\sigma = 1$), the coefficient of specific storage, S_s, is defined as

$$S_S = (\alpha_p + n_D \beta_p)\, \rho^* g. \quad (3.1\text{-}18a)$$

The units of S_S are (1/L) where L denotes length dimension (e.g., feet or meters). For partially saturated media ($\sigma < 1$), the coefficient of specific storage is taken to be

$$S_S = n_D\, \partial p(\sigma). \quad (3.1\text{-}18b)$$

Commonly, S_S for unsaturated media is written in terms of ψ, which is

$$S_S = -\, \partial\psi(\theta),\ \sigma < 1 \text{ (unsaturated)}. \quad (3.1\text{-}18c)$$

For unsaturated media, the ψ - θ relationship is known as the soil (or rock) characteristic curve and is experimentally determined. For saturated media, either the liquid and soil or rock compressibilities can be specified (from which the coefficient of specific storage can be estimated) or the coefficient of specific storage can be directly specified. The second option, that of specifying S_S, is adopted in PORFLO-3. The reason for specifying S_S (rather than compressibilities) for saturated media is that this parameter is usually directly estimated from analysis of pumping test data. In terms of S_S, the time derivative of Equation 3.1-8 becomes

$$\partial_t(\theta\, \rho) = \rho\, S_S\, \partial_t(P) - \theta\, \rho\, \beta_T\, \partial_t(T). \quad (3.1\text{-}19)$$

Substituting Equation 3.1-9a into the remaining term of Equation 3.1-8, this equation transforms to

$$\rho\, S_S\, \partial_t(P) = \vec{\nabla}\cdot\left\{(\underset{\approx}{k}_S\, k_r\, \rho\, \rho^*\, g/\mu)\, [\vec{\nabla}P + (R-1)\vec{\nabla}z]\right\} + \theta\, \beta_T\, \partial_t(T) + m, \quad (3.1\text{-}20)$$

where

$$R = \rho/\rho^* \quad (3.1\text{-}21a)$$

is the ratio of fluid densities. Setting the hydraulic conductivity, K, at reference fluid density

$$\underset{\approx}{K} = \underset{\approx}{k}\, \rho^*\, g/\mu^*, \quad (3.1\text{-}21b)$$

the buoyancy gradient, B, as

$$B = R - 1, \quad (3.1\text{-}21c)$$

the viscosity ratio, ξ, with reference viscosity μ^* as

$$\xi = \mu^*/\mu, \quad (3.1\text{-}21d)$$

and the volumetric source term, m_V, as

$$m_V = m/\rho^*, \quad (3.1\text{-}21e)$$

Equation 3.1-20 becomes

$$R\, S_S\, \partial_t(P) = \vec{\nabla}\cdot\left\{(R\, \xi\, \underset{\approx}{K}\, k_r/\mu)\, [\vec{\nabla}P + B\vec{\nabla}z]\right\} + \theta\, R\, \beta_T\, \partial_t(T) + m_V. \quad (3.1\text{-}22)$$

Equation 3.1-22 is the governing equation for pressure for single-phase fluid flow for nonisothermal conditions. The coefficient of specific storage, S_S, and the hydraulic conductivity tensor, $\underset{\approx}{K}$, in Equation 3.1-22 are at the reference values of fluid density (ρ^*) and viscosity (μ^*) and are, therefore, constant. These parameters are updated through the density and viscosity ratios, R and ξ, respectively, which vary with temperature. For example, R x S_S can be thought of as a coefficient of specific storage that varies with temperature. In its expanded form, considering both Cartesian and cylindrical coordinate systems, this equation is

$$R\,S_S\,\partial_t P = (1/r)\,\partial_x(rR\xi K_x\partial_x P) + \partial_y(R\xi K_y\partial_y P) + \partial_z\{R\xi K_z(\partial_z P + B)\}$$
$$+ \theta\beta_T R\,\partial_t T + m_v. \qquad (3.1\text{-}23)$$

Using Cartesian coordinates, $r \rightarrow \infty$; using cylindrical coordinates, r is the radial distance and is coincidental with the direction of the x-coordinate.

3.1.4 Equations for Velocity Components

The equations for the Darcy velocity are now written as

$$U = -K_x\,\partial_x P, \qquad (3.1\text{-}24a)$$

$$V = -K_y\,\partial_y P, \qquad (3.1\text{-}24b)$$

$$W = -K_z\,(\partial_z P + B), \qquad (3.1\text{-}24c)$$

where K_x, K_y, and K_z are the principal components of the hydraulic conductivity tensor, $\underset{\approx}{K}$, in the x, y, and z directions, respectively.

The average fluid velocity in the pores (i.e., the pore velocity) is obtained by dividing the Darcy velocity by the effective porosity, n_E. The effective (or flow) porosity, n_E, is different from the total porosity, n_T, in that n_E is only based on those pores that are interconnected and through which fluid flow occurs. These velocity components are given by

$$u = U / n_E, \qquad (3.1\text{-}25a)$$

$$v = V / n_E, \qquad (3.1\text{-}25b)$$

$$w = W / n_E. \qquad (3.1\text{-}25c)$$

3.2 EQUATION FOR HEAT TRANSFER

3.2.1 Conservation of Thermal Energy

From the first law of thermodynamics, it follows that the rate of change of the total energy of a system in a control volume, V, must be equal to the sum of the rate at which energy is added through the boundary, S, of the

control volume and the rate of energy generation inside the volume (see Figure 3-1) minus the rate at which work is done by the control volume on the surroundings.

In a general sense, the total energy of a system consists of (1) the internal energy caused by molecular motion; (2) the kinetic energy; (3) the potential energy; and (4) other energy forms such as electromagnetic, nuclear, and chemical.

Compared to the internal energy of the system, the changes in the kinetic and potential energy are negligible because the solid component of the fluid-solid matrix is nearly stationary, the fluid moves relatively slowly, and the gravitational (potential) force is time-independent and constant for all practical purposes (also see Bird et al. 1960). The other forms of energy mentioned above are also assumed to be negligible. Consequently, the rate of change of energy of the system, E, is given by

$$E = \partial_t \int_V \rho_e \, e_e \, dV, \tag{3.2-1}$$

where ρ_e is the effective mass density (i.e., composite density of the solid-fluid matrix) and e_e is the internal energy per unit mass of the fluid-solid matrix.

The rate at which energy enters the control volume, Q_T, is given by

$$Q_T = -\int_S (\rho \, \vec{V} \, e + \vec{q}_T + \vec{q}_D) \cdot \vec{s} \, dS, \tag{3.2-2}$$

where ρ is the fluid density, e is the internal energy of the fluid per unit volume, $\vec{q}_T$ is the energy flux created by thermal conduction, and $\vec{q}_D$ is the energy flux created by mechanical dispersion (Bear 1972). Other forms of energy exchange, such as those created by radiation and the Dufour effect, are assumed to be negligible.

With S_T as the rate of energy generation per unit volume of the system, the total energy generated in the control volume is given by

$$E_T = \int_V S_T \, dV. \tag{3.2-3}$$

The work done by the system on the surroundings is composed of external work and internal work because of the normal (pressure) and shear (viscous) forces in the fluid. In PORFLO-3, the former is assumed to be included in the S_T term and the latter is considered to be negligible because of the relatively low velocity of the fluid. (For an alternative argument that leads to the same conclusion, see Bird et al. 1960.)

In the equation expressing energy conservation for the control volume, V is obtained by combining Equations 3.2-1 through 3.2-3 as

$$\partial_t \left[\int_V \rho_e \, e_e \, dV \right] = -\int_S \left[\rho \, \vec{V} \, e + \vec{q}_T + \vec{q}_D \right] \cdot \vec{s} \, dS + \int_V S_T \, dV. \tag{3.2-4}$$

Employing the Gauss divergence theorem, the surface integral can be changed to a volume integral, and

$$\partial_t\left[\int_V \rho_e\, e_e\, dV\right] = -\int_V \vec{\nabla}\cdot\left[\rho\, \vec{V}\, e + \vec{q}_T + \vec{q}_D\right] dV + \int_V S_T\, dV. \qquad (3.2\text{-}5)$$

Because V is arbitrary, and assuming differentiability of $(\rho_e\, e_e)$,

$$\partial_t(\rho_e\, e_e) + \vec{\nabla}\cdot(\rho\, \vec{V}\, e) = -\vec{\nabla}\cdot(\vec{q}_T + \vec{q}_D) + S_T. \qquad (3.2\text{-}6)$$

3.2.2 Governing Equation for Temperature

For practical applications, it is more convenient to write Equation 3.2-6 in terms of temperature, T. Assuming that the fluid and solid are in thermal equilibrium, the internal energy of the fluid-solid matrix is given by

$$\rho_e\, e_e = \rho_e\, c_e\, T. \qquad (3.2\text{-}7)$$

The volumetric specific heat $(\rho_e\, c_e)$ of the composite solid-liquid matrix depends on the amount of liquid (the specific heat of gas is neglected) present in the matrix; i.e.,

$$\rho_e\, c_e = \eta_T\, \rho\, c_f + (1-n_T)\rho_S\, c_S, \qquad (3.2\text{-}8a)$$

where

$$\eta_T = n_T - n_D + \theta, \qquad (3.2\text{-}8b)$$

and

ρ_S = density of the solid matrix,
c_S = specific heat of the solid matrix,
c_f = specific heat of the pore liquid.

In writing Equation 3.2-8b, it is assumed that the pore space defined by n_T-n_E is filled with liquid. Although some of this liquid is immobile, it stores heat and participates in heat conduction. In saturated media, $\theta = n_D$ and the total porosity participates in heat conduction.

From Fourier's Law, the heat conduction term is written as

$$\vec{q}_T = -k_e\, \vec{\nabla}T, \qquad (3.2\text{-}9)$$

where the effective thermal conductivity of the fluid-solid matrix, R_e, is given by

$$k_e = \eta_T\, k_f + (1-n_T)\, k_S, \qquad (3.2\text{-}10)$$

with k_f and k_S as the coefficients of thermal conductivity for the fluid and the solid, respectively.

The mechanical dispersion (Bear 1972) term is written as

$$\vec{q}_D = - \rho\, c_f\, \eta_D\, \underset{\approx}{D}\, \vec{\nabla} T, \qquad (3.2\text{-}11)$$

where $\underset{\approx}{D}$ is a second-order tensor of mechanical dispersion, the nature of which is discussed in Section 3.4. Assuming that mechanical dispersion occurs only in the flowing fluid, η_D is defined as

$$\eta_D = \theta - (n_D - n_E). \qquad (3.2\text{-}12)$$

Substitution of Equations 3.2-7, 3.2-9, and 3.2-11 into Equation 3.2-6, with the assumption that $\rho_e\, c_e$ is independent of time, leads to the governing equation for temperature,

$$\rho_e\, c_e\, \partial_t T + \vec{\nabla} \cdot (\rho\, \vec{V}\, c_f\, T) = \vec{\nabla} \cdot \{(k_e + c_f\, \eta_D\, \underset{\approx}{D}) \vec{\nabla} T\} + S_T. \qquad (3.2\text{-}13)$$

In terms of the generalized three-dimensional coordinates of PORFLO-3, this equation is written as

$$\begin{aligned} c_e\, \partial_t T + (1/r)\, \partial_x (r \rho U c_f T) + \partial_y (\rho V c_f T) + \partial_z (\rho W c_f T) \\ = (1/r) \partial_x \left[r \left\{ k_e + \rho c_f \eta_D D_x \right\} \partial_x T \right] + \partial_y \left[\left\{ k_e + \rho c_f \eta_D D_y \right\} \partial_y T \right] \\ + \partial_z \left[\left\{ k_e + \rho c_f \eta_D D_z \right\} \partial_z T \right] + S_T. \end{aligned} \qquad (3.2\text{-}14)$$

3.3 EQUATION FOR MASS TRANSFER

3.3.1 Conservation of Chemical Species

The derivation of an equation for conservation of chemical species parallels that for the conservation of heat. From the principle of mass conservation, it follows that the rate of change of the mass of a chemical species in a control volume, V, must be equal to the sum of the rate at which the species is added through the boundary, S, of the control volume and the rate of species generation inside the volume (see Figure 3-1) minus the rate at which the species is consumed through chemical reaction or radioactive decay.

The rate of change of mass, M_C, of a species in control volume, V, is given by

$$M_C = \partial_t \left[\int_V C_e\, dV \right], \qquad (3.3\text{-}1)$$

where C_e is the mass density (or concentration) of the chemical species in the fluid-solid matrix per unit volume.

The rate, J_C, at which the species enters the control volume is given by

$$\vec{J}_C = -\int_S (\vec{V}\, C + \vec{j}_C + \vec{j}_D) \cdot \vec{s}\, dS, \qquad (3.3\text{-}2)$$

where C is the mass of the species in the fluid per unit volume of fluid, $\vec{j}_C$ is the species flux from diffusion, and $\vec{j}_D$ is the flux from dispersion (Bear 1972). Other forms of species exchange, such as those created by the Soret effect, are assumed to be negligible.

With S_C as the rate of mass species generation created by direct injection and chemical reaction per unit volume of the system, the rate of increase of the species, E_C, in the control volume is

$$E_C = \int_V S_C\, dV. \qquad (3.3\text{-}3)$$

With R_C as the rate of reaction or decay, the rate of disappearance of the chemical species because of either radioactive decay or an Arrhenius-type chemical reaction in the fluid-solid matrix, e_C, is given by

$$e_C = -\int_V R_C\, C_e\, dV. \qquad (3.3\text{-}4)$$

Given that the V is arbitrary, combining Equations 3.3-1 through 3.3-4 with the Gauss divergence theorem results in the following governing equation for the conservation of chemical species:

$$\partial_t C_e + \vec{\nabla}\cdot(\vec{V}\, C) = -\vec{\nabla}\cdot(\vec{j}_C + \vec{j}_D) + S_C - R_C\, C_e. \qquad (3.3\text{-}5)$$

3.3.2 Governing Equation for Species Concentration

The quantity Ce in Equation 3.3-5 depends on the way in which a chemical species is partitioned between the solid matrix and the fluid. Denoting by C and C_S the concentrations in the fluid and solid, respectively, C_e may be written as

$$C_e = \theta\, C + (1-n_T)\, C_S, \qquad (3.3\text{-}6)$$

assuming that no chemical species is contained in the isolated pores ($n_T - n_D$); i.e., the processes of convection, diffusion, and dispersion do not exchange mass in these pores. Consequently, the liquid in these pores participates only in heat conduction.

In PORFLO-3, adsorption-desorption processes are considered to be responsible for partitioning a radionuclide or chemical mass between the fluid and the solid phases. In general, descriptions of the sorption process may be grouped into two classes: local equilibrium models and disequilibrium models. For either class, sorption occurs at the interface between the liquid film and solid surface. The disequilibrium models assume that there

is a time-dependent mass exchange between the immobile and mobile liquids on the one hand, and between these liquids and the solid phase on the other (Goltz and Roberts 1988).

The more complex of these models assume a specific geometry (Sudicky and Frind 1982) for the immobile region and diffuse mass from the immobile to the mobile region. The disequilibrium models result in two concentration equations, one each for the mobile and the immobile regions, and require extra parameters to characterize the processes.

The local equilibrium models assume that the solid and liquid phases are in continuously reversible equilibrium; i.e., any change in the concentration in the liquid is accompanied by an instantaneous, corresponding change in the concentration in the solid phase. In addition, the concentration in the mobile and the immobile regions is assumed to be the same. In the simplest of these models included in PORFLO-3, the solid surface available for sorption is assumed to be inversely proportional to the density of solids. In addition, this model assumes that the sorption process is described by a linear Freundlich isotherm (Freeze and Cherry 1979) such that for saturated media

$$C_s = \rho_s \, k_d \, C, \tag{3.3-7a}$$

where k_d is variously called the distribution, sorption, or partition coefficient. Equation 3.3-7a implicitly assumes that the adsorption reaction is fully reversible; i.e., as the concentration, C, in the solution decreases, the mass adsorbed by the solids is released back into the solution.

One additional assumption regarding the extent of a wetted surface for conditions of variable saturation is required before Equation 3.3-7a can be used for unsaturated media. One assumption that could be made is that the fluid will wet all of the available solid surface, regardless of liquid saturation. With this assumption, which appears to be appropriate for higher saturations, no modification is required to Equation 3.3-7a. On the other hand, especially at lower saturations, an assumption could be made that some of the pores are dry and, therefore, the solid surface available for sorption is proportional to saturation. With such an assumption, Equation 3.3-7a is modified to

$$C_s = \sigma \, \rho_s \, k_d \, C. \tag{3.3-7b}$$

Substitution of Equation 3.3-7a into 3.3-6 leads to

$$C_e = \theta \, C + (1-n_T) \, \rho_s \, k_d \, C, \tag{3.3-8}$$

which can be written as

$$C_e = \theta C \left[1 + \frac{(1-n_T)\rho_s \, k_d}{\theta} \right]. \tag{3.3-9a}$$

On the other hand, substitution of Equation 3.3-7b into 3.3-6 leads to

$$C_e = \theta C \left[1 + \frac{(1-n_T)\rho_s \, k_d}{n_D} \right]. \tag{3.3-9b}$$

The quantity enclosed by the brackets in Equation 3.3-9a,b is termed the retardation coefficient, R_D. In terms of R_D, Equation 3.3-9a,b becomes

$$C_e = \theta R_D C. \tag{3.3-10}$$

In moving fluid, R_D depicts the ratio between the migration velocity of the fluid and the migration velocity of the radionuclide or chemical species. In general, it is analogous to the heat capacity in the heat transfer equation or to specific storage in the flow equation. It represents the capacity of the medium to store the chemical species. In the present version of PORFLO-3, R_D is given in terms of the definition provided by Equation 3.3-9b. This definition is used because at higher saturations, $\theta \rightarrow n_D$, and at lower saturations, Equation 3.3-9b is more appropriate.

From Fick's Law, the diffusion flux term is written as

$$\vec{J}_C = - \theta D_M \vec{\nabla} C, \tag{3.3-11}$$

where D_M is the molecular diffusivity of species in the fluid. In saturated media, $\theta = n_D$ and the entire diffusive porosity participates in mass exchange through molecular diffusion.

The mechanical dispersion term is written as (Bear 1972)

$$\vec{J}_D = - \eta_D \underset{\approx}{D} \vec{\nabla} C, \tag{3.3-12}$$

where D is a second-order tensor of fluid dispersion that is discussed in Section 3.4.

Substitution of Equations 3.3-6 through 3.3-10 in Equation 3.3-5 leads to the species concentration equation

$$\partial_t(\theta R_d C) + \vec{\nabla}\cdot(\vec{V} C) = \vec{\nabla}\cdot\{(\theta D_M + \eta_D \underset{\approx}{D})\vec{\nabla} C\} + S_C - \theta R_d R_C C. \tag{3.3-13}$$

In terms of the generalized Cartesian or cylindrical three-dimensional coordinates of PORFLO-3, this equation is written as

$$\begin{aligned} \partial_t(\theta R_d C) &+ (1/r)\,\partial_x(r U C) + \partial_y(V C) + \partial_z(W C) \\ &= (1/r)\partial_x\{r(\theta D_M+\eta_D D_x)\,\partial_x C)\} + \partial_y\{(\theta D_M+\eta_D D_y)\partial_y C)\} \\ &+ \partial_z\{(\theta D_M+\eta_D D_z)\partial_z C)\} + S_C - \theta R_d R_C C. \end{aligned} \tag{3.3-14}$$

3.4 GOVERNING EQUATIONS FOR FRACTURES AND BOREHOLES

An obvious method of considering flow and transport through fractures (a method requiring no additional assumptions and therefore probably the most correct) would be to explicitly consider fractures as defining zones that are distinct from the adjoining rock (or soil) matrix. Such a method has been used by various researchers (e.g., Wang and Narasimhan 1985) for small-scale

problems in which only one or two fractures are involved. Significantly larger numbers of fractures would tax the memory capability of even the largest computer. This method has the advantage that pressures, temperatures, and concentrations have values in the fractures that are distinct from those in the rock, thus permitting a continuous exchange of fluid, energy, and species between the fractures and the adjacent media.

A second method of incorporating fractures (or other such features) is to treat them as part of a composite medium and not distinguish between the fractures and the rock. This method requires that the flow and transport properties of the composite medium be specified. This method is preferred for conditions in which numerous, randomly distributed fractures exist. In such cases, field testing usually would provide values of parameters for the composite medium. In any case, testing of each specific fracture would not be practical.

Both of the above methods require no new mathematical formulation for the fractures. Using the first method, a fracture would be treated as a three-dimensional domain, just like any element of the porous continua. Using the second method, the fracture would have no separate identity. A third method, which is intermediate in nature between these two, has also been incorporated into PORFLO-3. This method considers the fractures to be two-dimensional elements (and boreholes or other man-made subsurface excavations as one-dimensional elements) that are embedded in the three-dimensional rock or soil.

In the context of the groundwater flow and contaminant transport equations of PORFLO-3, the flow and transport would occur predominantly in the two dimensions of the fracture (i.e., the flux across the plates of fracture faces would be negligible) or along the one dimension of a borehole. Two important assumptions are made in this case: (1) pressure, temperature, and concentration in a fracture are the same as that of the adjoining rock and (2) at fracture intersections, complete mixing occurs. As will be explained in Chapter 4.0, these assumptions limit fluid, energy, and species exchange between the fractures and adjoining rock or soil to discrete points.

In general, both the fractures and the boreholes are considered to be filled with porous material; consequently, the flow is assumed to be Darcian. This assumption is not considered to be a limitation of the program because, even for open fractures, a Darcian flow equation is commonly invoked in which a surrogate hydraulic conductivity is specified based on the "cubic law" or a variant (Snow 1969; Sagar and Runchal 1982). The open boreholes or other man-made excavations usually act as internal boundary conditions with fixed heads and can be treated as such. For example, an open tunnel or shaft would be at atmospheric pressure, while an open borehole filled with water would be at hydrostatic pressure.

The governing equations for fluid flow, heat transfer, and mass transport in the fractures and boreholes are two- and one-dimensional analogs, respectively, of the corresponding three-dimensional equations and, hence, are not repeated here.

3.5 COUPLING TERMS

The pressure and the temperature equations are coupled to each other through the fluid properties and the velocity components. The matrix properties, specific storage coefficient, and hydraulic conductivities are functions of fluid density and viscosity (see Section 3.1.1). The latter, in turn, are functions of the temperature. (The dependence of these on pressure is neglected in PORFLO-3; see Section 3.7.) The buoyancy term, R, arises in response to differences in fluid densities created by the temperature field. This term accounts for the natural convection caused by the thermal field.

Another coupling comes from the fluid expansion term on the right side of Equation 3.1-23. This term contains a product of the fluid thermal expansion coefficient and the time-rate-of-change of temperature. In terms of relative magnitudes, the most important of these coupling effects usually arises from the buoyancy term. The fluid expansion term is usually the smallest for most hydrologic problems; it becomes important only if there is a rapid change in the temperature field. The pressure equation, in turn, determines the velocity components, which, in turn, provide the convective flux of the temperature equation. Strong coupling usually occurs between the pressure and temperature equations for most nonisothermal flow fields.

There is only a one-way coupling between the concentration equation and the pressure equation; that is, although the pressure field affects the concentrations through the velocity field, the reverse is not true. Having neglected the Dufour and Sorret effects, there is no direct coupling between the temperature and concentration equations. However, an indirect coupling between these two equations exists because of the dependence of the convective velocity on the buoyancy.

As stated earlier, the temperature and the concentration equations are coupled to the pressure equation through the convective velocities. The strength of this coupling depends on the magnitudes of the velocities. The ratio of the convective to dispersive transport of heat and species is known as the Peclet number. The solution of the temperature and concentration equations depends largely on the values of the Peclet number. In the absence of convective transport, the equations are fully parabolic. When transport by dispersion and diffusion is negligible compared to that caused by convection, the equations become hyperbolic. As will be seen in Chapter 4.0, the Peclet number plays a crucial role in proper descretization of these equations.

3.6 GENERAL FORM OF THE GOVERNING EQUATIONS

All three governing equations (3.1-23, 3.2-14, and 3.3-14) have a similar mathematical structure. All three are second-order, parabolic equations that can be represented by the general transport equation

$$a\,\partial_t F + (1/r)\partial_x(r\,b\,U\,F - r\,c_x\,\partial_x F) + \partial_y(b\,V\,F - c_y\,\partial_y F) + \partial_z(b\,W\,F - c_z\,\partial_z F) = S_F - s_F\,F, \qquad (3.6\text{-}1)$$

where F is the dependent variable (P, T, or C) and the various other coefficients and source terms are summarized in Table 3-1.

Table 3-1. Coefficients and Source Terms of the General Transport Equation for the Three Dependent Variables of PORFLO-3.

F	a	b	c_x	c_y	c_z	S_F	s_F
P	RS_s	0	$R K_x$	$R K_y$	$R K_z$	$m_v+\partial_z(RK_zB)+nR\beta_T\partial_t T$	0
T	$\rho_e c_e$	c	$k_e+\rho c\eta_T D_x$	$k_e+\rho c\eta_T D_y$	$k_e+\rho c\eta_T D_z$	S_T	0
C	θR_d	1	$\theta D_M+\eta_D D_x$	$\theta D_M+\eta_D D_y$	$\theta D_M+\eta_D D_z$	S_C	$\theta R_d R_C$

In discussing the solution of the governing equations in Chapter 4.0, reference will be made to Equation 3.6-1 and its generic dependent variable, F.

3.7 AUXILIARY EQUATIONS

In addition to the governing equations described in Sections 3.1 through 3.3, several auxiliary equations are needed for a complete description of the flow and transport processes. These auxiliary equations include a description of the initial and boundary conditions and equations of state that describe the dependence of the fluid and solid properties on pressure, temperature, and saturation. These equations are described in the following sections.

3.7.1 Fluid Properties

3.7.1.1 Fluid Density. The principal fluid for most applications of PORFLO-3 is a liquid. In general, fluid density is a function of both temperature and pressure. However, for most liquids the dependence of density on pressure is much smaller than that on temperature. For example, for water at 100 °C, compressibility is on the order of 10^{-6}, whereas the coefficient of thermal expansion is on the order of 10^{-4}. For this reason, changes in water density caused by pressure variations are ignored in PORFLO-3. However, it should be noted that if the fluid of interest is a gas, the pressure dependence of density may need to be accounted for.

Several equations relating water density to temperature have been published. Three of these are implemented in the PORFLO-3 computer program. The first relation is that recommended by Perry and Chilton (1973). With the density of water known to be ρ^* at temperature, T^*, the density, ρ, at temperature, T, is given by the equation

$$\rho = \rho^* [(T_c - T)/(T_c - T^*)]^A, \qquad (3.7\text{-}1)$$

where T_c is the critical temperature, and the value of the exponent, A, is obtained from experimental data through regression. With T_c = 647.3 K, T^* = 300 K, and ρ^* = 996.59 kg/m^3, the value of exponent A is found to be equal to 0.20. Perry and Chilton (1973) have tabulated the values of water density from experimental data. Comparison of this tabulation with Equation 3.7-1 demonstrates that from 4 to 200 °C the difference between density calculated using Equation 3.7-1 and that determined experimentally is < 1%. The maximum error increases to about 2.5% for temperatures up to 350 °C. This error decreases at higher pressures. If fluids other than water are being simulated, suitable values of T_c and A should first be determined.

The second relation for water density is the polynomial expression

$$\rho = A_1 + A_2 T + A_3 T^2 + A_4 T^3, \quad (3.7\text{-}2)$$

where A_1, A_2, A_3, and A_4 are empirical constants. The optimal values of these coefficients for water, which are valid for a temperature ragge of 0 to 50 °C, are given by Buretta (1972) (with ρ in kg/m^3 and T in °C) as

$$A_1 = 9.999317011 \times 10^{+2}, \quad (3.7\text{-}3a)$$

$$A_2 = 4.745080000 \times 10^{-2}, \quad (3.7\text{-}3b)$$

$$A_3 = -7.393800000 \times 10^{-3}, \quad (3.7\text{-}3c)$$

$$A_4 = 3.500000000 \times 10^{-5}. \quad (3.7\text{-}3d)$$

These are used as default values in the PORFLO-3 program. Other values may be specified by the user.

A third relation for density that is incorporated into PORFLO-3 is a linear function of temperature and concentration expressed as

$$\rho = \rho^* [1 + A_5(T^* - T) + A_6(C^* - C)], \quad (3.7\text{-}4)$$

where A_5 and A_6 are user-specified constants and * denotes a reference value.

3.7.1.2 Fluid Viscosity. In a manner similar to that for fluid density, the viscosity of liquids is, in general, a much stronger function of temperature than it is of pressure. Therefore, in PORFLO-3 the pressure dependence of viscosity is neglected. The PORFLO-3 program provides for three different options for calculating changes in fluid viscosity. The first relation for fluid viscosity is that given by Perry and Chilton (1973):

$$\mu = B_1 \exp (B_2/T), \quad (3.7\text{-}5)$$

where B_1 and B_2 are empirical constants and T is the temperature in Kelvin. For a temperature range of 0 to 350 °C, the optimal values of the coefficients B_1 and B_2 for water are 6.40 x 10^{-6} kg/(m•s) and 1436 K, respectively. The water viscosity obtained by using these coefficients is in kilograms per meter per second.

The second option for calculating water viscosity is the polynomial relation

$$\mu = B_3 + B_4 T + B_5 T^2 + B_6 T^3, \quad (3.7\text{-}6)$$

where B_3 through B_6 are empirical constants. The optimal values of these coefficients for a temperature range of 0 to 50 °C are given by Buretta (1972) as follows:

$$B_3 = -1.6872274 \times 10^{-3}, \quad (3.7\text{-}7a)$$

$$B_4 = 4.4676700 \times 10^{-5}, \quad (3.7\text{-}7b)$$

$$B_5 = 6.0209700 \times 10^{-7}, \quad (3.7\text{-}7c)$$

$$B_6 = -3.2788000 \times 10^{-9}, \quad (3.7\text{-}7d)$$

where the viscosity is in kilograms per meter per second and the temperature is in degrees Celsius.

A third option available in PORFLO-3 is the second-order exponential relation

$$\mu = \mu^* \exp[B_7(T^* - T) - B_8(T^* - T)^2], \quad (3.7\text{-}8)$$

where B_7 and B_8 are empirical constants, and the * denotes a reference value.

3.7.2 Hydraulic Properties of Saturated Media

It is evident from Equation 3.1-23 that the two main parameters in the saturated flow equation are the coefficient of specific storage and the hydraulic conductivity tensor. The dependence of both of these parameters on temperature is through their dependence on liquid properties. This dependence was made explicit in Equation 3.1-23 by using the density and viscosity ratios, R and ξ, respectively. Consequently, only the reference values of S_S and $\underset{\approx}{K}$ need to be specified for application of this equation to saturated flow.

3.7.3 Hydraulic Properties of Partially Saturated Media

Although a single governing equation (Equation 3.1-23) was written for flow in both saturated and unsaturated media, there are two major differences between flow in saturated and unsaturated media. In saturated flows, $k_r = 1$ and therefore is eliminated from Equation 3.1-23. For unsaturated flows, k_r depends on saturation, σ, and is less than 1. Although S_S is directly specified for saturated flow, this is not possible for unsaturated flow because S_S is the (negative) slope of the soil moisture - tension curve and also depends on saturation. As will be discussed below, because saturation depends on pressure head, the flow equation for unsaturated flow becomes nonlinear. This aspect will be further discussed in Chapter 4.0.

Because of the simultaneous presence of both the liquid (e.g., water) and gas (e.g., air) in unsaturated media, liquid-gas interfaces are formed throughout. These concave interfaces extend from grain to grain across each pore channel. The radius of curvature of each interface reflects the surface tension of that interface. Liquid in the unsaturated zone is held by these surface tension forces; the greater this force, the less moisture is retained. The relation between the tension forces and moisture content is dependent on soil (or rock) grain sizes and arrangements. However, this relation often is measured directly in the field and specified as a basic hydraulic property of the medium. In many soils, the θ - ψ relation is hysteretic; i.e., it has different shapes for wetting and drying episodes. In PORFLO-3, hysteretic effects are neglected.

3.7.3.1 Soil Moisture-Retention Curves. A typical θ - ψ curve is shown in Figure 3-2. This curve can be specified either as an analytic function or as a table. Three options for analytic functions are provided in PORFLO-3.

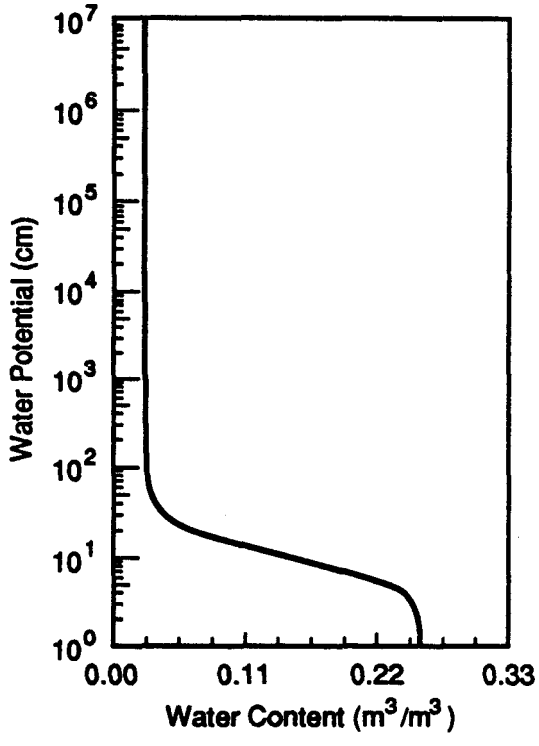

Figure 3-2. Typical Soil Moisture-Retention Curve.

- Van Genuchten (1978)

$$\theta^* = [1 + (\psi/\alpha)^n]^{-m}, \quad h < 0, \tag{3.7-9a}$$

$$\theta^* = 1, \quad h \geq 0, \tag{3.7-9b}$$

where α, m, and n are empirical constants, $h = -\psi$ is the pressure head, and θ^* is the normalized water content (or saturation), which is defined as

$$\theta^* = \frac{\theta - \theta_r}{n_D - \theta_r}, \tag{3.7-10}$$

in which θ_r is the residual (or immobile) moisture content. In PORFLO-3, because of the way the diffusive and effective porosities have been defined,

$$\theta_r = n_D - n_E. \tag{3.7-11a}$$

In addition, the coefficients m and n are related through

$$m = (1 - a/n), \tag{3.7-11b}$$

where a is 1 for Mualam and 2 for Burdine relations for hydraulic conductivity (Section 3.7.3.2).

- Brooks and Corey (1966)

$$\theta^* = (\psi/\psi^*)^{-\beta}, \quad h < -\psi^*, \tag{3.7-12a}$$

$$\theta^* = 1, \quad h \geq -\psi^*, \tag{3.7-12b}$$

where ψ^* is the air-entry head and β is an empirical constant. From Equation 3.7-12a, it is apparent that when $\psi = \psi^*$, $\theta^* = 1$; i.e., full saturation is approached as $\psi \rightarrow \psi^*$. Thus, for $\psi < \psi^*$, the soil is saturated. No analogous cutoff point is stipulated in the Van Genuchten relation.

- Tabular Specification

Any arbitrary soil-moisture curve can be specified in the form of a θ - ψ table. The value of θ corresponding to a value of ψ that is not in the table can be obtained through interpolation. Linear interpolation is used in PORFLO-3.

3.7.3.2 Relative Hydraulic Conductivity Curves. Measurement of in situ unsaturated hydraulic conductivity is difficult. Therefore, unsaturated hydraulic conductivities (or relative conductivity, k_r, of Equation 3.1-7) are usually estimated based on physical attributes of the porous media (e.g., pore radii, porosity, and tortuosity factor). The simplest formula for k_r is based on a generalization of Kozney's approach (Brutsaert 1967):

$$k_r = (\theta^*)^\gamma, \tag{3.7-13}$$

where γ is an empirical coefficient. A value for γ of 3.5 (Averjanov 1950) has been found to agree well with experimental observations.

Other, more complex formulae for k_r have been derived using the basic theory of capillary flow. Burdine (1953) derived the following relation:

$$k_r = (\theta^*)^2 \int_0^{\theta^*} \frac{1}{\psi^2}\, d\theta \;/\; \int_0^1 \frac{1}{\psi^2}\, d\theta. \qquad (3.7\text{-}14)$$

Substituting the Van Genuchten relation, Equation 3.7-9a, into 3.7-14, the following relation for k_r is obtained:

$$k_r(\theta^*) = \theta^* 2[1-(1-\theta^{*1/m})m. \qquad (3.7\text{-}15a)$$

If the Brooks and Corey moisture retention curve, Equation 3.7-12a, is used instead, the following formula is obtained:

$$k_r(\theta^*) = \theta^{*(3+2/\beta)}. \qquad (3.7\text{-}15b)$$

By setting $\beta = [2/(\gamma-3)]$, Equation 3.7-15b reduces to Equation 3.7-13.

The formulae for k_r also can be written in terms of ψ. The formula corresponding to the Van Genuchten moisture retention curve is

$$k_r(\psi) = \frac{1-(\psi/\alpha)^{n-2}\,[1+(\psi/\alpha)]^{-m}}{[1+(\psi/\alpha)^n]^{2m}}, \qquad (3.7\text{-}16a)$$

while for the Brooks and Corey moisture retention curve, it is

$$k_r(\psi) = (\psi/\psi^*)^{-2-3\beta}. \qquad (3.7\text{-}16b)$$

Mualem (1976) used a pore-size distribution in the modified form of the Childs and Collis-George (1950) relation to obtain the following for k_r:

$$k_r = (\theta^*)^{\frac{1}{2}} \int_0^{\theta^*} \frac{1}{\psi^2}\, d\theta \;/\; \int_0^1 \frac{1}{\psi^2}\, d\theta. \qquad (3.7\text{-}17)$$

Using Equation 3.7-17, the formula for k_r in terms of θ is, for Van Genuchten,

$$k_r(\theta) = \theta^{*\frac{1}{2}}\,[1 - (1 - \theta^{*1/m})m]2, \qquad (3.7\text{-}18a)$$

and for Brooks and Corey it is

$$k_r = \theta^{*(5/2 + 2/\beta)}. \qquad (3.7\text{-}18b)$$

The corresponding relations in terms of ψ become

$$k_r(\psi) = \frac{\{1-(\psi/\alpha)^{n-1}\,[1+(\psi/\alpha)]^{-m}\}^2}{[1+(\psi/\alpha)^n]^{m/2}}, \qquad (3.7\text{-}19a)$$

and

$$k_r(\psi) = (\psi/\psi^*)\text{-}2\text{-}3\beta. \qquad (3.7\text{-}19b)$$

Although other formulae for k_r have been published, those discussed above are used in PORFLO-3. In addition, an option is available to specify either the k_r - θ or the k_r - ψ curve in a table. In this case, linear interpolation is used to obtain the value of k_r for any ψ.

3.7.4 Mechanical Dispersion

Transport following mechanical dispersion is caused by the nature of flow in the interconnected pores of the media (Bear 1972). This phenomenon occurs only in moving fluid and is the result of the velocity variations at the pore scale.

In general, the coefficient of mechanical dispersion, $\underset{\approx}{D}$, is a second-order symmetric tensor (Bear 1972) and is a function of both the media and the fluid. To simplify this term, a set of parameters of the media, termed the dispersivities, is defined. Based on experimental evidence, longitudinal and transverse dispersivities are defined to represent the process of mechanical dispersion in, respectively, the direction of the average fluid velocity and orthogonal to it. As stated in Section 3.1.2, the x, y, and z coordinates in PORFLO-3 are assumed to coincide with the principal directions of the hydraulic conductivity. The average fluid velocity does not, in general, coincide with the x, y, or z axes. To obtain the components of the dispersion coefficient in the directions of the axes, the following equations suggested by Scheidegger (1961) are used:

$$D_X = \alpha_L U' + \alpha_T (V'+W'), \qquad (3.7\text{-}20a)$$

$$D_Y = \alpha_L V' + \alpha_T (W'+U'), \qquad (3.7\text{-}20b)$$

$$D_Z = \alpha_L W' + \alpha_T (U'+V'), \qquad (3.7\text{-}20c)$$

where α_L and α_T are, respectively, the longitudinal and transverse dispersivities and

$$\begin{aligned} U' &= U^2/\xi, \\ V' &= V^2/\xi, \\ W' &= W^2/\xi, \end{aligned} \qquad (3.7\text{-}21a)$$

where

$$\xi = (U^2 + V^2 + W^2)^{\frac{1}{2}}. \qquad (3.7\text{-}21b)$$

3.7.5 Boundary and Initial Conditions

The boundary conditions for the three governing equations can be represented in general as

$$- a\partial F/\partial N = b(F - F_o) + c, \quad (3.7\text{-}22)$$

where F represents P, T, or C, depending on the governing equation under consideration; N is a direction that is normal to the boundary; and a, b, c, and F_o are specified constants. By selecting appropriate values of a, b, c, and F_o, three types of boundary conditions can be represented by Equation 3.7-22. These boundary conditions are as follows:

- Dirichlet boundary condition: Obtained by specifying that a = c = 0, and b = 1. In other words, this condition is represented by

$$F = F_o, \quad (3.7\text{-}23a)$$

where F_o is the specified value of F at the boundary. This boundary condition also is known as a fixed head, temperature, or concentration boundary condition for the P, T, and C equations, respectively.

- Neumann boundary condition: Obtained by specifying that b = 0. In this case, a is equal to hydraulic conductivity, thermal conductivity, or the dispersion coefficient for the fluid flow, heat transfer, and mass transport equations, respectively. Thus, this boundary condition is

$$- a\partial F/\partial N = c, \quad (3.7\text{-}23b)$$

where c is the specified flux of fluid, heat, or chemical species per unit surface area of the boundary.

- Mixed (or radiation) boundary condition: Obtained by substituting c = 0 in Equation 3.7-22, resulting in

$$- a\partial F/\partial N = b(F - F_o). \quad (3.7\text{-}23c)$$

In this case, a has the same meaning as in the Neumann boundary condition; b is the fluid, heat, or mass transfer coefficient; and F_o is the equilibrium value of F. Using the heat transfer equation as an example, F_o may be specified to be the temperature of the atmosphere to which heat is being lost from the boundary of the domain under consideration.

The initial condition can be any reasonable value of the variable under consideration. For ease of specification, a linear variation in both the initial and boundary conditions is allowed; i.e.,

$$F = a + bx + cy + dz, \quad (3.7\text{-}24)$$

where a, b, c, and d are constants and x, y, and z are the coordinates of a point either in the interior of the domain or on its boundary.

4.0 NUMERICAL BASIS

Numerical solution of the governing and auxiliary equations described in Chapter 3.0 is by two steps: (1) using the Nodal Point Integration Method, the governing equations are discretized into a set of algebraic equations and (2) the matrix of algebraic equations is solved. Alternative choices of "integration profiles" in step 1 and different "matrix solution" methods in step 2 provide the adaptability to solve problems of increasing difficulty. This chapter is devoted to discussion of these two steps. Equation 3.6-1, the generic mass transport equation, provides a convenient basis for these discussions and will be referenced throughout this chapter.

4.1 DISCRETIZATION METHOD

The method of nodal point integration (Runchal 1969; Gosman et al. 1969; Patankar 1980) is employed to transform the differential equations into their algebraic analogs. The nodal point integration method is also referred to in the technical literature as the "finite-volume" or "integrated finite-difference" method. The essence of the nodal point integration method is to analytically integrate assumed profiles (polynomials, exponentials, etc.) for the dependent variable (F, in Equation 3.6-1) over a time step and finite volume that are defined by the calculational domain. Consequently, the nodal point integration method does not use the Taylor expansion method to represent derivatives, as is typically the case with finite-difference methods. In contrast, the nodal point integration approach resembles the finite-element method. However, it differs from the finite-element method in that integrations are performed on each finite volume, rather than on the total domain. This local nature of integration gives a significant advantage to the nodal point integration method; it intrinsically maintains the mass, momentum, and thermal energy balances at the local scale of an element and, thus, results in a stable numerical formulation.

The nodal point integration method implemented in PORFLO-3 provides a choice of two distinct integration profiles (or schemes) for discretization: the exponential (Spalding 1972) and the hybrid (Runchal 1972). However, the first step of the discretization process is to partition the total spatial domain into a set of finite volumes through the imposition of a grid, as explained below.

4.1.1 The Spatial Grid

The spatial grid used in PORFLO-3 is constructed using three mutually perpendicular surfaces. In the Cartesian coordinate system, these surfaces are identified by right-handed orthogonal (x,y,z), coordinates. In the cylindrical coordinate system, the orthogonal coordinates are r,θ,z, and the surface in the θ-z plane is circular. In both coordinate systems, the z-axis is taken to be vertical and is positive in the upward direction. In the following discussion, only the x,y,z notation is used, but the discussion can be applied to the r,θ,z system by substituting r for x and θ for y. The grids are depicted in Figures 4-1 and 4-2 for Cartesian and cylindrical

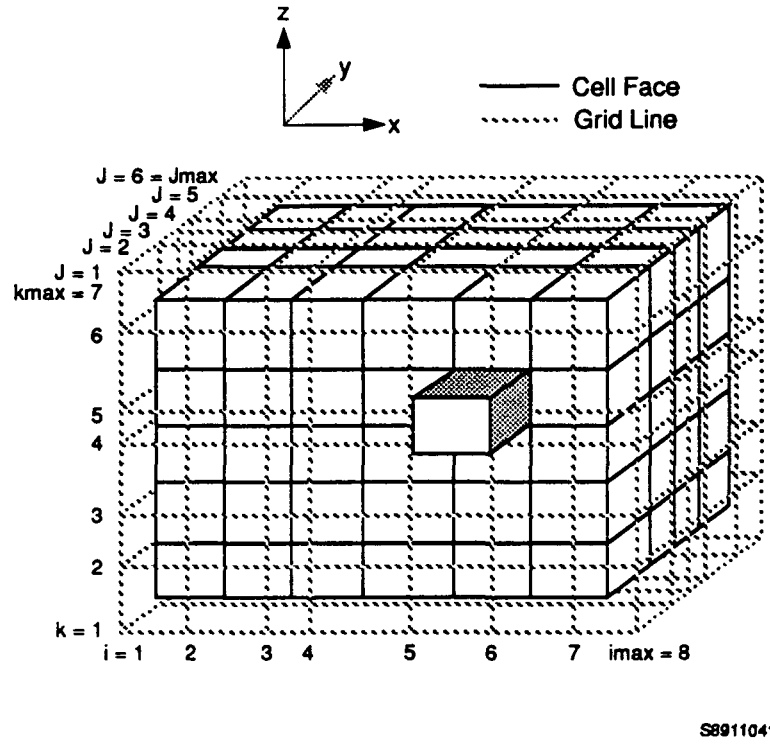

Figure 4-1. Illustration of Cartesian Grid Arrangement.

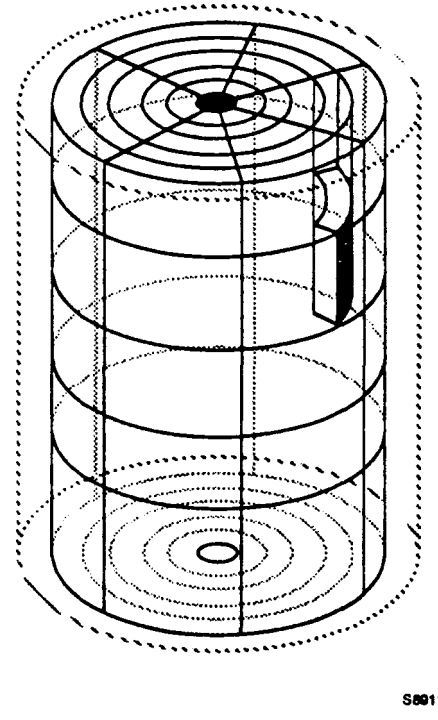

Figure 4-2. Illustration of Cylindrical Grid Arrangement.

coordinates, respectively. The dashed lines in these figures show the grid surfaces. Horizontal cross sections through these grids are shown in Figures 4-3 and 4-4.

In the following discussion, the grid surfaces (or grid lines in two dimensions) are identified by the indices I, J, and K in the x, y, and z directions, respectively. Within the domain of interest, these grid surfaces are numbered from 1 to IMAX, 1 to JMAX, and 1 to KMAX in the three respective directions. Grid nodes are points where the three mutually perpendicular surfaces intersect. The total number of nodes (internal plus boundary) in the domain of interest is thus IMAX x JMAX x KMAX.

The actual integration and solution of the governing equations of PORFLO-3 proceeds not by reference to the grid surfaces or nodes, but by reference to the elements. These elements also are variously referred to as the control volumes or cells. An element or control volume is associated with each internal grid node; i.e., all grid nodes except the boundary grid nodes. The control volume for each node is obtained by constructing surfaces that are located exactly midway between the grid surfaces. The cell surfaces are shown as solid lines in Figures 4-1 to 4-4. Because the grid surfaces in PORFLO-3 may be unevenly spaced, the control volume sizes associated with nodes may vary from node to node. The actual physical domain of a problem is thus completely encompassed by a discrete number of contiguous elements. The boundary nodes surrounding the physical domain are employed to impose the boundary conditions for the problem.

A typical cell or element for a Cartesian grid system is shown in Figure 4-5; one for a cylindrical grid system is shown in Figure 4-6. A horizontal cross section through the element of Figure 4-5 is shown in Figure 4-7. The node, P, enclosed by the cell has the grid indices I,J,K. The value of the dependent variable, F, at P (and at each internal node) is assumed to be influenced by its six immediate neighbors; these neighbors are denoted by E (east), W (west), N (north), S (south), U (up), and D (down). The respective indices for these nodes are I+1,J,K; I-1,J,K; I,J+1,K; I,J-1,K; I,J,K+1; and I,J,K-1. The cell faces are denoted, respectively, by e, w, n, s, u, and d. Each cell face lies exactly midway between the elemental node, P, and its nearest neighbor in the direction of the cell face. The number of internal nodes or, equivalently, the number of cells is (IMAX-2)*(JMAX-2)*(KMAX-2).

During numerical manipulations, all of the intrinsic property variables, such as pressure head, temperature, concentration, density, and viscosity, are defined at the grid nodes. On the other hand, the flux variables, such as velocity components, and heat and mass fluxes, are defined at the cell faces. The U velocity locations are midway between the grid nodes in the x direction, the V velocity locations are midway between the grid nodes in the y direction, and the W velocity locations are midway between the grid nodes in the z direction. The use of this "staggered" grid approach leads to a more natural description of the physical system, whereby the fluxes are defined at the element boundaries and the intrinsic properties are defined at the element node. The index notation employed is such that the velocity components at the W (west), S (south), and D (down) faces of the control volume are denoted by the same I, J, and K index values as the F values at the associated grid node (see Figure 4-7).

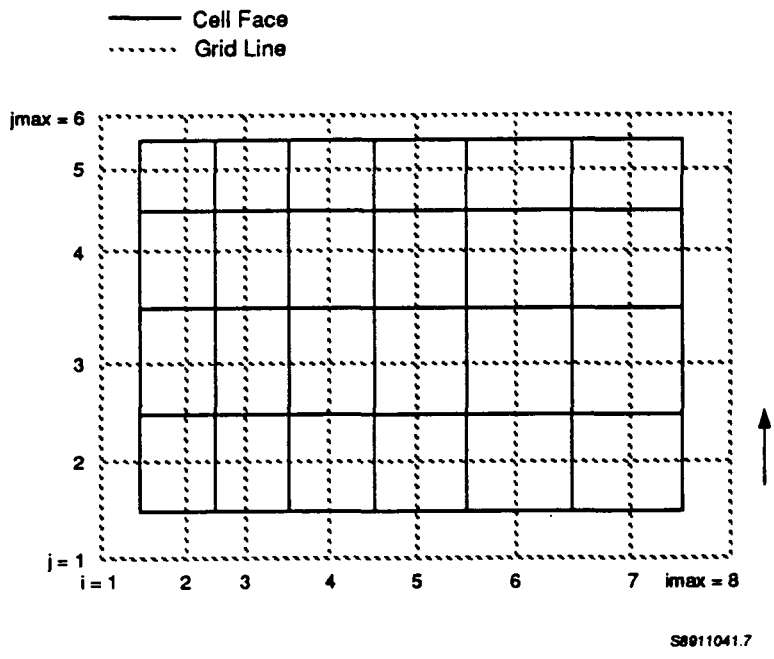

Figure 4-3. Horizontal Cross Section Through a Cartesian Grid System.

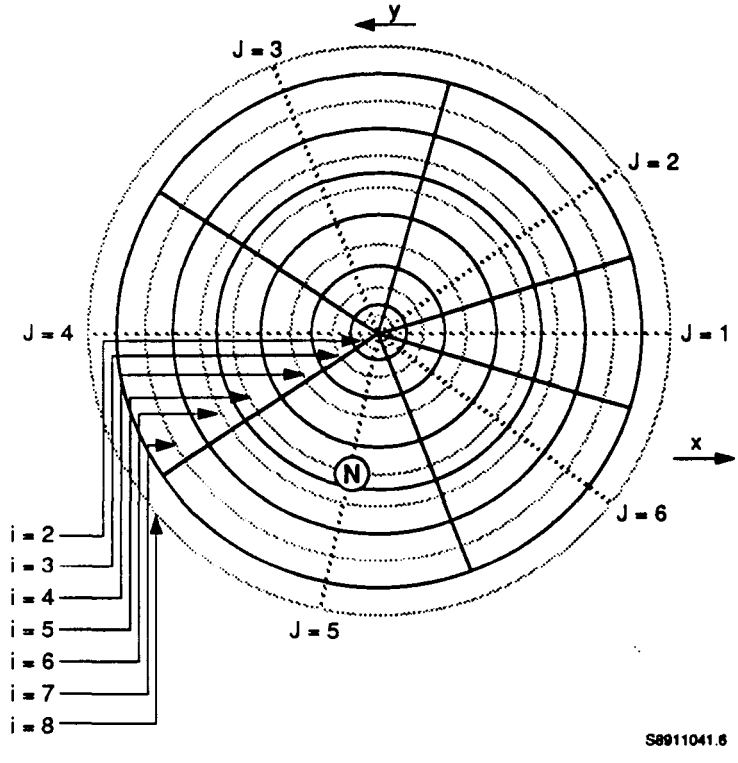

Figure 4-4. Horizontal Cross Section Through a Cylindrical Grid System.

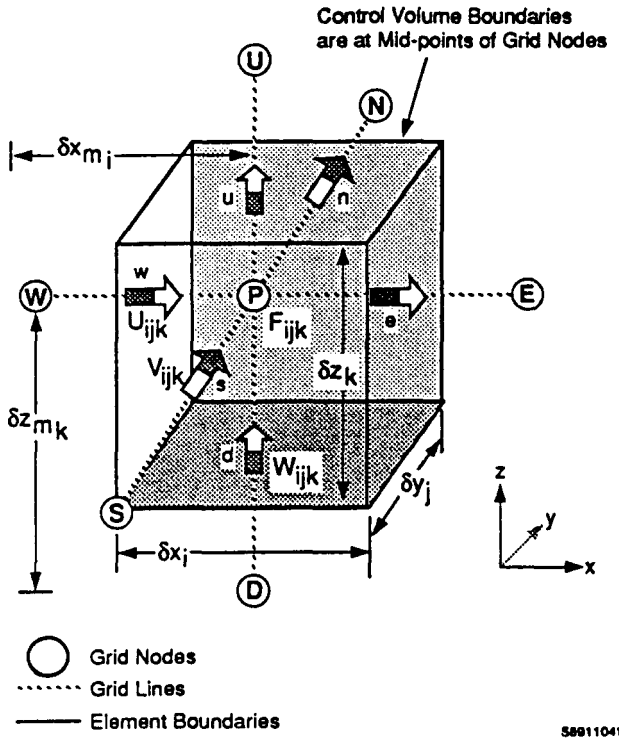

Figure 4-5. Typical Grid Cell in Cartesian Coordinates.

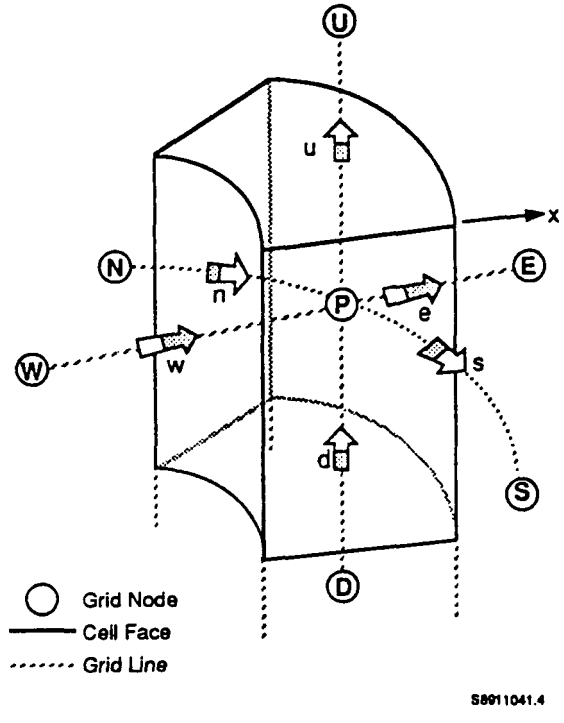

Figure 4-6. Typical Grid Cell in Cylindrical Coordinates.

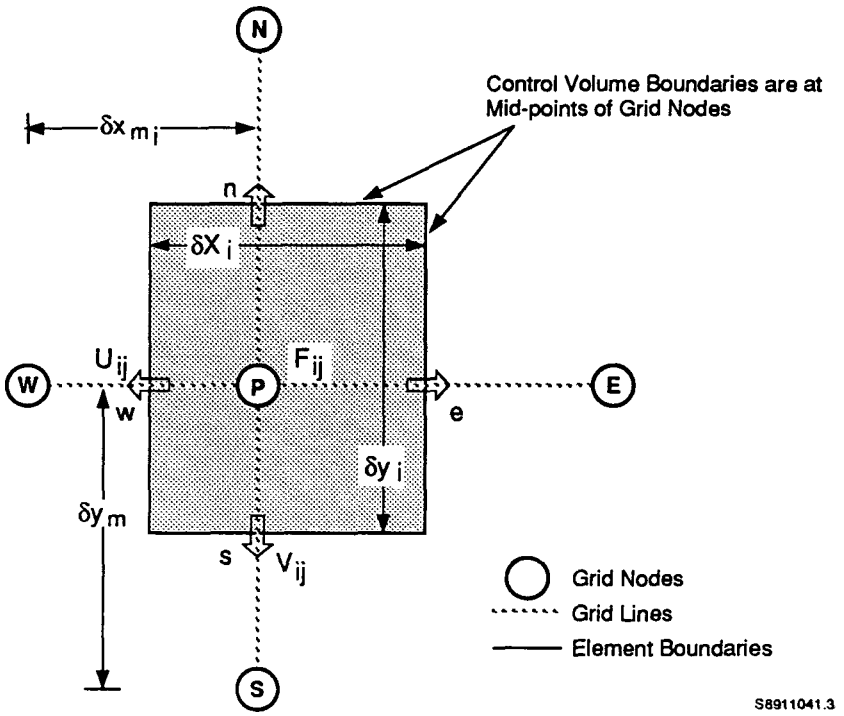

Figure 4-7. Horizontal Cross Section Through a Typical Grid Cell in Cartesian Coordinates.

4.1.2 General Formula for Discretization

Conceptually, the governing equations are discretized by integrating them over the volume of each cell and time step. Considering Equation 3.6-1 for a node, P, as shown in Figure 4-7, the integral is

$$\int_{t}^{t+\delta t} \int_{V_P} [\partial_t(a\ F) + L_x + L_y + L_z - S_F + s_F\ F\ ]\ dV\ dt\ = 0, \qquad (4.1\text{-}1)$$

where L_x, L_y, and L_z are partial derivative operators; i.e.,

$$L_x = r^{-1}\ \partial_x(r\ b\ U\ F - r\ c_x\ \partial_x F), \qquad (4.1\text{-}2a)$$

$$L_y = \partial_y(b\ V\ F - c_y\ \partial_y F), \qquad (4.1\text{-}2b)$$

$$L_z = \partial_z(b\ W\ F - c_z\ \partial_z F). \qquad (4.1\text{-}2c)$$

If a profile (polynomial or exponential) for F (and other terms, such as S_F) is assumed within the time interval, [t, t+δt], and over the volume, V, Equation 4.1-1 can be integrated analytically to obtain an algebraic equation applicable to node P. As will be seen later, different profile shapes for F may be used while integrating the convective (i.e., containing first-order derivatives of F) and diffusive (containing second-order

derivatives of F) terms in Equation 4.1-1. A similar procedure is followed to obtain an algebraic equation for each internal node. Further details are provided in Sections 4.1.3 and 4.1.4.

4.1.3 Temporal Integration

Assuming a linear time variation of F at node P(I,J,K), the time integral of the term containing the time derivative and the decay term of Equation 4.1-1 is

$$\int_t^{t+\delta t}\int_{\forall}\left[\partial_t(a\,F)+s_F\,F\right]d\forall\,dt=\int_{\forall}\left[a(F^{n+1}-F^n)+s_F\,F^{n+1}\right]d\forall. \qquad (4.1\text{-}3a)$$

In Equation 4.1-3a, F^{n+1} and F^n are the values of F at points in volume $d\forall$ at time steps (n+1) and n, respectively; i.e., $F^{n+1}=F(t+\delta t)$ and $F^n=F(t)$. For the remaining terms in Equation 4.1-1, the time integral is written as

$$\int_t^{t+\delta t}\int_{\forall}(L_x+L_y+L_z-S_F)\,d\forall\,dt = \delta t\left[\int_{\forall}(L_x^k+L_y^m+L_z^i-S_F^j)\,d\forall\right]. \qquad (4.1\text{-}3b)$$

The superscripts (k, m, i, and j) in Equation 4.1-3b denote the value at a time between t and t+δt of the specific quantity in which they occur. In terms of time steps, $n \le k,m,i,j \le n+1$. A choice of values of k, m, i, and j results in different numerical schemes and solution methods. The schemes used in PORFLO-3 are as follows.

1. k = m = i = j = n. That is, all values in Equation 4.1-3b are at the previous time step and, hence, are known. This is a fully explicit formulation. Only one unknown, F(t+δt), remains in the equation for a node. The Point Successive Over Relaxation method used in PORFLO-3 uses this type of formulation.

2. k = m = i = j = n+1. That is, all values in Equation 4.1-3b are at the new time step. In this case, values of F(t+δt) not only at node P, but at all of its neighboring nodes, appear in the equation for node P. This is the fully explicit formulation. The Cholesky Decomposition, Gaussian Elimination, and Reduced-System Conjugate-Gradient methods in PORFLO-3 use this formulation.

3. Three substeps are taken to complete the solution for a time step. In the first substep, k = n+1; in the second, m = n+1; and in the third, i = n+1; while all other superscripts are held equal to n. This formulation is used in conjunction with the Alternating-Direction-Implicit method of solution in PORFLO-3.

The various solution methods mentioned previously have distinctive accuracy and stability characteristics and differ greatly in required computer memory, as discussed in Section 4.4.

4.1.4 Spatial Integration

PORFLO-3 provides for alternative methods of spatial integration of the terms appearing in Equation 4.1-3a,b. From inspection of this equation, it can be seen that the spatial terms fall into four categories: diffusion terms with characteristic second-order spatial derivatives, the convection term with first-order spatial derivatives, the source and sink terms, and the accumulation terms with first-order time derivatives.

In the nodal point integration method, integration proceeds by assuming a suitable inter-nodal profile for the piecewise variation of the state variables (F of Equation 3.6-1) from one grid node to another. There are two approaches to the assumptions of these integration profiles. In the simpler approach, the diffusive and convective terms are considered separately, each with its own characteristic profile. The second approach provides a more comprehensive mathematical treatment by considering both the convective and the diffusive terms in a unified manner. Both approaches are illustrated below for the Cartesian coordinate system. The derivation of the equations proceeds in an identical manner for the cylindrical coordinate system.

4.1.4.1 Discretization of the Diffusive Terms. The integral of the x-directional component of the diffusion term in Equation 4.1-3b is written as

$$I_1 = \int_t^{t+\delta t} \int_{V_p} \partial_x(c_x \, \partial_x F) \, dV \, dt. \qquad (4.1\text{-}4)$$

By application of the divergence theorem, this equation is written as

$$I_1 = \int_t^{t+\delta t} \int_{S_{ijk}} \partial_x(c_x \, \partial_x F) \bullet \vec{s} \, dS \, dt, \qquad (4.1\text{-}5)$$

where S_{ijk} is the bounding surface of the element (I,J,K) and $\vec{s}$ is the unit outward, normal to this surface. In the Cartesian coordinate system, the surface is composed of six rectangular surfaces. Because of the orthogonality of the coordinate system and the rectangular shape of the elements, the contributions to the integral in the y and z directions are zero. Therefore, Equation 4.1-5 is written as

$$I_1 = \int_t^{t+\delta t} \left\{ \int_e \partial_x(c_x \, \partial_x F) \, dy \, dz - \int_w \partial_x(c_x \, \partial_x F) \, dy \, dz \right\} dt, \qquad (4.1\text{-}6)$$

where e and w denote the values of the quantity at the e and w faces of the element, as shown in Figure 4-7.

Further integration now proceeds by assuming that in the interval $x_{i-1} \leq x \leq x_{i+1}$, $y_{j-1} \leq y \leq y_{j+1}$, and $z_{k-1} \leq z \leq z_{k+1}$, the state variable, F, is represented by the following piecewise quadratic polynomial,

$$F = a_0 + a_1 x + a_2 x^2 + a_3 y + a_4 y^2 + a_5 z + a_6 z^2, \qquad (4.1\text{-}7)$$

where all of the "a" terms are arbitrary constants. This yields

$$\partial_x F|_w = a_1 + 2 a_3 x_{i-\frac{1}{2}}, \qquad (4.1\text{-}8a)$$

$$\partial_x F|_e = a_1 + 2 a_3 x_{i+\frac{1}{2}}. \qquad (4.1\text{-}8b)$$

Equation 4.1-7 also implies that, for nodes W, P, and E of Figure 4-7,

$$F_W = a_0 + a_1 x_{i-1} + a_2 x_{i-1}^2 + a_3 y_j + a_4 y_j^2 + a_5 z_k + a_6 z_k^2, \qquad (4.1\text{-}9a)$$

$$F_P = a_0 + a_1 x_i + a_2 x_i^2 + a_3 y_j + a_4 y_j^2 + a_5 z_k + a_6 z_k^2, \qquad (4.1\text{-}9b)$$

$$F_E = a_0 + a_1 x_{i+1} + a_2 x_{i+1}^2 + a_3 y_j + a_4 y_j^2 + a_5 z_k + a_6 z_k^2. \qquad (4.1\text{-}9c)$$

Because

$$x_{i-\frac{1}{2}} = (x_i + x_{i-1}) / 2, \qquad (4.1\text{-}10a)$$

$$x_{i+\frac{1}{2}} = (x_i + x_{i+1}) / 2, \qquad (4.1\text{-}10b)$$

Equations 4.1-9a-c yield

$$(F_P - F_W) / (x_i - x_{i-1}) = a_1 + 2 a_3 x_{i-\frac{1}{2}}, \qquad (4.1\text{-}11a)$$

$$(F_E - F_P) / (x_{i+1} - x_i) = a_1 + 2 a_3 x_{i+\frac{1}{2}}. \qquad (4.1\text{-}11b)$$

By comparison of Equations 4.1-8a,b and 4.1-11a,b,

$$\partial_x F|_w = (F_P - F_W) / (x_i - x_{i-1}), \qquad (4.1\text{-}12a)$$

$$\partial x F|_e = (F_E - F_P) / (x_{i+1} - x_i). \qquad (4.1\text{-}12b)$$

In the notation of Figure 4-7, these equations may be written more compactly as

$$\partial_x F|_w = (F_P - F_W) / \delta x_w, \qquad (4.1\text{-}13a)$$

$$\partial_x F|_e = (F_E - F_P) / \delta x_e, \qquad (4.1\text{-}13b)$$

where

$$\delta x_w = x_i - x_{i-1}, \qquad (4.1\text{-}14a)$$

$$\delta x_e = x_{i+1} - x_i. \qquad (4.1\text{-}14b)$$

Assuming that c_x remains constant across a cell face, Equation 4.1-6 is now written as

$$I_1 = \int_t^{t+\delta t} \{[c_{xe} (F_E-F_P)/ \delta x_e] A_e - [c_{xw} (F_P-F_W)/ \delta x_w] A_w\} dt, \quad (4.1\text{-}15)$$

where the cell face areas, A_e and A_w, are given by

$$A_w = (y_{j+\frac{1}{2}} - y_{j-\frac{1}{2}}) (z_{k+\frac{1}{2}} - z_{k-\frac{1}{2}}) = A_e. \quad (4.1\text{-}16)$$

Analogous to the discussion of the time integral provided above, to complete the transformation of this integral, assume that a representative value of F^m between $F(t)$ and $F(t+\delta t)$ exists. In general, this may be written as

$$F^m = \alpha F(t) + \beta F(t+\delta t), \quad (4.1\text{-}17)$$

where

$$\alpha + \beta = 1. \quad (4.1\text{-}18)$$

PORFLO-3 provides three choices for α and β; these are the fully explicit scheme with $\alpha = 1$, the implicit scheme with $\beta = 1$, and the ADI scheme with mixed values of α and β. The final form of the integral of Equation 4.1-15 is now written as

$$I_1 = B_W(F_W^m - F_P^m) + B_E(F_E^m - F_P^m), \quad (4.1\text{-}19)$$

where

$$B_W = c_{xw} A_w \delta t / \delta x_w, \quad (4.1\text{-}20a)$$

$$B_E = c_{xe} A_e \delta t / \delta x_e. \quad (4.1\text{-}20b)$$

In a similar manner, the integrals for the y and z directional diffusion terms may be written as

$$I_2 = B_S(F_S^m - F_P^m) + B_N(F_N^m - F_P^m), \quad (4.1\text{-}21)$$

$$I_3 = B_D(F_D^m - F_P^m) + B_U(F_U^m - F_P^m), \quad (4.1\text{-}22)$$

where

$$B_S = c_{ys} A_s \delta t / \delta y_s, \quad (4.1\text{-}23a)$$

$$B_N = c_{yn} A_n \delta t / \delta y_n, \quad (4.1\text{-}23b)$$

$$B_D = c_{zd} A_d \delta t / \delta y_d, \quad (4.1\text{-}23c)$$

$$B_U = c_{zu} A_u \delta t / \delta y_u, \quad (4.1\text{-}23d)$$

with

$$\delta y_s = y_j - y_{j-1}, \tag{4.1-24a}$$

$$\delta y_n = y_{j+1} - y_j, \tag{4.1-24b}$$

$$\delta z_d = z_k - z_{k-1}, \tag{4.1-24c}$$

$$\delta z_u = z_{k+1} - z_k, \tag{4.1-24d}$$

$$A_s = (z_{k+\frac{1}{2}} - z_{k-\frac{1}{2}})\ (x_{i+\frac{1}{2}} - x_{i-\frac{1}{2}}) = A_n, \tag{4.1-24e}$$

$$A_d = (x_{i+\frac{1}{2}} - x_{i-\frac{1}{2}})\ (y_{j+\frac{1}{2}} - y_{j-\frac{1}{2}}) = A_u. \tag{4.1-24f}$$

The values of the diffusion coefficients at the interfaces (i.e., the "c" terms of Equations 4.1-20a,b and 4.1-23a-d) are taken to be functions of the values at their nearest neighboring nodes. Four choices for these functions are available in PORFLO-3: (1) harmonic mean, (2) geometric mean, (3) arithmetic mean, and (4) upwind value. For c_{xw}, these four functional forms are, respectively,

$$c_{xw} = 2.\ c_{xW}\ c_{xP}\ /\ (c_{xW} + c_{xP}), \tag{4.1-25a}$$

$$c_{xw} = (c_{xW}\ c_{xP})^{\frac{1}{2}}, \tag{4.1-25b}$$

$$c_{xw} = (c_{xW} + c_{xP})\ /\ 2, \tag{4.1-25c}$$

$$c_{xw} = c_{xW},\ \text{if } U > 0;\ c_{xw} = c_{xP},\ \text{if } U < 0, \tag{4.1-25d}$$

where c_{xW} and c_{xP} are the values of the diffusion coefficient, c_x, at the nodes W and P (see Figure 4-7). For fully saturated flow problems, the harmonic mean option usually produces the best results; for unsaturated flow problems, the geometric mean options generally work best.

4.1.4.2 Discretization of the Convective Term. The integral of the x-directional component of the convection term in Equation 3.6-1 is written as

$$I_4 = -\int_t^{t+\delta t}\int_{\forall P} \partial_x(b\ U\ F)\ d\forall\ dt. \tag{4.1-26}$$

Proceeding in a manner similar to that for the diffusion term, this integral can be written as

$$I_4 = -\{\ b_e U_e^m\ F_e^m\ A_e - b_w U_w^m\ F_w^m\ A_w\}\ \delta t\ , \tag{4.1-27}$$

where

$$b_e = (b_E + b_P) / 2, \quad (4.1\text{-}28a)$$

$$b_w = (b_W + b_P) / 2, \quad (4.1\text{-}28b)$$

$$F_e = f_e F_E + (1 - f_e) F_P, \quad (4.1\text{-}28c)$$

$$F_w = f_w F_W + (1 - f_w) F_P. \quad (4.1\text{-}28d)$$

For the second order polynomial of Equation 4.1-7,

$$f_e = f_w = 1/2. \quad (4.1\text{-}29)$$

However, the use of the second-order polynomial for the convective terms may lead to numerical instability if the grid Peclet number exceeds a critical value of 2 (Patankar 1980). For example, in the present context, the grid Peclet number for the x-direction flux at location e of the control volume is defined by

$$P_e = b_e |U_e| \delta x_e / c_{xe}, \quad (4.1\text{-}30)$$

where x_e is the local grid size and U_e is the velocity component in the x-direction. To combat this instability, PORFLO-3 employs a hybrid approach (Spalding 1972; Runchal 1972) for selecting suitable values for the f's of Equation 4.1-28c,d. In this approach, the second-order polynomial of Equation 4.1-7 is employed if the local grid Peclet number is less than 2; otherwise, an upwind (or donor) scheme is employed. The values of the f's of Equation 4.1-28c,d are then given by

$$f_e = 0.5 - 0.25 \left\{P_e/|P_e|\right\} \left\{1 + \left[||P_e| - 2|\right] / \left[|P_e| - 2\right]\right\}, \quad (4.1\text{-}31a)$$

$$f_w = 0.5 + 0.25 \left\{P_w/|P_w|\right\} \left\{1 + \left[||P_w| - 2|\right] / \left[|P_w| - 2\right]\right\}. \quad (4.1\text{-}31b)$$

The convective integral of Equation 4.1-27 can now be written as

$$I_4 = C (F_E^m - F_P^m) + C_W (F_W^m - F_P^m) + (C_W' - C_P') F^m, \quad (4.1\text{-}32)$$

where

$$C_W' = b_w U_w^m A_w \delta t, \quad (4.1\text{-}33a)$$

$$C_E' = b_e U_e^m A_e \delta t, \quad (4.1\text{-}33b)$$

$$C_W = f_w |C_W'|, \quad (4.1\text{-}33c)$$

$$C_E = f_e |C_E'|. \quad (4.1\text{-}33d)$$

The convective integrals in the y and z direction are written by analogy as

$$I_5 = C_N(F_N^m - F_P^m) + C_S(F_S^m - F_P^m) + (C_S' - C_N') F_P^m, \quad (4.1\text{-}34)$$

$$I_6 = C_U(F_U^m - F_P^m) + C_D(F_D^m - F_P^m) + (C_D' - C_U') F^m, \quad (4.1\text{-}35)$$

where

$$C_S' = b_s U_s^m A_s \delta t, \quad (4.1\text{-}36a)$$

$$C_N' = b_n U_n^m A_n \delta t, \quad (4.1\text{-}36b)$$

$$C_D' = b_d U_d^m A_d \delta t, \quad (4.1\text{-}36c)$$

$$C_U' = b_u U_u^m A_u \delta t, \quad (4.1\text{-}36d)$$

$$C_S = f_s |C_S'|, \quad (4.1\text{-}36e)$$

$$C_N = f_n |C_N'|, \quad (4.1\text{-}36f)$$

$$C_D = f_d |C_D'|, \quad (4.1\text{-}36g)$$

$$C_U = f_u |C_U'|, \quad (4.1\text{-}36h)$$

where the "b" and "f" terms are defined in a manner analogous to that of Equations 4.1-28a-d and 4.1-31a,b.

4.1.4.3 Discretization of the Source Term. The source term, S_F of Equation 3.6-1, is discretized as

$$I_7 = \int_t^{t+\delta t} \int_{\forall P} S_F \, d\forall \, dt, \quad (4.1\text{-}37a)$$

$$= S_P^m \forall_P \delta t, \quad (4.1\text{-}37b)$$

where

$$\forall_P = (1/8)(x_{i+1} - x_{i-1})(y_{j+1} - y_{j-1})(z_{k+1} - z_{k-1}). \quad (4.1\text{-}38)$$

4.1.4.4 Discretization of the Decay-Rate Term. As indicated by Equation 4.1-3a, the decay-rate term, $s_F F$ of Equation 3.6-1, is always discretized at the time level $t+\delta t$; i.e.,

$$I_8 = \int_t^{t+\delta t} \int_{\forall P} s_F F \, d\forall \, dt, \quad (4.1\text{-}39a)$$

$$= s_P^{n+1} F_P^{n+1} \forall_P \delta t. \quad (4.1\text{-}39b)$$

4.1.4.5 Discretization of Accumulation Term. For this term, the F is assumed to remain constant within the cell so that

$$Ig = \int_t^{t+\delta t} \int_{\forall P} a\, \partial_t F \, d\forall \, dt, \tag{4.1-40a}$$

$$= a_P(F_P^{n+1} - F_P^{n+1})\, \forall P. \tag{4.1-40b}$$

4.1.5 Algebraic Analog of the General Transport Equation

The algebraic analog of the general transport equation (Equation 3.6-1) can be obtained by a combination of Equations 4.1-19 through 4.1-40. This analog is written as

$$\begin{aligned} a_P(F_P^{n+1} - F_P^n)\, \forall P \;=\; & A_E(F_E^m - F_P^m) + A_W(F_W^m - F_P^m) \\ & + A_N(F_N^m - F_P^m) + A_S(F_S^m - F_P^m) \\ & + A_U(F_U^m - F_P^m) + A_D(F_D^m - F_P^m) \\ & + S_P^m \forall P\, \delta t - s_P^{n+1} F_P^{n+1} \forall P\, \delta t \\ & - (C_W' - C_E' + C_S' - C_N' + C_D' - C_U')\, F_P^m, \end{aligned} \tag{4.1-41}$$

where

$$A_W = B_W + C_W, \tag{4.1-42a}$$

$$A_E = B_E + C_E, \tag{4.1-42b}$$

$$A_S = B_S + C_S, \tag{4.1-42c}$$

$$A_N = B_N + C_N, \tag{4.1-42d}$$

$$A_D = B_D + C_D, \tag{4.1-42e}$$

$$A_U = B_U + C_U, \tag{4.1-42f}$$

and the superscript, m, indicates the time (equal to n or n+1) at which various values are taken.

From the continuity equation, the last term on the right side of Equation 4.1-41 can be shown to be zero for incompressible fluids and negligible for fluids with small compressibility. Equation 4.1-41 can be written in a more compact form as follows:

$$A_P\, F^{n+1} = a_P\, \forall P\, F_P^n + \sum_M [A_M(F_P^m - F_P^m) + \sum_M (-1)^k\, C_M'\, F_P^m] + S_P^m\, \forall P\, \delta t, \tag{4.1-43}$$

where M takes values of E, W, N, S, U, and D, respectively; k = +1 for M = W, S and D; and K= -1 otherwise; and,

$$A_P = a_P + s_P^{n+1} \forall_P \, \delta t. \qquad (4.1\text{-}44)$$

PORFLO-3 provides for both the explicit and implicit versions of Equation 4.1-43 to be solved. The methods of solution are described later, in Section 4.4.

4.1.6 Exponential Integration Profile

The mathematical description given above employs a second-degree polynomial profile for the state variable, F (Equation 4.1-7), for spatial discretization of the convection and diffusion terms. A second alternative available in PORFLO-3 relies on piecewise exponential profiles for F. This choice is inspired by the analytic solution to the steady-state, one-dimensional version of the general transport Equation 3.6-1, which is

$$\partial_X(b\, UF - c_X\, \partial_X F) = \phi, \qquad (4.1\text{-}45)$$

when

$$F = Fp \quad at \quad x = xp, \qquad (4.1\text{-}46a)$$

$$F = F_E \quad at \quad x = x_E, \qquad (4.1\text{-}46b)$$

and ϕ is some constant. The exact solution of Equation 4.1-45, subject to Equation 4.1-46a,b, is

$$F = Fp + (F_E - Fp)\, \{\exp[b\, U(x - xp)/c_{xe}] - 1\} \,/[\exp(P_e - 1)]. \qquad (4.1\text{-}47)$$

Now, consider the following composite convection and diffusion integral for the cell face represented by e,

$$I_{10} = \int_t^{t+\delta t} \int_e (b\, U\, F - c_X\, \partial_X F)\, dy\, dz\, dt. \qquad (4.1\text{-}48)$$

Assuming an exponential profile for F, as indicated by Equation 4.1-47, the integral in Equation 4.1-48 can be evaluated as

$$I_{10} = b_e\, U_e\, \{(F_E - Fp) \,/\, (\exp P_e - 1) - Fp\}\ A_e\, \delta t. \qquad (4.1\text{-}49)$$

The coefficient A_E of Equation 4.1-43 now can be replaced by

$$A_E = b_e\, U_e \,/\, (\exp P_e - 1). \qquad (4.1\text{-}50)$$

The other integrals are evaluated in a similar manner. The A's of Equation 4.1-43 are thus replaced by expressions similar to those of Equation 4.1-50. All other terms of Equation 4.1-43 are evaluated as before.

4.2 ALGEBRAIC ANALOG OF FRACTURES, CLASTIC DIKES, AND BOREHOLES

It was stated in Section 3.4 that the governing equations for fractures, clastic dikes, and boreholes are the same as for the three-dimensional domain, except for their reduced dimensionality. The discretization of these equations proceeds exactly in the same manner as explained in the previous sections for the general, three-dimensional case.

The geometry of the two-dimensional fracture and the one-dimensional borehole elements is restricted by the model in two ways. First, these elements must be aligned with the grid lines of the three-dimensional elements; second, they must begin and end at nodes of the three-dimensional grid. The first limitation is restrictive because fractures and boreholes inclined to the grid lines cannot be represented except by ingenious grid designs that allow approximation of inclined fractures as "stair-stepped" features. The second limitation is not severe because grid points can be located anywhere in three-dimensional space.

The major theoretical assumption that simplifies inclusion of fractures, clastic dikes, and boreholes in three-dimensional domains is that the value of the state variable (pressure, temperature, or concentration) at the node of an element or control volume is common to the three-dimensional geologic continua, two-dimensional fracture, or one-dimensional borehole. That is, no interchange of fluid, heat, or species between the fracture and the surrounding rock is considered within each cell. However, the flux of fluid, heat, or mass moving into or out of a control volume is considered to be composed of two parts--fluid in the rock matrix and fluid in the fracture, dike, or borehole. Given this assumption, the set of algebraic equations obtained for the three-dimensional space can be modified to accommodate fractures and boreholes without introducing the need to solve a separate set of equations.

To explain the above concepts, consider a control volume or cell whose node is P, with grid indices (I, J, and K). Assume that the volume contains a one-dimensional borehole that is aligned with the x-direction of the model grid, as shown in Figure 4-8. Now, consider the discretization of the diffusion term. Because the borehole is aligned with the x-direction, it does not affect the transport of the quantity, F, in the y- and z-directions; i.e., Equations 4.1-21 and 4.1-22 remain unaltered. However, the integral, I_1 of Equation 4.1-4, would be modified as follows:

$$I_1 = \int_t^{t+\delta t} \int_{V_P} \{ \partial_x(c_{xR}\, \partial_x F) + \partial_x(c_{xF}\, \partial_x F) \}\, dV\, dt. \qquad (4.2\text{-}1)$$

Based on the derivations given in Section 4.1, the following expressions for B_E and B_W, modified from those given in Equation 4.1-20a,b, can be obtained:

$$B_W = (c_{xwR}\, A_{wR} + c_{xwF}\, A_{wF})\, \delta t \,/\, \delta x_w, \qquad (4.2\text{-}2a)$$

$$B_E = (c_{xeR}\, A_{eR} + c_{xeF}\, A_{eF})\, \delta t \,/\, \delta x_e. \qquad (4.2\text{-}2b)$$

Similar modifications are made to the convection terms. For calculating the convective term, the flow velocities in the fractures, dikes, and boreholes are accounted for separately from that of the porous continua.

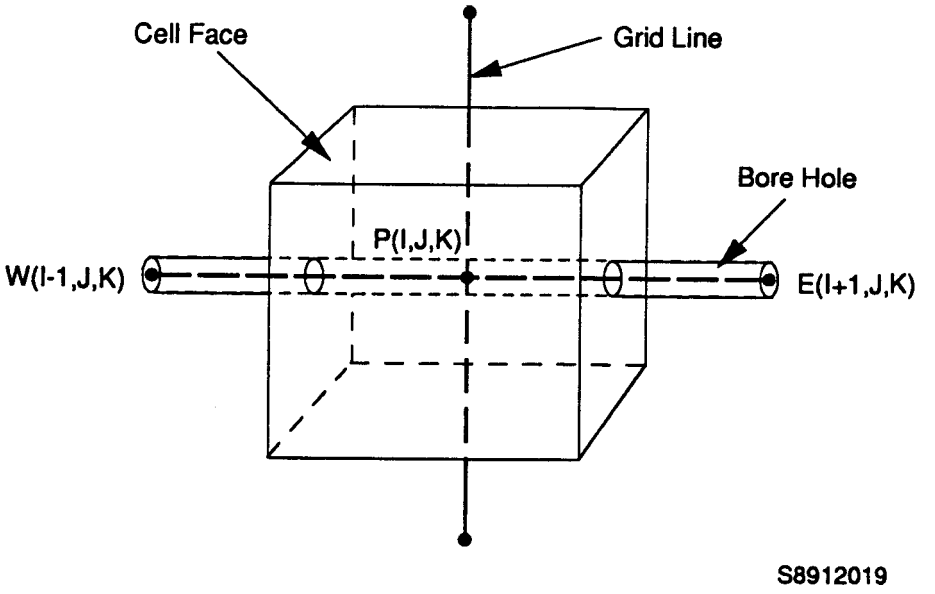

Figure 4-8. Inclusion of Borehole in x-Direction.

In theory, there is no limit on the number of fractures, dikes, and boreholes that can be included in the model. However, there are practical limitations, depending on available computer storage. One fracture, dike, or borehole may be distinguished from another by its alignment, geometric properties, or groundwater flow and contaminant transport properties, and each such feature may contain up to three zones with different properties. This capability is provided mainly in recognition of the fact that during construction of subsurface openings, the rock or soil around that opening is disturbed, thus creating zones of differing hydrologic properties.

This formulation of fluid flow and contaminant transport through fractures does not provide for accurate solution of the governing equations for the part of the domain that is in proximity to such features. If detailed information on flow and transport adjacent to these features is important, they should be represented as fully three-dimensional elements. If this is done, the grids would have to be very fine, thereby increasing computational costs. For most problems, interest centers on estimating integrated quantities, such as the fluxes of fluid, heat, and mass, rather than the distribution of pressures, temperatures, and concentrations on a fine scale. For these problems, the use of planar and linear elements provides reasonable results.

4.3 ALGEBRAIC ANALOGS OF BOUNDARY CONDITIONS

The general form of the boundary condition, as discussed in Section 3.7.5, is

$$- a \, \partial F/\partial N = b(F - F_0) + c, \qquad (4.3\text{-}1)$$

where N represents a direction normal to a boundary. Suitable choices for a, b, c, and F_0 lead to Dirichlet, Neumann, and mixed boundary conditions

(see Section 3.7.5). The algebraic equations for nodes located next to boundaries are modified to account for Equation 4.3-1. As an example, consider the node W, to the west of node P in Figure 4-7, to be a boundary node. To incorporate Equation 4.3-1 into the algebraic analog for node P, it is written as

$$- a\,(F_P - F_W) \,/\, \delta x_W = b(F_W - F_O) + c, \qquad (4.3\text{-}2)$$

where the value of Fp is taken at the advanced time, $t+\delta t$ (or at time step n+1). Equation 4.3-2 is now solved for F_W to obtain

$$F_W = a\,F_P + [\delta x_W\,(c - bF_O)\,] \,/\, [a - b\delta x_W]. \qquad (4.3\text{-}3)$$

Finally, Equation 4.3-3 is substituted into the algebraic equation Equation 4.3-2 for node P, which eliminates F_W from the latter equation.

Thus, when the coefficient matrix is formed, the boundary conditions are implicitly included in it. Once the equations are solved (i.e., the value of Fp is obtained), Equation 4.3-3 is used again (in case of Neumann and mixed boundary conditions) to obtain the new value of F at the boundary.

4.4 SOLUTION OF ALGEBRAIC EQUATIONS

4.4.1 Explicit Solution Method

For explicit solution of Equation 4.1-43, the superscript m is replaced by n; i.e., all of the F^m appearing on the right side of Equation 4.1-43 are assumed to be those at time t. Equation 4.1-43 then can be rearranged as

$$F_P = (1/A_P)\; a_P\, \forall p\, F_P^n + \sum_M A_M (F_M^m - F_P^m) + \sum_M (-1)^k\, C_M'\, F_P^m + S_P^m\, \forall p\, \delta t. \qquad (4.4\text{-}1)$$

Because all quantities on the right side of Equation 4.4-1 are known from initial conditions at time t, the Fp^{n+1} is easily evaluated by a simple substitution. The substitution is performed in a simple point-by-point manner. Three alternatives are available for the order of this substitution. In the first, the substitution starts along the x-direction (I=1 to IMAX), then along the y-direction (J=1 to JMAX), and finally along the z-direction (K=1 to KMAX). This is called an x-y-z sweep. For the second alternative, the substitution is performed in the order of the y, z, and x directions; whereas, in the third, it is performed in the order of the z, x, and y directions. These last two alternatives are called the z-x and x-y sweeps.

4.4.2 Implicit Solution Method

For implicit solution, the superscript, m, is replaced by n+1. Equation 4.1-43 then can be rearranged as

$$\left(A_P + \sum_M A_M + (-1)^k C'_M\right) F_P^{n+1} = \sum_M A_M F_M^{n+1} + S_P^n, \qquad (4.4\text{-}2a)$$

where

$$S_P^n = a_P V_P F_P^n + S_P^n V_P \delta t. \qquad (4.4\text{-}2b)$$

There are no more than seven unknowns (at node P and its six nearest neighbors) in Equation 4.4-2a. The number of unknowns is exactly seven for those nodes that have no boundary node as their neighbor. As explained in Section 4.3, values of F are eliminated for equations of those nodes that are located next to domain boundaries. Thus, for these nodes, the number of unknowns are fewer than seven. Writing the set of equations for all of the nodes results in a heptadiagonal matrix. This coefficient matrix is of banded form and is very sparse. The actual band width depends on how the nodes are numbered. In PORFLO-3, nodes are numbered in the order of increasing I, then J, and then K index. In this numbering system, the band width is 2 * (IMAX-2) * (JMAX-2).

To visualize the concept of sparsity of the coefficient matrix, consider a grid with dimensions of 10x12x15. The total number of nodes in this grid is 2,400. The number of internal nodes is 1,040. Thus, the coefficient matrix has 1,040 * 1,040 = 1,081,600 elements, of which fewer than 1,040 * 7 = 7,280 are nonzero.

Two direct and two iterative methods are available in PORFLO-3. The direct solution methods are accurate, but have the disadvantage of having elements within the band width that become nonzero during elimination procedures and thus require large amounts of storage. Therefore, these methods can be used only for relatively small grid sizes. The iterative methods, on the other hand, can be implemented using a limited storage space and, hence, are to be preferred for large grids. A brief description of these methods is provided in the following section.

4.4.2.1 Cholesky Decomposition Method. The Cholesky decomposition method is a direct solution method that is applicable to symmetric matrices. The governing equation for pressure is always symmetric. The governing equations for temperature and concentration are symmetric only if the convection terms are neglected; otherwise, they are asymmetric. In a matrix form, the set of algebraic equations may be written as

$$[A]\{F\} = \{R\}, \qquad (4.4\text{-}3)$$

where [A] is the symmetric coefficient matrix for elements A_{ij}, {F} is the vectors of unknowns, and {R} is the right side (or forcing) vector. [A] is of size NxN, where N is the number of internal nodes. Because [A] is symmetric, only half of the band width need be stored. In the Cholesky decomposition, [A] is decomposed into the product

$$[A] = [L]\,[L^T], \qquad (4.4\text{-}4)$$

where [L] is a lower triangular matrix for elements L_{ij}, and $[L^T]$ is the transposition of [L]. The general formulas for obtaining L_{ij} are (Jennings 1977)

$$L_{ij} = \left(A_{ij} - \sum_{k=1}^{i-1} L_{ik}\right)^{\frac{1}{2}}, \quad j > i, \tag{4.4-5a}$$

and

$$L_{ij} = \left(- \sum_{k=1}^{j-1} L_{ik}\, L_{jk}\right) / L_{jj}, \quad j < i. \tag{4.4-5b}$$

Having thus decomposed the coefficient matrix [A], solution of the system of equations [A] {F} = {R} proceeds in two stages. First, {G} = $[L^T]$ {F} is defined, whereupon the lower triangular system,

$$[L]\ \{G\} = \{R\}, \tag{4.4-6a}$$

may be solved for the vector {G} by forward substitution. Then, the solution for {F} is obtained from the upper triangular system,

$$[L^T]\ \{F\} = \{G\}, \tag{4.4-6b}$$

by back substitution.

4.4.2.2 Gaussian Elimination Method. Gaussian elimination, taking into consideration the special structure of the coefficient matrix, but without any pivoting, is used in PORFLO-3. Pivoting is not used because the coefficient matrix is expected to stay diagonally dominant throughout the elimination process.

With respect to Equation 4.4-3, the $(k+1)^{th}$ elimination step is as follows:

$$A_{ik}(k+1) = 0, \quad k < i \leq N, \tag{4.4-7a}$$

$$A_{ij}(k+1) = A_{ij}(k) - [A_{ik}(k)\, A_{kj}(k)] / A_{kk}(k), \quad k < i,j \leq N, \tag{4.4-7b}$$

and

$$R_i(k+1) = R_i(k) - [A_{ik}(k)\, R_k(k)] / A_{kk}(k), \quad k < i \leq N. \tag{4.4-7c}$$

After the reduction phase has been completed, the solution can be written into {R} beginning with the last row. This back substitution is described by the following equation:

$$F_{ij} = \left[R_i - \sum_{k=i+1}^{N} A_{ik}\, F_{kj}\right] / A_{ii}. \tag{4.4-8}$$

4.4.2.3 Alternating-Direction-Implicit Method. The Alternating-Direction-Implicit method completes the solution for one time step in three substeps. In the first substep, Equation 4.3-2 is replaced with

$$\left(A_P + \sum_M A_M + (-1)^k C'_M\right) F^*_P = A_E F^*_E + A_W F^*_W + S^* + S_P, \quad (4.4\text{-}9a)$$

where

$$S^* = A_S F^n_S + A_N F^n_N + A_D F^n_D + A_U F^n_U. \quad (4.4\text{-}9b)$$

Equation 4.4-9a generates a tridiagonal (no more than three unknowns per node) matrix that is easily solved using the Thomas algorithm to yield values of F^*. For the next substep, another approximation, F^{**}, is obtained from

$$\left(A_P + \sum_M A_M + (-1)^k C_M\right) F^{**}_P = A_S F^{**}_S + A_N F^{**}_N + S^* + S^n_P, \quad (4.4\text{-}10a)$$

where

$$S^* = A_W F^* + A_E F^* + A_D F^* + A_U F^*. \quad (4.4\text{-}10b)$$

Finally, the solution for δt is completed by a third approximation, F^{***}_P, which is obtained from

$$\left(A_P + \sum_M A_M + (-1)^k C_M\right) F^{***}_P = A_D F^{***}_D + A_U F^{***}_U + S^{**} + S^n_P, \quad (4.4\text{-}11a)$$

where

$$S^{**} = A_W F^{**}_W + A_E F^{**}_E + A_S F^{**}_S + A_N F^{**}_N. \quad (4.4\text{-}11b)$$

In many instances, F^{***}_P provides an acceptable approximation to F^{n+1}_P; however, PORFLO-3 provides for iterative solution of Equations 4.4-9a,b through 4.4-11a,b, for a prespecified number of cycles at each time step.

The procedure above describes the solution process that first proceeds in the x-direction (Equation 4.4-9a), then in the y-direction (Equation 4.4-10a), and finally in the z-direction (Equation 4.4-11a). In a manner similar to that for the explicit solution method, PORFLO-3 also provides for the sweeps to be conducted in the y-z-x and z-x-y directions.

4.4.2.4 Reduced-System Conjugate-Gradient Method. The Reduced-System Conjugate-Gradient method provides an accelerated iterative solution that is well suited to sparse matrices. In PORFLO-3, the Reduced-System Conjugate-Gradient algorithm developed by Kincaid et al. (1982) is used. Application of this method requires that the algebraic equations be reordered into a "red-black" system (Hageman and Young 1981). In this ordering, components of {F} are considered to be either "red" or "black." A red-black ordering rearranges the vector {F} such that every black unknown follows all of the red unknowns. This ordering leads to a 2x2 red-black partitioning of [A]; i.e.,

$$[A] = \begin{vmatrix} [A_{D1}] & [A_B] \\ [A_R] & [A_{D2}] \end{vmatrix}, \qquad (4.4\text{-}12)$$

where $[A_{D1}]$ and $[A_{D2}]$ are diagonal submatrices, and $[A_B]$ and $[A_R]$ are, respectively, the black and red submatrices.

The conjugate-gradient algorithm follows the following steps (Reid 1981). The residual at iteration k, r(k), is

$$\{r(k)\} = \{R\} - [A]\{F(k-1)\}, \qquad (4.4\text{-}13)$$

where F(0) is the initial approximation of the solution. The following steps are then followed:

$$q(k) = \langle\{r(k)\},[A]\{r(k)\}\rangle \,/\, \langle\{r(k)\},\{r(k)\}\rangle - e(k-1), \qquad (4.4\text{-}14a)$$

$$\{r(k+1)\} = \{r(k)\} + (1/q(k)) \left[-[A]\{r(k)\} + e(k-1) \left(\{r(k)\}-\{r(k-1)\}\right)\right], \qquad (4.4\text{-}14b)$$

$$\{F(k+1)\} = \{F(k)\} + (1/q(k)) \left[\{r(k)\} + e(k-1) \left(\{F(k) - \{F(k-1)\}\right)\right], \qquad (4.4\text{-}14c)$$

and

$$e(k) = q(k)[\langle r\{k+1\},\{r(k+1)\}\rangle \,/\, \langle\{r(k)\},\{r(k)\}\rangle]. \qquad (4.4\text{-}14d)$$

In Equation 4.4-14a-d, $\langle\{r\},\{s\}\rangle$ denotes the inner product of the two vectors, {r} and {s}. The iterations are performed until the solution satisfies a tolerance limit on the residual, {r}.

4.5 TREATMENT OF NONLINEARITIES

The governing equations for temperature and concentration (Equations 3.2-14 and 3.3-14) have slight nonlinearities. These nonlinearities stem from the fact that the convective velocities, U, V, and W, can be functions of temperature and concentration. With suitably selected time steps, these minor nonlinearities are of no consequence in solution of the equations. In general, it is assumed that the values of the quantities that depend on the dependent variable are available from the calculation at the previous time step. That is, these quantities lag the solution by one time step.

The governing equation for pressure (Equation 3.1-23), however, can be highly nonlinear for conditions of partial saturation. This is apparent from the soil-moisture relations discussed in Section 3.7.3. For most soils and rocks, the degree of nonlinearity increases as the saturation decreases. To deal with these nonlinearities, an iterative method is followed in PORFLO-3.

Three iterative methods for nonlinear equations are discussed in Huyakorn and Pinder (1983): (1) Picard, (2) Newton-Raphson, and (3) chord

slope. Of these, the Picard method is the simplest, requires no additional storage, and is currently implemented in PORFLO-3. In a later, updated version of PORFLO-3, the Newton-Raphson method and its variation, the chord slope methods, may also be implemented.

Using the Picard method, solution is begun with an initial "guess," which is usually the initial conditions specified by the user. Values of parameters that are functions of the dependent variable are calculated using this guess and substituted into Equation 4.1-43. Solution of Equation 4.1-43 provides a new estimate of the solution, and the process is repeated until specified convergence criteria are satisfied.

The following two options for determining convergence are provided by PORFLO-3:

$$\max_{i=1,N} \left| \left(1 - F_i(k+1)/F_i(k)\right) \right| \leq \epsilon, \tag{4.5-1}$$

and

$$(1/N)\left[\sum_{i=1}^{N}\left\{1 - [F_i(k+1)/F_i(k)]\right\}^2\right]^{\frac{1}{2}} \leq \epsilon, \tag{4.5-2}$$

where N is the total number of internal nodes, k is the iteration number, and ϵ is the specified convergence limit.

4.6 CHOICE OF SPATIAL GRID AND TIME STEPS

The design of the spatial grid and choice of time steps for a given problem may depend on several, competing objectives. A need for detailed and accurate solutions suggests the use of a fine-mesh spatial grid and small time steps, but limitations on computer resources (memory and execution time) restrict their use. In practice, considerations of computational cost, accuracy and stability of numerical solution, output needs with respect to locations and times, and accommodation of special physical features (boundaries, heterogeneities, and sources) influence design of the spatial grid and choice of time steps. Some of the factors that need to be considered in choosing grid spacing and time steps are discussed in the following section.

4.6.1 Design of Spatial Grid

4.6.1.1 Scale of Heterogeneity. The spatial variation in hydraulic, thermal, and mass transport properties should be adequately represented by the grid. The material properties are specified at grid nodes and are assumed to remain constant within a cell. If these properties change in a discontinuous manner, as commonly occurs in layered geologic media, spatial grids should be designed such that a cell face coincides with the boundary between two layers with differing characteristics. For problems with continuously varying properties, the cell size should be smaller in regions where the variation in properties is relatively rapid and larger where the variation occurs more

slowly. All other factors being equal, a uniformly accurate solution may be expected if the properties of interest vary uniformly across the cells of interest.

To design the grid, it is helpful to sketch the domain and all of the zones in which the properties of concern have different values. Then, cell faces should be located wherever an abrupt change in these properties is anticipated. Because the grid nodes are located midway between two cell faces, the two nodes on either side of the cell face will automatically be fixed in space, in accordance with the cell face locations.

4.6.1.2 Scale of Resolution. For a variety of reasons, in specific parts of the domain, solutions may be needed at a finer scale than in other parts. For example, interest may be focused on those areas where temperatures or chemical concentrations are high. In such areas, smaller cells should be used.

4.6.1.3 Scale of Geologic Features. Geologic features, such as fractures, faults, or clastic dikes, and man-made features, such as boreholes, wells, and tunnels, are commonly distinguishable from the geologic continua by distinctive contrasts in their physical properties and scales. To accurately represent these features, cell sizes that are comparable to the sizes of these features (i.e., to the sizes of their apertures, thicknesses, and diameters) should be used.

However, if the solution in close proximity to these features is not of interest, they alternately may be represented as two-dimensional planar elements and one-dimensional line elements. Fractures and clastic dikes can be considered to be planar features because the dimension orthogonal to the plane defined by their dip and strike is considerably smaller than their dimension in that plane. Consequently, fluid flow, heat transfer, and mass transport can be assumed to occur in only two dimensions in these features. Similarly, only one dimension need be considered for boreholes, wells, and tunnels. If these features are represented using reduced dimensionality, the choice of cell sizes is not affected by them.

4.6.1.4 Sources and Sinks. Hydraulic head, temperature, and chemical concentrations usually can be expected to change rapidly close to sources and/or sinks of fluid, heat, and mass. Unacceptable errors may occur in the solution if large cells are used in such areas. As a general principle, finer mesh grids should be used in areas where the values of the state variables are expected to change rapidly.

4.6.1.5 Boundary Conditions. Some boundaries are natural geologic features. For instance, a river may form a boundary at which it is appropriate to specify hydraulic heads. Cell sizes should be comparatively small in close proximity to these boundaries. Other boundaries do not represent natural geologic features and usually are located at large distances (in theory, at infinite distance) from the area of interest. Near these boundaries, coarse-mesh grids can be used. In problems with boundaries at infinity, it is advisable to discern whether the boundaries are located at distances sufficiently far that they do not affect the solution.

4.6.1.6 Memory Requirements. The amount of computer memory required to solve a problem is directly proportional to the number of computational cells. Consequently, an upper limit to the number of computational cells is imposed by the available capacity of the computer memory. An estimation of appropriate cell size, based on the considerations discussed above, may require subsequent adjustment to remain within this limit.

4.6.1.7 Computation Time. The time required to solve a problem is a non-linear function of the number of grid cells. The time of computation increases in a ratio that varies from the square to the cube of the number of cells. In some cases, the maximum allowable computation time may restrict the maximum number of computational cells.

4.6.2 Choice of Time Steps

The size of time steps is determined by the time scales characteristic of the propagation of pressure, diffusion, and convective transients. These time scales depend on the cell sizes discussed in Section 4.6.1 and the material properties discussed in the following sections.

The choice of time steps also is influenced by considerations of numerical stability. In general, a stable numerical scheme controls the growth of numerical error as the solution advances with time. Two types of instabilities may be encountered: (1) weak instability in which the solution oscillates about a mean value and (2) strong instability in which divergence from the true solution increases monotonically. Both types of instabilities can be removed by shortening the time steps. However, for strong instability, alternative solution methods (see Section 4.4) may be more economical.

4.6.2.1 Time Scale of Pressure Transient. Let δL represent the length of one edge of a computational cell; δL can be equal to δx, δy, or δz, depending on the coordinate direction of interest. Similarly, let K_L represent the hydraulic conductivity in the L direction of the cell under consideration. (L could be in the x, y, or z direction.) The characteristic time scale (δtp_L) for the propagation of transient pressure (or hydraulic head) effects in the L direction for that cell is given by

$$\delta tp_L = S_S \, \delta x^2 / K_x. \qquad (4.6\text{-}1)$$

Similar equations can be written for all cells. The smallest of these characteristic time-scale values for all cells in the grid represents the time scale for pressure transients (δtp). The term δtp is an approximation of the time required to propagate a pressure change across a cell. If the computational time step, δt, is much larger than δtp, it is possible that the variation of pressure with time will be missed across some of the cells in the grid. Therefore, for problems in which prediction of time-dependent pressures (or hydraulic heads) is important, δtp can be used as a guide in selecting appropriate time steps. For the Point Successive Over Relaxation method of solution (see Section 4.4.1), stability considerations require that δt be less than δtp. For other methods of solution, there is no theoretical limit on δt for stability, but for physically accurate solutions, δt should be kept less than ten times δtp.

Pressure transients may be thought of as consisting of waves of different frequencies. As the high-frequency components move across the computational grid, the severity of pressure transients decreases. Therefore, it is possible to gradually increase the size of the time step as the solution advances with time.

4.6.2.2 Time Scale of Diffusion. A time scale of diffusion is defined in a similar manner to the time scale of pressure transients that was discussed in Section 4.6.2.1:

$$\delta t_D = \delta L^2/(2D_L), \qquad (4.6\text{-}2)$$

where D_L is the diffusion coefficient in the L direction (which can be in the x, y, or z direction). The term D_L is the sum of the molecular diffusion coefficient and the coefficient of hydrodynamic dispersion (see Section 3.7.4). For reasons analogous to those discussed above, the smallest value of δt_D in the grid is selected. For problems in which diffusion and dispersion are major considerations, the choice of size of the time step should be guided by the value of δt_D. For the Point Successive Over Relaxation method to be stable, the computational time step size, δt, should be less than δt_D. For other methods, δt should be less than ten times δt_D.

4.6.2.3 Time Scale of Convection. The time scale of convection is based on the flow velocity of fluid and is defined as

$$\delta t_C = \delta L/U_L, \qquad (4.6\text{-}3)$$

where U_L is the fluid velocity in the L direction (in which L can be in the x, y, or z direction). The constraint on size of the computational time step, δt, based on Equation 4.6-3, is often stated in terms of the Courant number, Co, which is defined as

$$Co = \delta t/\delta t_C = (U_L\ \delta t)/D_L. \qquad (4.6\text{-}4)$$

For the Point Successive Over Relaxation method to remain stable, Co must not exceed unity. For other methods, δt must not exceed ten times δt_C.

4.6.2.4 Other Time Scales. The time scales defined above are the most common ones. However, in certain problems, other time scales may apply. These other time scales occur whenever time-dependent phenomena are included in the problem. For example, time-varying sources and sinks and time-dependent boundary conditions inherently would have time scales associated with them. The general rule in such cases is that the size of the computational time step, δt, be kept less than any other time scale of a problem. The basis for this rule is that the effect of the variation of time on any phenomena with a time scale less than δt will not manifest itself in the solution.

5.0 APPLICATION EXAMPLES

Two example simulations using PORFLO-3 are presented in this chapter. Both examples represent realistic applications to complex problems of groundwater flow and contaminant transport. Specifically, the two simulations described in this chapter are (1) dynamics of a three-dimensional plume from a distributed source and (2) three-dimensional flow in the presence of linear and planar features.

5.1 EXAMPLE ONE: THREE-DIMENSIONAL PLUME FROM A DISTRIBUTED SOURCE

5.1.1 Description of Problem

Chemical processing of spent nuclear fuel at the Hanford Site, located in south-central Washington State, has resulted in the accumulation of large inventories of chemical, nuclear, and mixed wastes. From 1943 to 1964, a large part of this waste was stored underground in 149 single-shell waste storage tanks. These tanks are constructed of concrete and lined with a single layer of carbon-steel. The tanks are generally configured into "tank farms," which consist of groups of 6 to 18 buried tanks interconnected by pipes. These tanks range in size from 6 to 23 m (15 to 75 ft) in diameter and 6 to 15 m (15 to 50 ft) high, are buried 40 to 70 m above the water table, and are typically covered by several meters of overburden.

Approximately 450 m^3 (115,000 gal) of liquid containing radioactive and chemical wastes leaked from one of these waste tanks in June 1973 (AEC-RL 1973; ARHCO 1973; Gillette 1973). This tank (241-T-106) is 23 m (75 ft) in diameter and 8.5 m (28 ft) high, with a storage capacity of 2,000 m^3 (500,000 gal). The leaked fluid discharged into the unsaturated coarse-grained sediments of the Hanford formation, which underlie the base of the tank. The extent of the contaminant plume in the vadose zone was estimated through gamma energy spectrometry in dry wells drilled to monitor the leak (ARHCO 1973; Routson et al. 1979). Data on the configuration of the plume in 1973 provide an excellent opportunity to test the applicability of PORFLO-3 for studying flow and transport in the vadose zone.

5.1.2 Description of Site Hydrogeology and Conceptual Model

Geologic details of the 241-T tank farm have been described by Price and Fecht (1976) and Fecht and Price (1977), and a summary is provided in Figure 5-1. The water table is located within a thick sequence of sediments that are probably part of the middle member of the Pliocene age Ringold Formation. These coarse-grained sediments are overlain by about 14 m of fine-grained sediments that probably are part of the upper Ringold Formation and at least a portion of a unit of the Plio-Pleistocene age. These sediments consist of stratified, silty, fine to very fine-grained sand with intercalated, calcareous zones. At an elevation of about 173 m, or approximately 30 m below the surface, the sediments appear to be highly cemented. This cementation may represent caliche formation in a near-surface soil horizon during late Pliocene time.

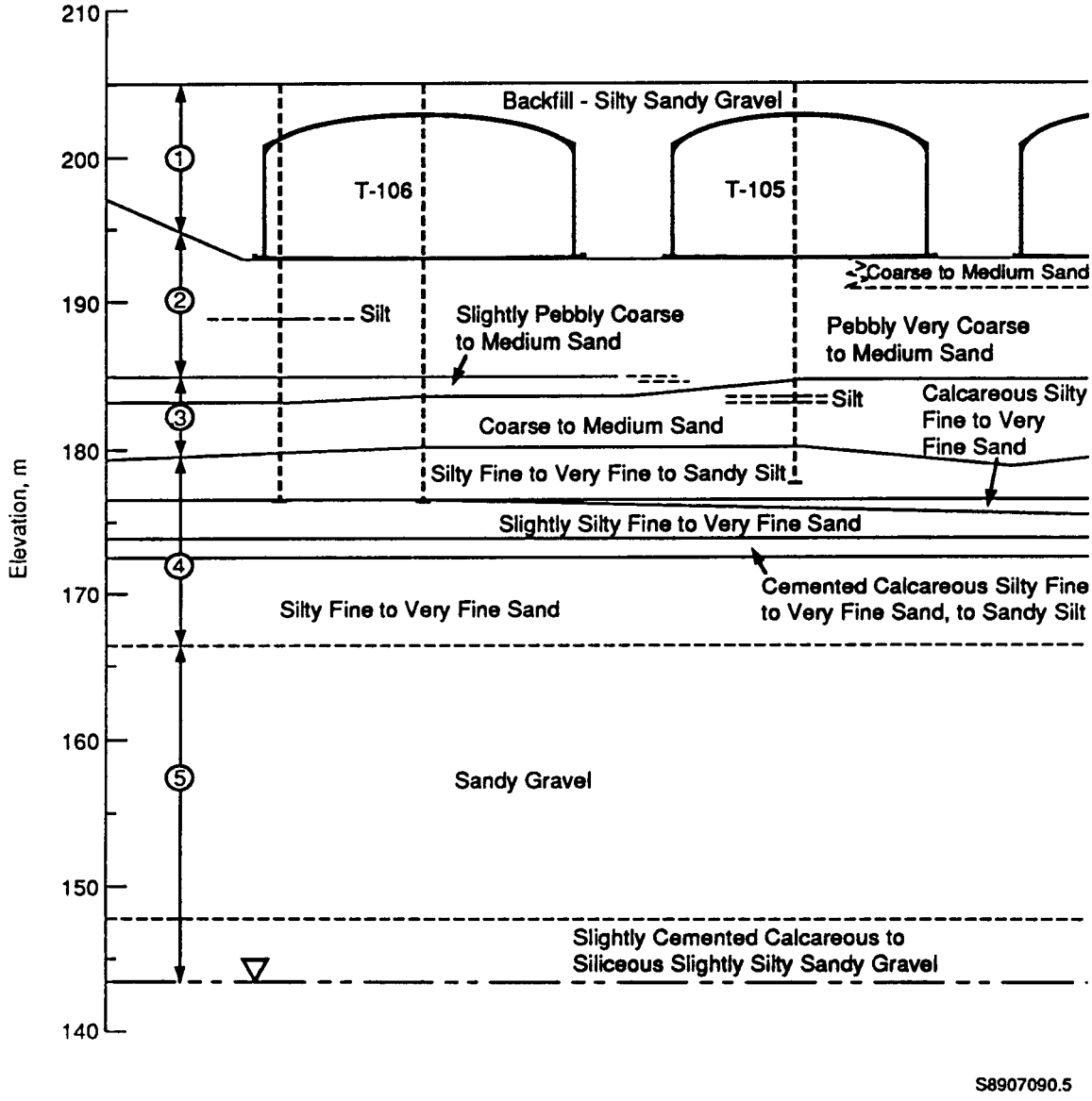

Figure 5-1. Stratigraphy of the T Tank Farm.

Overlying the fine-grained sediments are about 4 m of somewhat coarser grained material consisting of coarse- to medium-grained sand with some pebbles in the upper portion. This zone may contain sediments from both the upper Plio-Pleistocene unit and the lower portion of the Hanford Formation. Above this zone approximately 8 m of the pebbly, very coarse- to medium-grained sands of the Hanford Formation extend to the base of the single-shell tanks. A silty, sandy, gravelly backfill comprises the remaining 12 m of sediments to the surface. The upper 10 to 20 m of the Hanford Formation were locally excavated and backfilled during installation of single-shell tanks. The backfill was derived from the excavated material. In the remainder of this report, this zone is described as backfill to distinguish it from undisturbed Hanford Formation.

Based on the above description, five stratigraphic subdivisions (referred to as zones) were included in the conceptual model shown in Figure 5-2. The unconfined aquifer in the vicinity of the 241-T-106 tank is contained within the unconsolidated sediments of the middle, lower, and basal members to the Ringold Formation; the underlying Columbia River Basalt is assumed to form the base of this aquifer. Groundwater generally flows towards the Columbia River. Depths to water are commonly 60 to 80 m.

5.1.3 Hydrogeologic and Transport Parameters

Soil moisture-retention characteristics used in the simulation were based on qualitative comparison of soil textural and stratigraphic properties with catalogs of data that document these characteristics for certain Hanford Site soils. The absence of data specific to the site of the tank (241-T-106) introduces an undetermined amount of uncertainty into the modeling results.

The moisture-retention curves for the five soil horizons (or zones) are shown in Figures 5-3 through 5-6. The curves show that the soils exhibit a

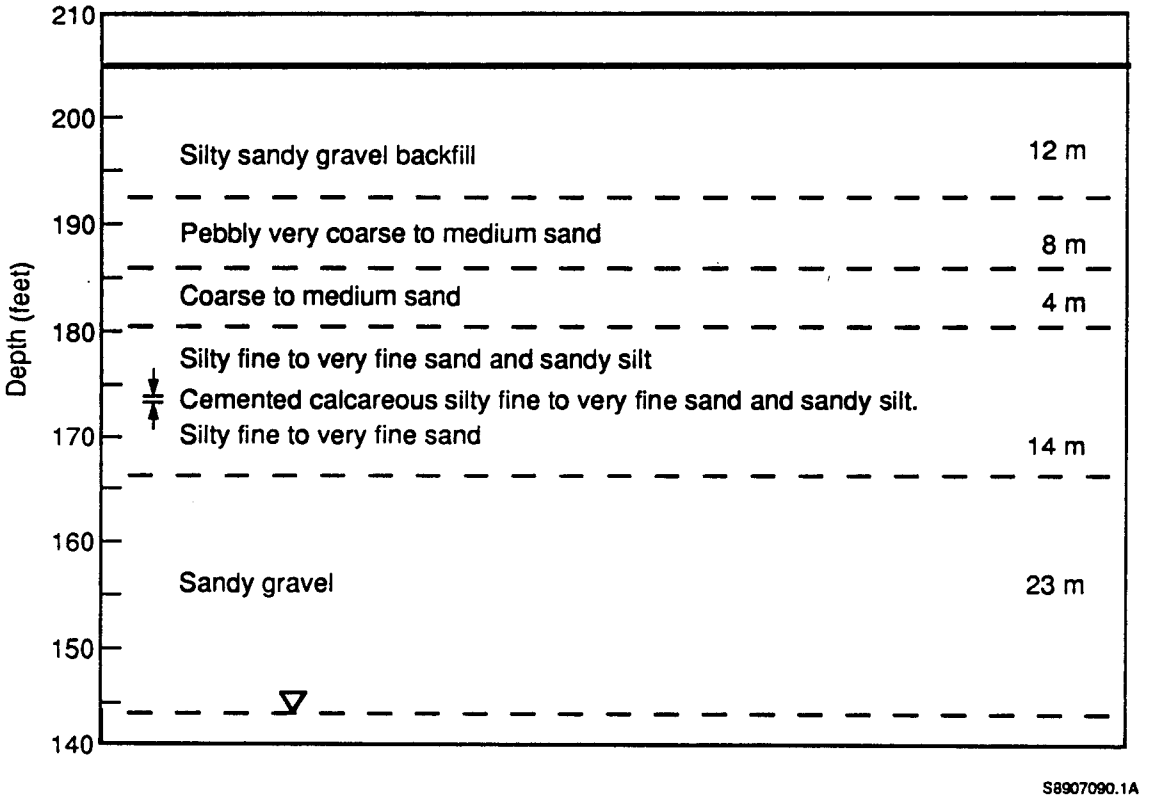

Figure 5-2. Textures and Thicknesses of the Five Major Stratigraphic Zones at the T Tank Farm.

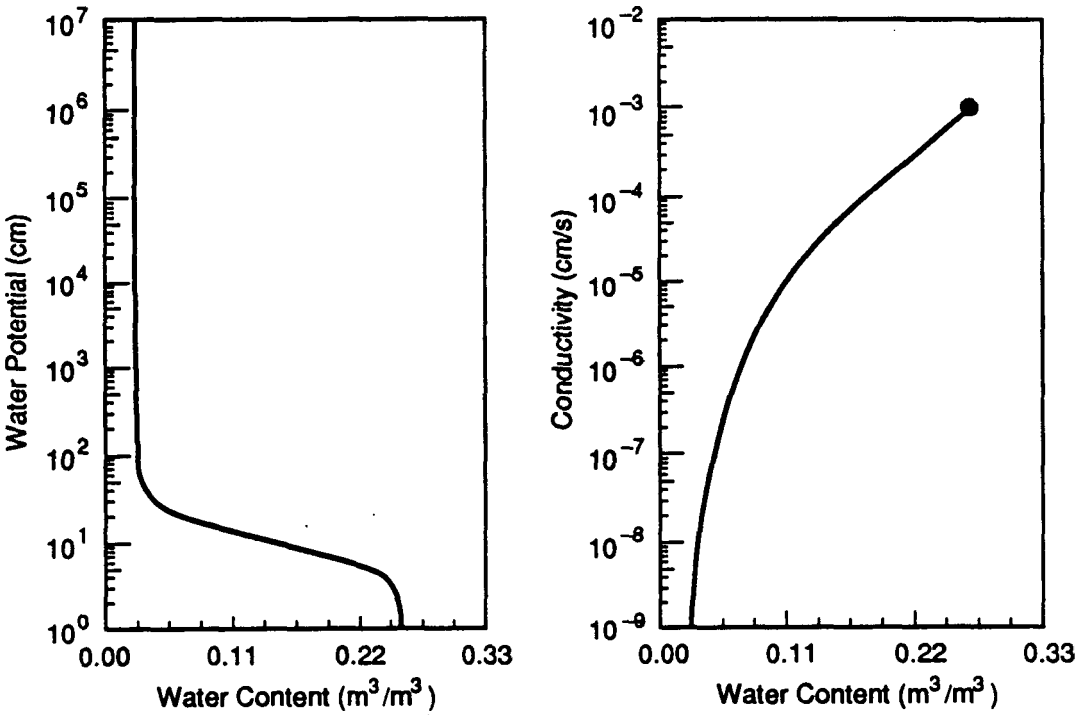

Figure 5-3. Moisture-Retention Curves for Soil Horizons One and Five at the T Tank Farm.

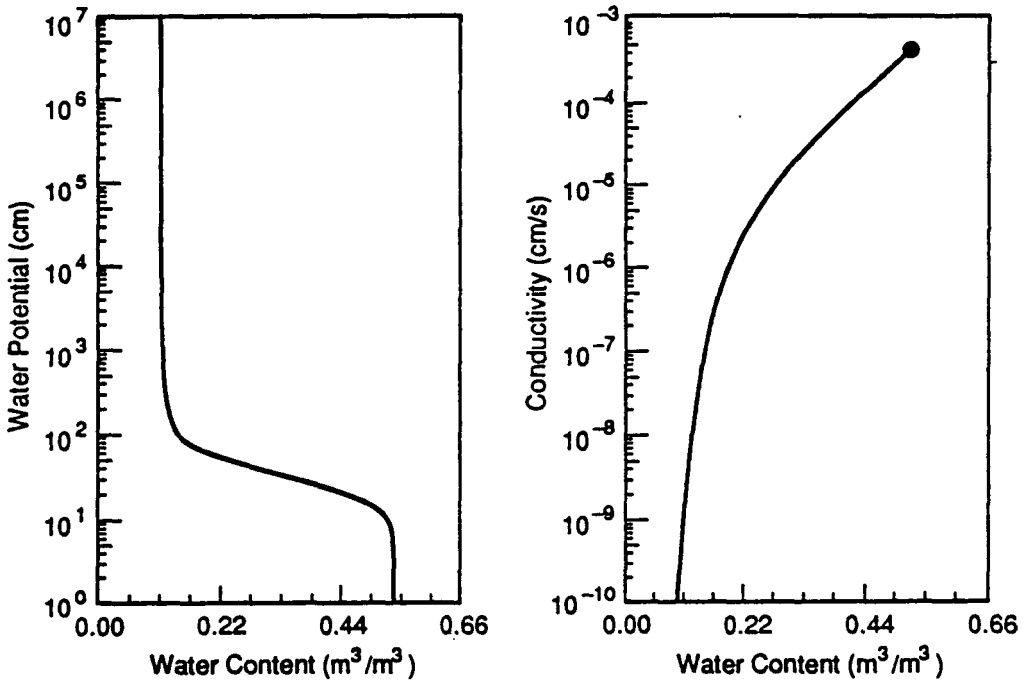

Figure 5-4. Moisture-Retention Curves for Soil Horizon Two at the T Tank Farm.

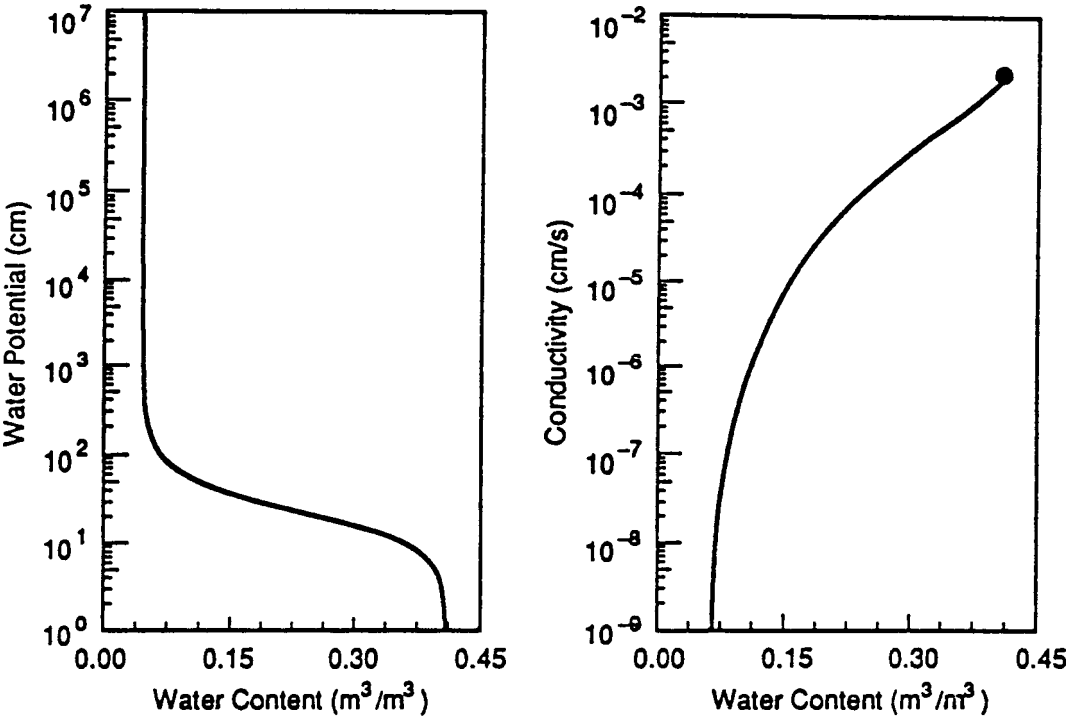

Figure 5-5. Moisture-Retention Curves for Soil Horizon Three at the T Tank Farm.

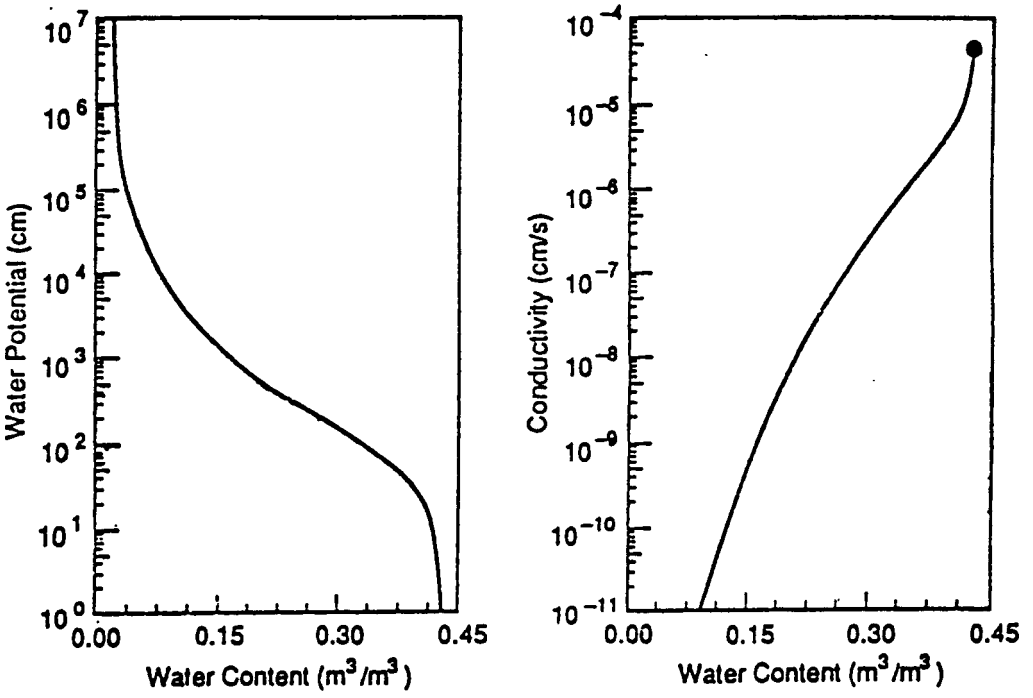

Figure 5-6. Moisture-Retention Curves for Soil Horizon Four at the T Tank Farm.

relatively wide range of properties. The corresponding unsaturated hydraulic conductivity curves also are shown in the figures. The tank itself was assumed to be impermeable except for the leaking area.

Contaminant transport coefficients were assumed for each of the five major soil horizons. For all five soil horizons, the molecular diffusion coefficient (D) was held constant at 1×10^{-5} m^2/day and longitudinal and transverse dispersivity at 1.0 m and 0.1 m, respectively. For those model simulations incorporating retardation, a distribution coefficient of 5×10^{-7} m^3/g (0.5 mL/g) was used for ^{106}Ru and 1×10^{-4} m^3/g (100.0 mL/g) for ^{137}Cs. These parameter values are generic in nature and are not based on actual measurements of the 241-T tank farm soils.

Estimates of natural recharge depend on soil type, vegetation, and climatic factors and vary widely for the Hanford Site (Gee 1987). A value of 5 cm/yr was used for the simulations reported here.

5.1.4 Source Terms

Routson et al. (1979) provide a detailed chronology of the 241-T-106 tank leak. Leakage began on or about April 20, 1973; the tank was filled to capacity by reprocessed wastes. Leakage stopped on June 10, 1973, when the pumpable liquid contents of the tank were removed. The total duration of the leak was approximately 52 days, during which 115,000 gal of supernatant fluid were lost from the tank.

The conceptual model source terms for radionuclides are based on their known inventories in the supernate. The total inventory of about 2.7×10^{11} μCi of ^{106}Ru results in a source term of 5.1×10^{9} μCi/day, during the 52 days that the leak occurred. The corresponding liquid flux is about 8.4 m^3/day and is assumed to have density and viscosity properties identical to water. The total inventory of ^{137}Cs was about 3.8×10^{10} μCi, resulting in a source term of about 7.4×10^{8} μCi/day for the 52-day duration of the leak.

The tank leak apparently occurred on the southeast side of the tank; the contaminant plume is centered around this portion of the tank. Figure 5-7 shows a plan view and vertical cross section of the plume measured in the summer of 1973, 100 days after the tank was pumped out and the leak stopped. The figure shows the concentrations of ^{106}Ru, ^{144}Ce, and ^{137}Cs. Ruthenium-106 is the most mobile of the three and traveled the farthest; ^{137}Cs is the least mobile and was contained within a small zone at the base of the tank. The configuration of the ^{106}Ru plume appears to be approximately circular, with a radius of about 15 to 20 m in plan view and a maximum depth of penetration of about 20 m. Figure 5-7 shows the horizontal and vertical distribution of ^{106}Ru for several isopleths. This figure reveals a relatively steep distribution front, both laterally and vertically.

5.1.5 Description of Numerical Mesh and Boundary Conditions

In the horizontal plane, the model domain extends about four or five tank diameters (one diameter = 22 m) beyond the tank. At this scale, each

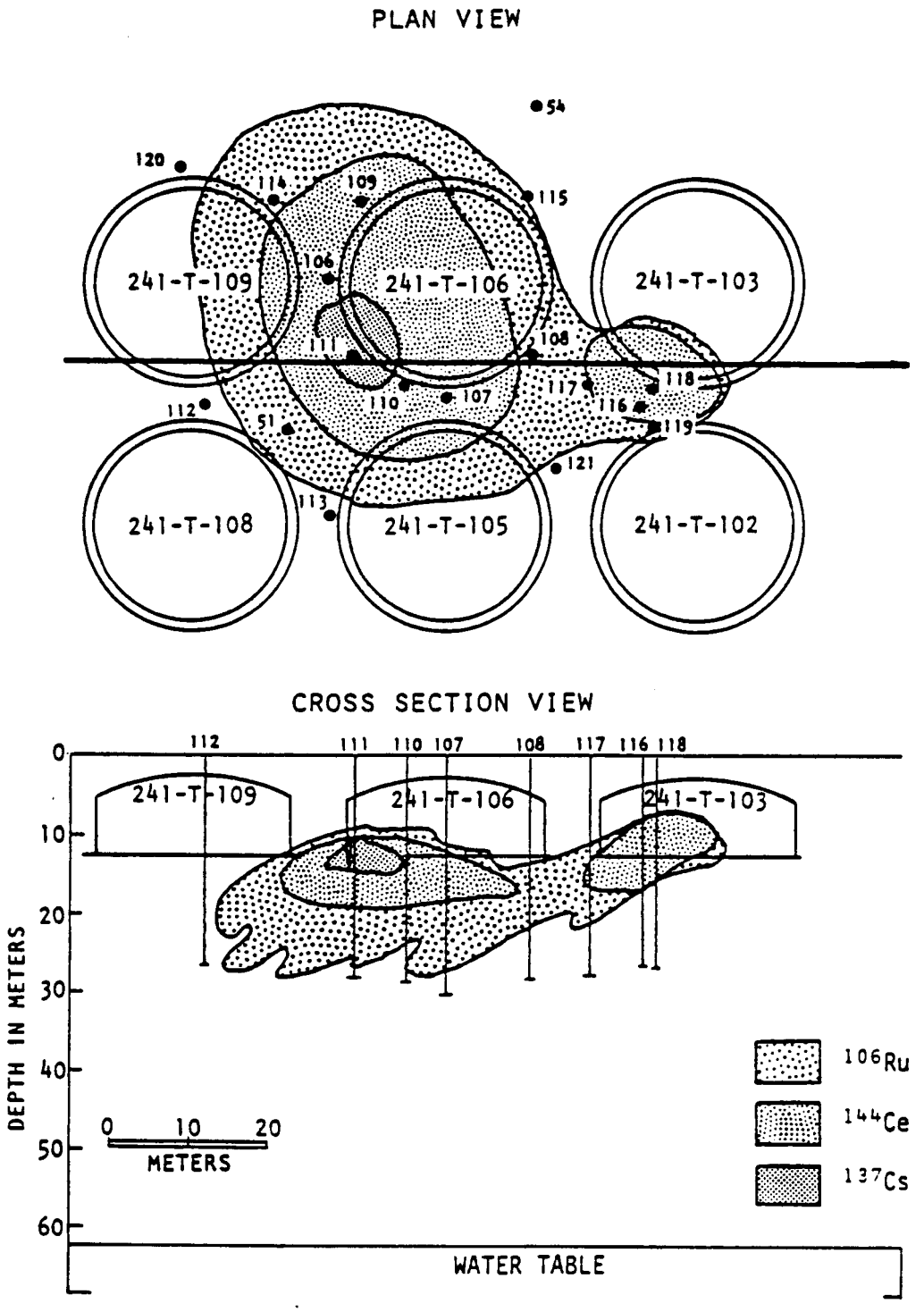

Figure 5-7. Vertical and Horizontal Cross-Sectional Views of the 1973 ^{137}Cs, ^{137}Ce, and ^{106}Ru 1-μCi/L Volumetric Isopleths (measured) (after Routson et al. 1979). Note: Numbers identify boreholes.

soil stratum within the domain was assumed to be of constant thickness (see Figure 5-2). No flow was allowed across the vertical boundaries of the domain. Thus, on the scale of the model domain (≈80 m), the flow was vertical. However, locally in the vicinity of the leak, flow was fully three dimensional. The water table formed the lower boundary for the model. The pressure at this boundary was assumed to remain fixed at the atmospheric value. A uniform infiltration of 0.05 m/yr was applied to the upper surface of the model. The tank itself was represented as an impervious block. This allowed the infiltrating water to be diverted around the tank. Thus, in a localized area around the perimeter of the tank, the volumetric flux may be significantly enhanced.

The three-dimensional model domain is a region of 3.7×10^5 m^3, having dimensions of 88 x 68 x 62 m. This domain has been discretized into a 24 X 15 X 33 Cartesian grid containing 11,880 cells. The discretization is shown in Figure 5-8. A variable grid spacing is used in all three dimensions. In the x and y directions, the finest discretization of 2 m is used in the vicinity of the tank; the discretization coarsens with distance towards the edge of the grid. In the vertical direction, the grid size varies from 0.5 m near the base of the T-106 tank to 8 m near the water table.

Initial conditions were specified for hydraulic head and radionuclide concentration throughout the model domain. To estimate the initial conditions, the soil moisture tension within the unsaturated sediments was assumed to be in equilibrium with a constant 0.05 m/yr infiltration rate. For conditions of unit hydraulic gradient (because of gravity), the hydraulic conductivity was equal to the infiltration rate from which the initial soil suction was then estimated. These initial soil moisture-tension values did not account for the possible additional water flux adjacent to the tank because of the diversion of water around its domed top.

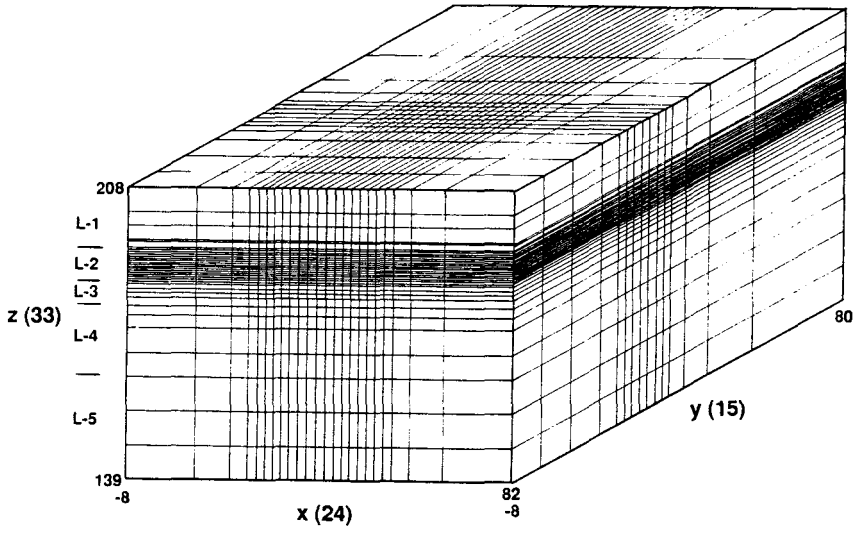

Figure 5-8. Discretized Grid for Three-Dimensional Calculations.

The starting time of the simulation was the instant just before the start of tank leak. The initial concentration of radionuclide was set equal to zero throughout the soil volume. Because the tank is impervious, the concentration inside the tank was immaterial.

5.1.6 Results

5.1.6.1 Moisture Movement. The PORFLO-3 program provides output for soil moisture in terms of saturation for each time step. The two major sources of moisture to the model were infiltration from precipitation and the fluid introduced by the tank leak. The leak itself is expected to produce a saturated slug, which would move predominantly downward with some lateral spread, thus increasing the relative saturation of the underlying sediments. Consequently, the major features of interest with respect to the moisture movement and redistribution are the infiltration around the tank and the movement of the leaked fluid volume.

The simulated redistribution of the leaked fluid is shown in Figures 5-9 through 5-13. Figure 5-9 shows moisture distribution at 150 days after the leak started. The sediments just below the tank have begun to drain. The zone of higher saturation resulting from the leaked tank fluid is about 15 m below the base of the tank in the top of soil zone 4. Zone 4 has a lower porosity than zone 3. It has a much lower saturated hydraulic conductivity and may be expected to inhibit spread of the fluid. These features lead to an increase in saturation near the top of the finer-grained sediments in zone 4 which is apparent from Figure 5-9.

At later times, shown in Figures 5-10 through 5-13, the moisture slug continues to drain and spread. Of special note is the high moisture zone formed next to the tank sides visible in Figures 5-11 through 5-13. Velocity vectors, showing the direction of water movement along the same cross section (Figure 5-14), reveal water moving laterally across the top of the tank, down along the sides, and perhaps refracting slightly as it enters the sediments below the tank. These results would seem to indicate that the assumed initial conditions based on a 0.05 m/yr recharge may not be correct close to the tank.

5.1.6.2 Ruthenium (^{106}Ru) Plume. All concentrations reported in this example are based on the bulk soil volume; i.e., volume, including solids and liquids. The results for ^{106}Ru migration calculations are shown in a vertical cross section in Figure 5-15 and in a horizontal cross section in Figure 5-16 for up to 150 days after the leak began. These figures show migration of the 1-μCi/L ^{106}Ru isopleth to a depth of about 40 m below the tank after 150 days from the beginning of the leak. This is about twice as far as was observed in the dry wells adjacent to the tank (see Figure 5-7) as reported by Routson et al. (1979). Although discrepancies in the measured plume may result from an absence of measurements under the tank and conversion of gamma counts to concentrations, for the purpose of this modeling exercise the 1973 measured plume data are assumed to be correct. The plume migration rate in the vertical direction, therefore, should be slower than obtained from this first model calculation. The horizontal cross section shown in Figure 5-16 is taken about 5 m below the base of the tank

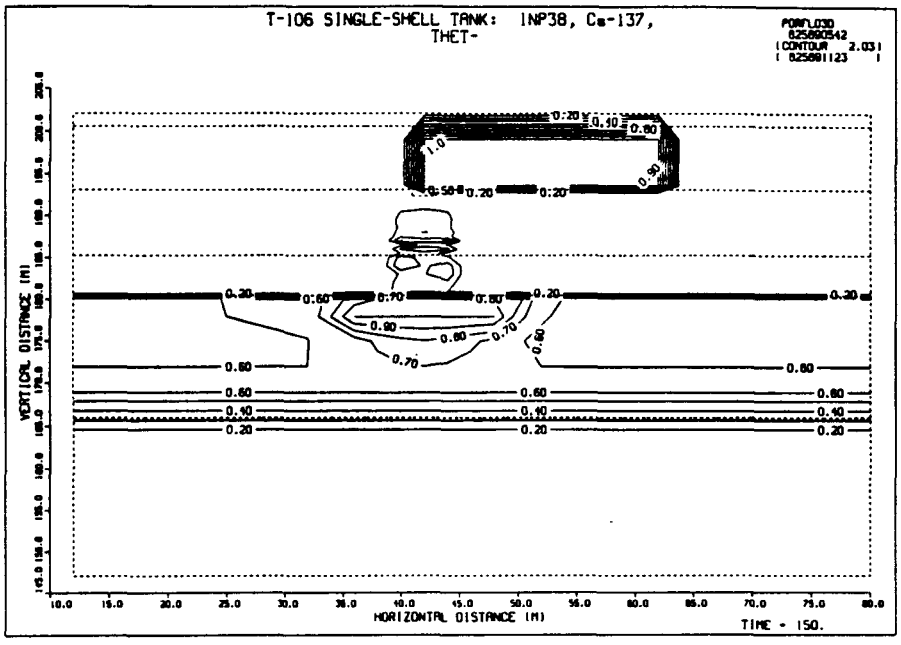

Figure 5-9. Calculated Relative Saturation 150 Days After Beginning of Leak (base case properties).

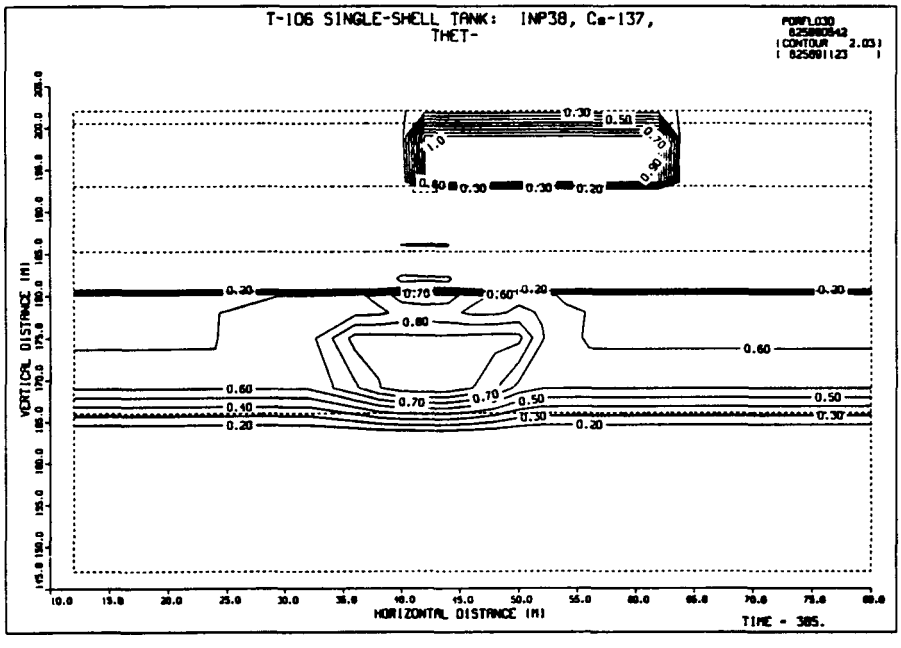

Figure 5-10. Calculated Relative Saturation 1 Year After Beginning of Leak (base case properties).

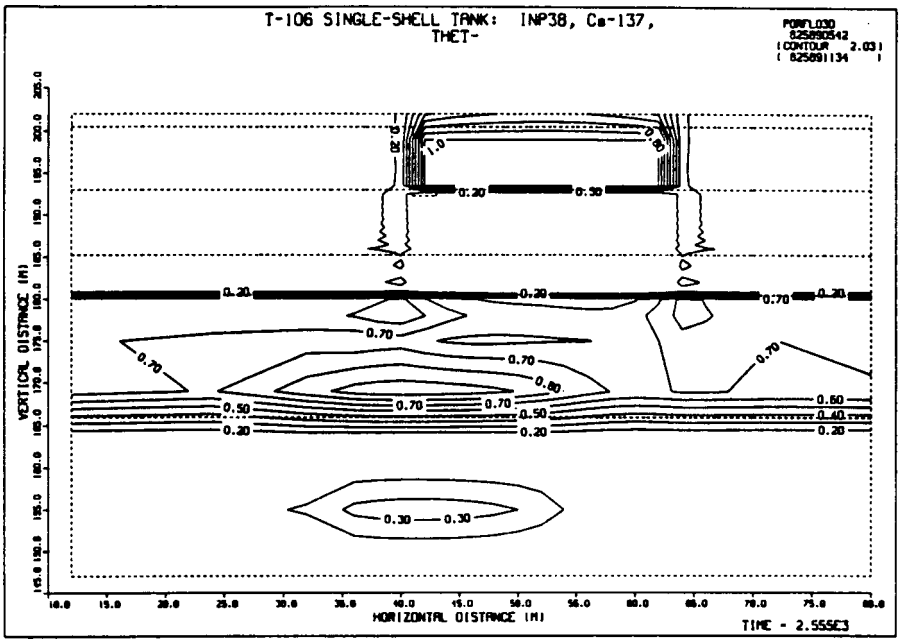

Figure 5-11. Calculated Relative Saturation 7 Years After Beginning of Leak (base case properties).

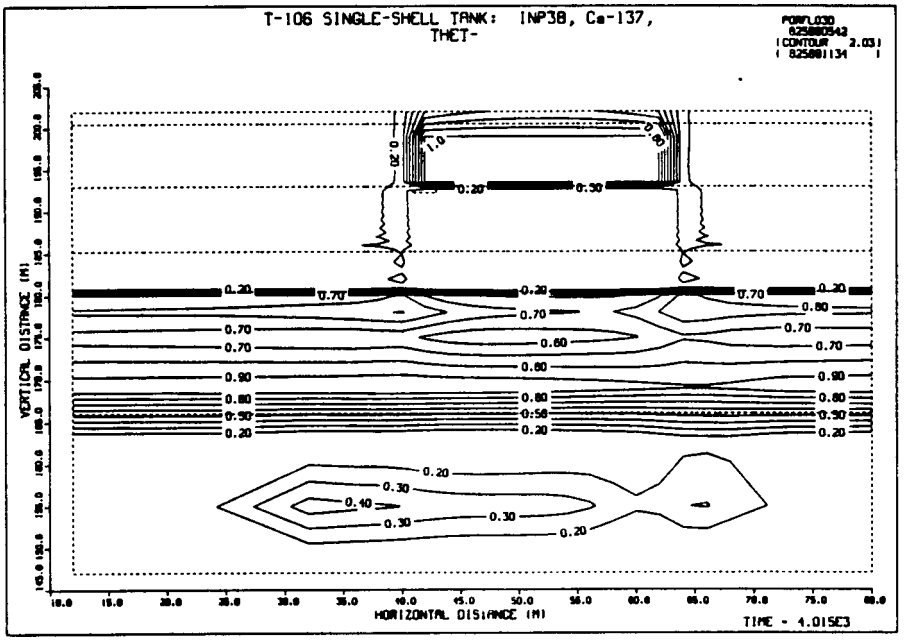

Figure 5-12. Calculated Relative Saturation 11 Years After Beginning of Leak (base case properties).

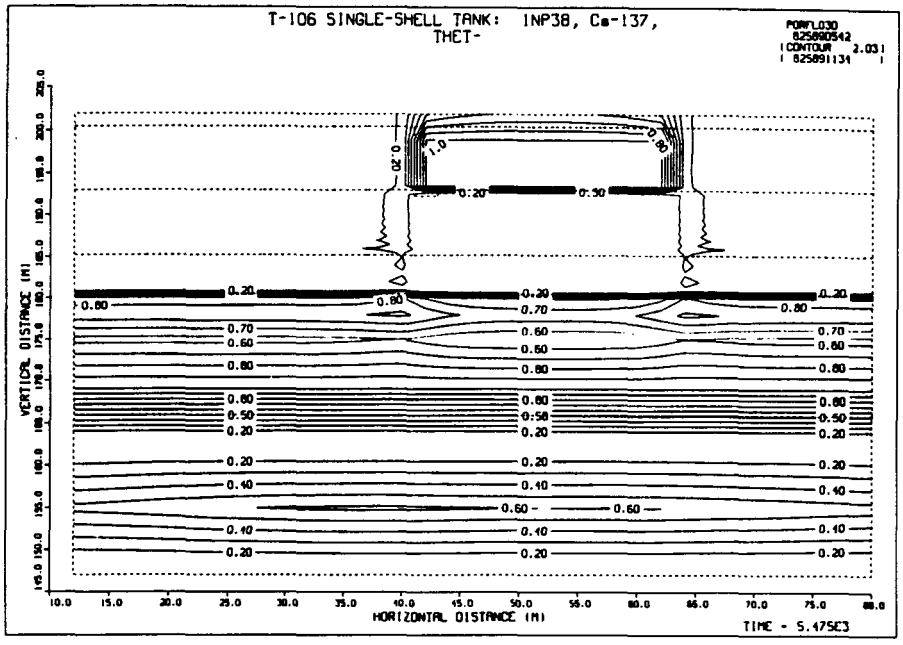

Figure 5-13. Calculated Relative Saturation 15 Years After Beginning of Leak (base case properties).

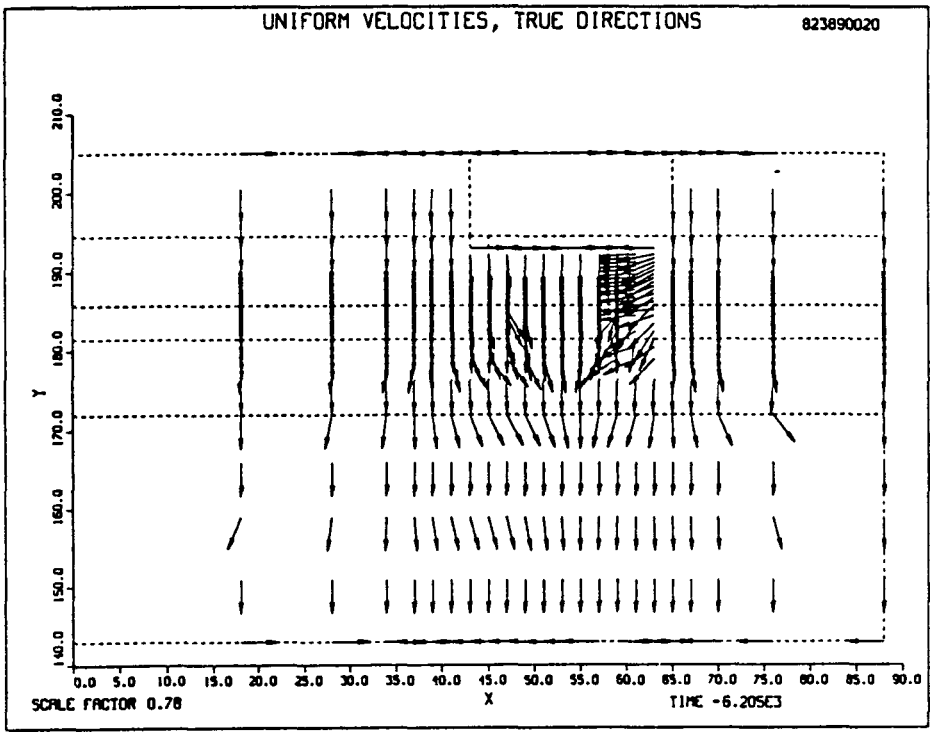

Figure 5-14. Darcy Velocity Vectors at 100 Days Showing Runoff from Tank Top (base case properties).

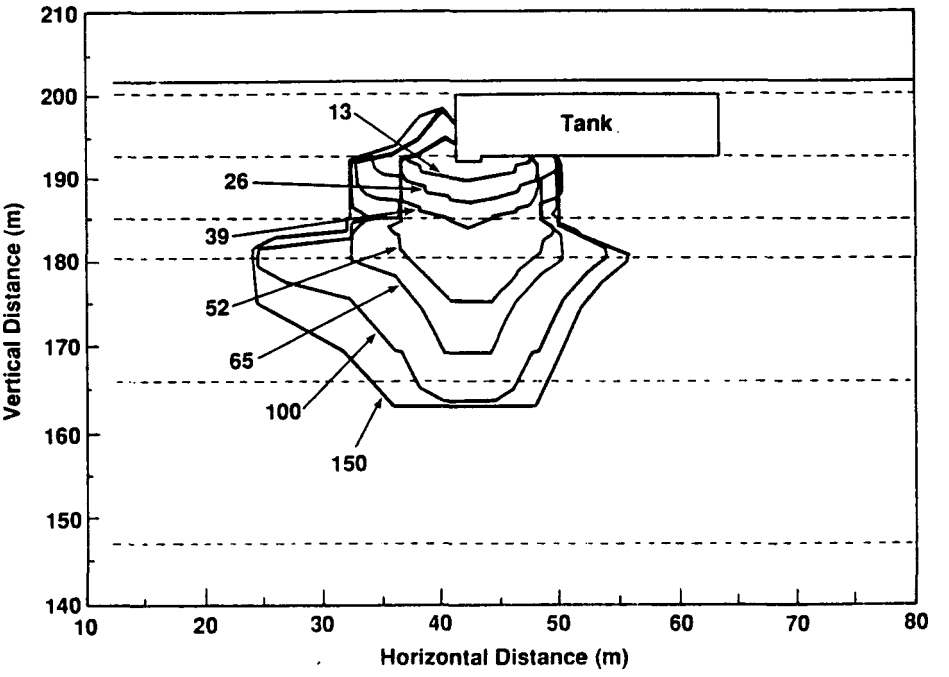

Figure 5-15. Calculated Vertical Extent of the ^{106}Ru 1-μCi/L Isopleth for Base Case Properties. Note: Times marked on the contours are in days.

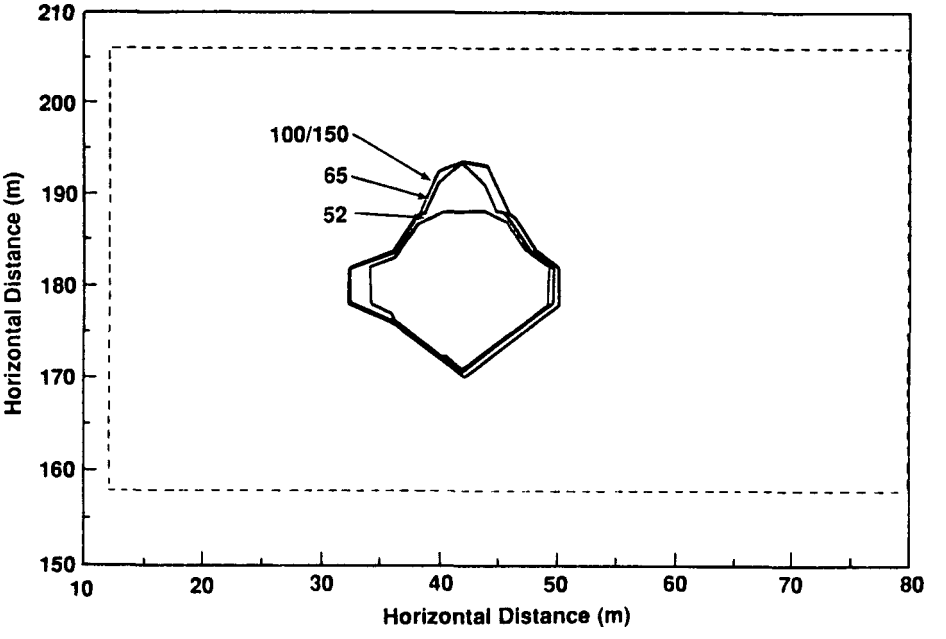

Figure 5-16. Calculated Horizontal Extent of the ^{106}Ru 1-μCi/L Isopleth for Base Case Properties. Note: Times marked on the contours are in days.

and indicates a 1-μCi/L ^{106}Ru isopleth of about 30-m diameter. This compares favorably with a diameter of 30 to 40 m of the measured horizontal spread reported by Routson et al. (1979).

Based on results depicted in Figures 5-15 and 5-16, several adjustments in the input data were made in order to better match the vertical extent of the ^{106}Ru plume. First, the vertical hydraulic conductivity (K_z) was reduced by a factor of two. This lower value of the hydraulic conductivity may be justified because of the higher viscosity (compared to that of water) of the supernate liquid.

Vertical and horizontal cross sections of the ^{106}Ru plume resulting from the adjusted Kz are shown in Figures 5-17 and 5-18, respectively, for the first 150 days of the leak. The calculated 150-day 1-μCi/L isopleth is now located approximately 20 m below the base of the tank, as reported by ARHCO (1973) and Routson et al. (1979). The diameter of the horizontal extent of the plume is still approximately 30 m, which compares favorably to the reported information. Consequently, the model appears to be reasonably well calibrated to the 1973 data.

The simulation was then resumed and run through 1990 in order to estimate the present-day extent of the plume. Figures 5-19 and 5-20 show the vertical and horizontal extent of the calculated plume for several years up to 1990. The model shows the 1-μCi/L ^{106}Ru isopleth migrating through much of the soil column down towards the water table by the early 1980's. Radioactive decay then appears to reduce the extent of the plume through the remainder of the time. However, the model projects that the 1-μCi/L ^{106}Ru isopleth will encompass a relatively large portion of the soil volume. This appears to be a consequence of the large initial inventory of ruthenium.

The degree to which ^{106}Ru is adsorbed in soils is uncertain. Ruthenium-106 species tend to be cationic below a pH of about 5 and anionic above pH 5. Because Hanford Site soils tend to be neutral to slightly basic and the supernate in the T-106 Tank had a pH of about 12, cation exchange is probably not a major cause of adsorption for ^{106}Ru. Coles and Ramspott (1982) and Ames and Rai (1978) both report ^{106}Ru moving approximately with the water through soil columns of varying composition, as was modeled by PORFLO-3. However, work by Murthy et al. (1983) indicated that there may be some small retardation factor (less than 5) associated with ^{106}Ru. Therefore, another simulation was made incorporating a small retardation factor. A K_d of 0.5 mL/g was used, resulting in R ranging between about 2.5 and 4 for various soil horizons. K_z was reset to the original value for the isotropic conditions in the original simulation.

The results of this simulation are shown in Figures 5-21 and 5-22 for both vertical and horizontal sections through the plume. The extent of the plume 150 days after the beginning of the leak is about 25 m below the base of the tank. The 1-μCi/L ^{106}Ru isopleth diameter at about 10-m depth is about 10 m. The vertical extent of the isopleth is similar to that reported by Routson et al. (1979), but the horizontal extent of the 1-μCi/L ^{106}Ru isopleth is somewhat smaller.

The isopleths at later times for small, nonzero K_d appear to be quite different from those obtained earlier with zero k_d. The nonzero K_d

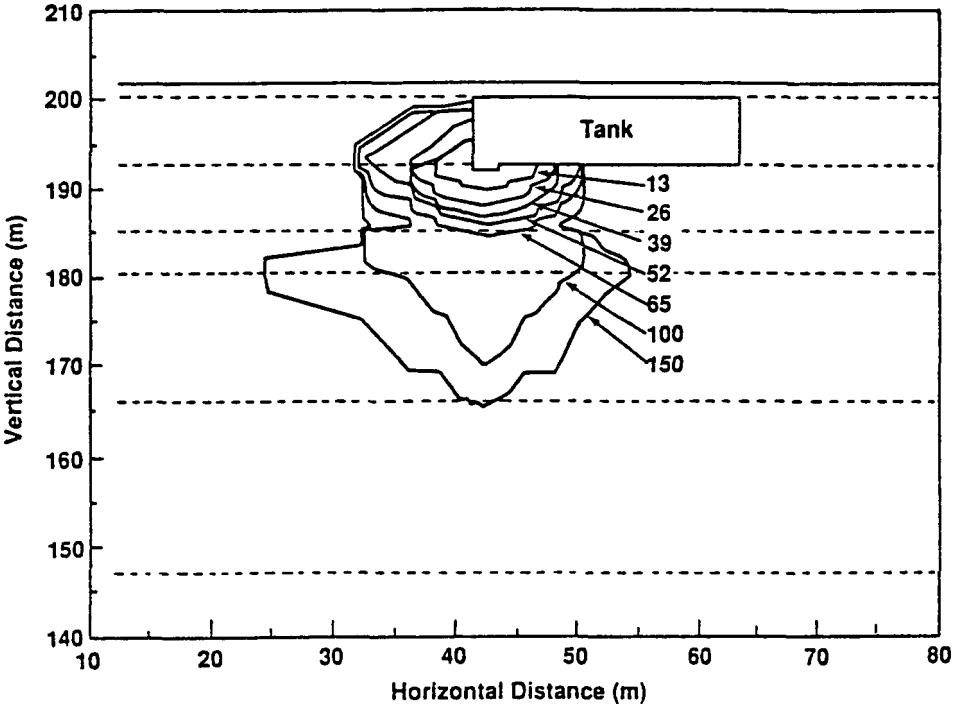

Figure 5-17. Calculated Vertical Extent of the ^{106}Ru 1-μCi/L Isopleth When K_z = Half of Base Case Value. Notes: Times marked on the contours are in days.

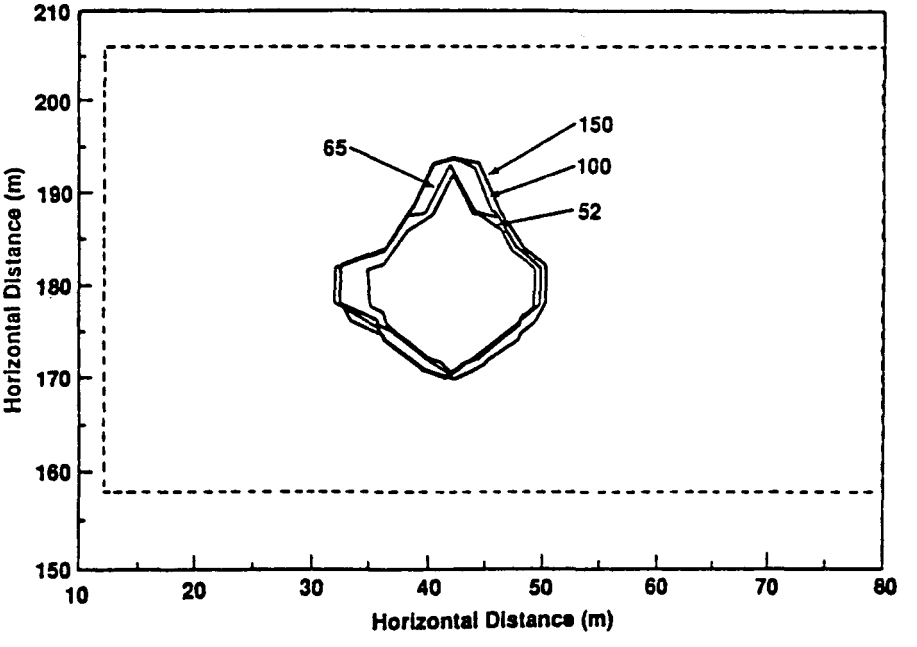

Figure 5-18. Calculated Horizontal Extent of the ^{106}Ru 1-μCi/L Isopleth When K_z = Half of Base Case Value. Note: Times marked on the contours are in days.

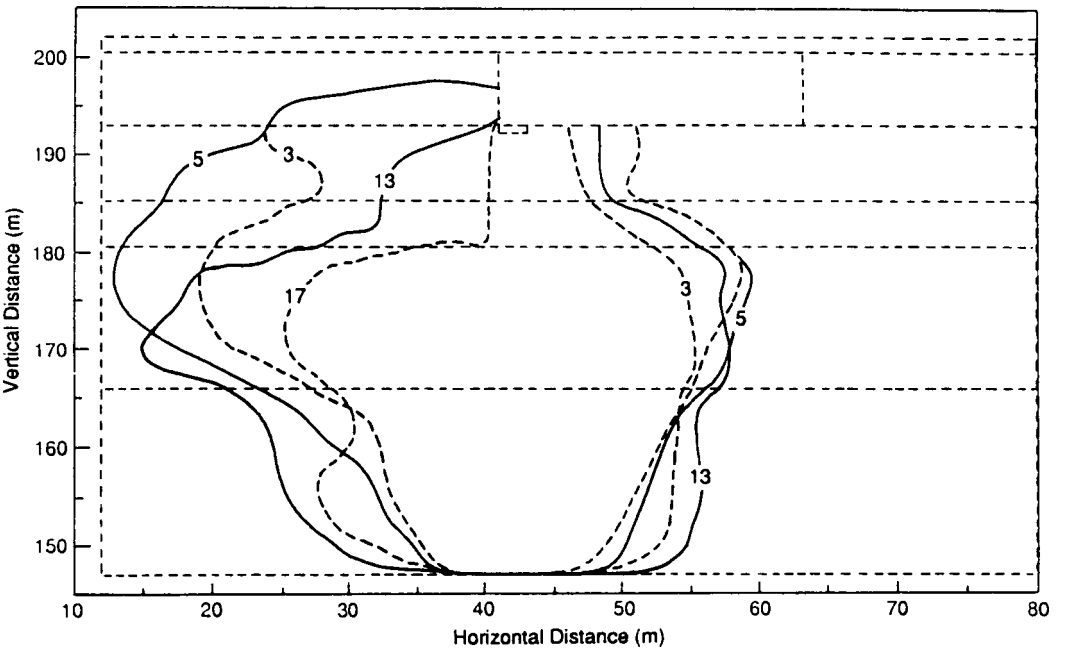

Figure 5-19. Development of the Vertical Extent of the ^{106}Ru 1-μCi/L Isopleth When K_Z = Half of Base Case Value. Note: Times marked on the contours are in years.

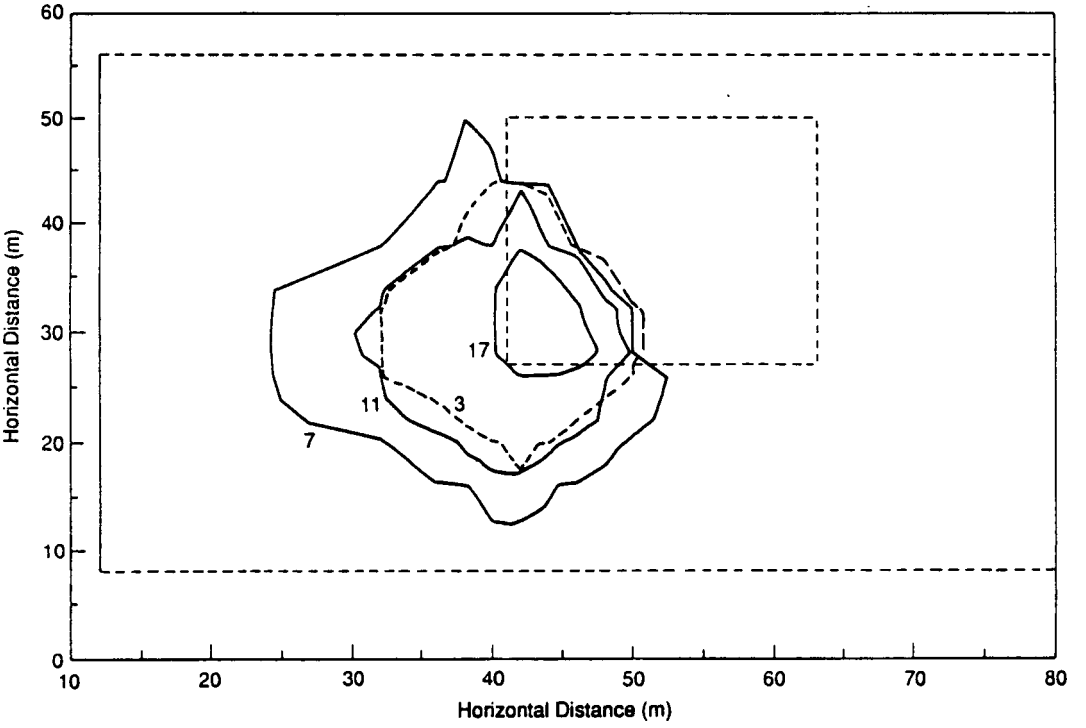

Figure 5-20. Development of the Horizontal Extent of the ^{106}Ru 1-μCi/L Isopleth When K_Z = Half of Base Case Value. Note: Times marked on the contours are in years.

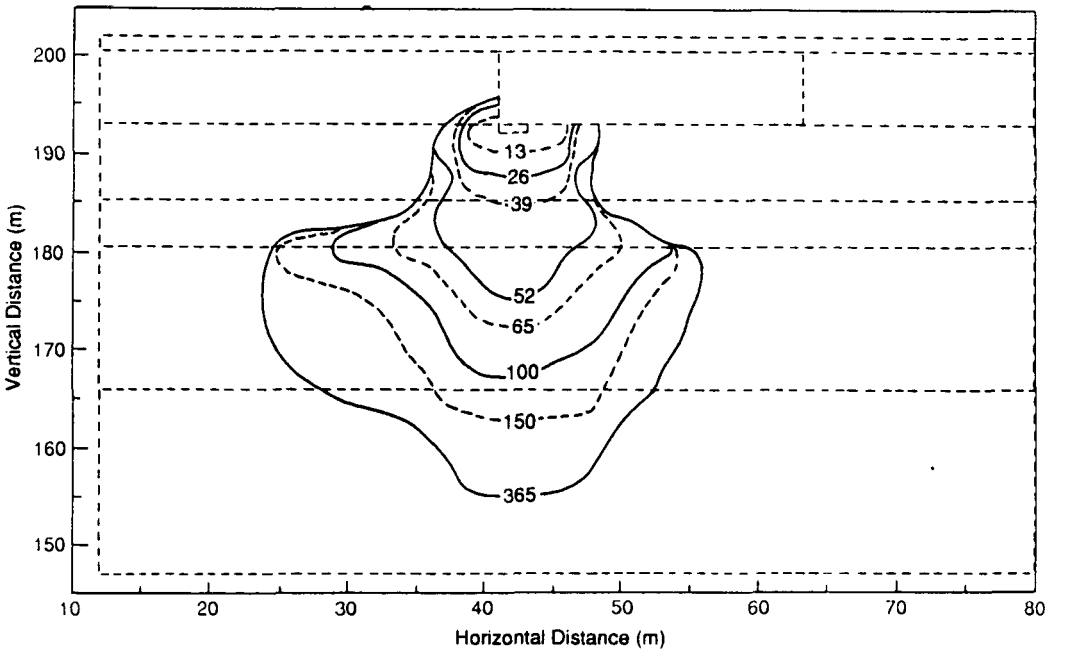

Figure 5-21. Calculated Vertical Extent of the ^{106}Ru 1-μCi/L Isopleth up to 1 Year After the Leak Began (Base Case K_z; K_d = 0.5 mL/g). Note: Times marked on the contours are in days.

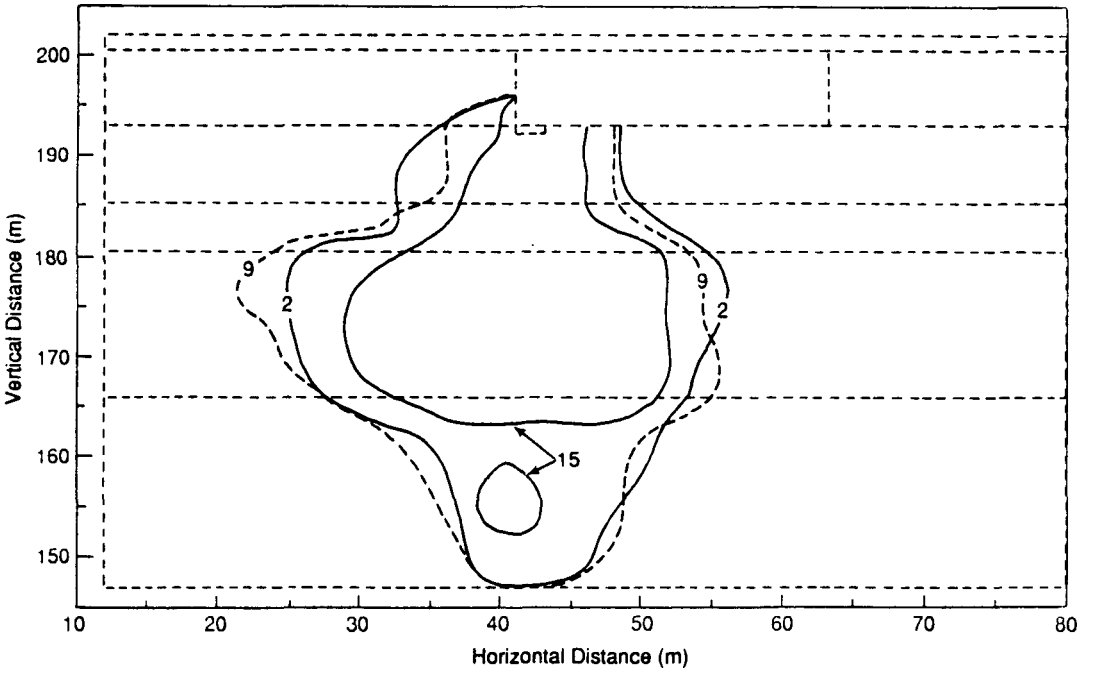

Figure 5-22. Calculated Vertical Extent of the ^{106}Ru 1-μCi/L Isopleth up to 15 Years After the Leak Began (Base Case K_z; K_d = 0.5 mL/g). Note: Times marked on the contours are in years.

simulation shows the 1-μCi/L ^{106}Ru isopleth migrating through much of the soil column down towards the water table by the early 1980s, but the plume seems to recede faster and farther at later times. Because the concentration is defined with respect to the bulk soil volume, it should be noted that a concentration of 1 μCi/L in the nonretarded case means a much higher concentration in the liquid compared to that in the retarded case. Therefore, in the retarded case, the mass moves slower and decays more in place than in the nonretarded case.

5.1.6.3 Cesium (^{137}Cs) Plume. A base case run was developed for ^{137}Cs very similar to that developed for ^{106}Ru. The same hydraulic properties were used in the simulation. Cesium-137 a half-life of about 1.1×10^4 days (30 yr) and is much less mobile in Hanford Site soils than ^{106}Ru. For the simulation, a K_d of 1.0×10^{-4} m^3/g (100.0 mL/g) was input, resulting in retardation coefficient values ranging between about 320 and 640.

The results for the ^{137}Cs base case are shown in vertical and horizontal cross sections in Figures 5-23 and 5-24, respectively. Migration of the 1-μCi/L ^{137}Cs isopleth occurred to a depth of only several meters below the tank after 150 days from the beginning of the leak. This movement compares favorably with observations in the dry wells adjacent to the tank as reported by Routson et al. (1979). Cesium-137 is relatively highly retarded in Hanford Site soils, and the smaller plume movement compared to ^{106}Ru would be expected. The horizontal spread of 5 to 10 m also compared favorably to that reported by Routson et al. (1979). Extension of the simulation through 1990 produced very little change in the shape of the plume compared to that which developed by about 65 days. The model does not show any redistribution or reduction in the plume. This would appear reasonable given the high sorption and large half-life for ^{137}Cs.

5.1.7 Summary of First Application Example

The first application example presents an attempt at calibrating a three-dimensional transient model to observed field data. The calibrated model then is used to project the results beyond the measurement period.

The release of large amounts of fluid and contaminants from the 241-T-106 single-shell waste storage tank in 200 West Area of the Hanford Site was simulated with PORFLO-3. The release occurred over a period of 52 days in the summer of 1973. For purposes of modeling, release was assumed to occur at a uniform rate during the period of release. The tank itself was assumed to be impermeable except for a small tear at the southwest end of the base from where the leak occurred. Soil properties for the simulations were estimated from a catalogue of Hanford Site soil properties.

The model was calibrated to the measured data of 1973. For ruthenium, the most mobile constituent, a reduction of the saturated hydraulic conductivity alone produced a calculated plume that was very similar to the measured plume. Considering that the hydraulic conductivity used initially was for water, while the leaked liquid was more viscous, this reduction in permeability is not unjustified from a practical point of view.

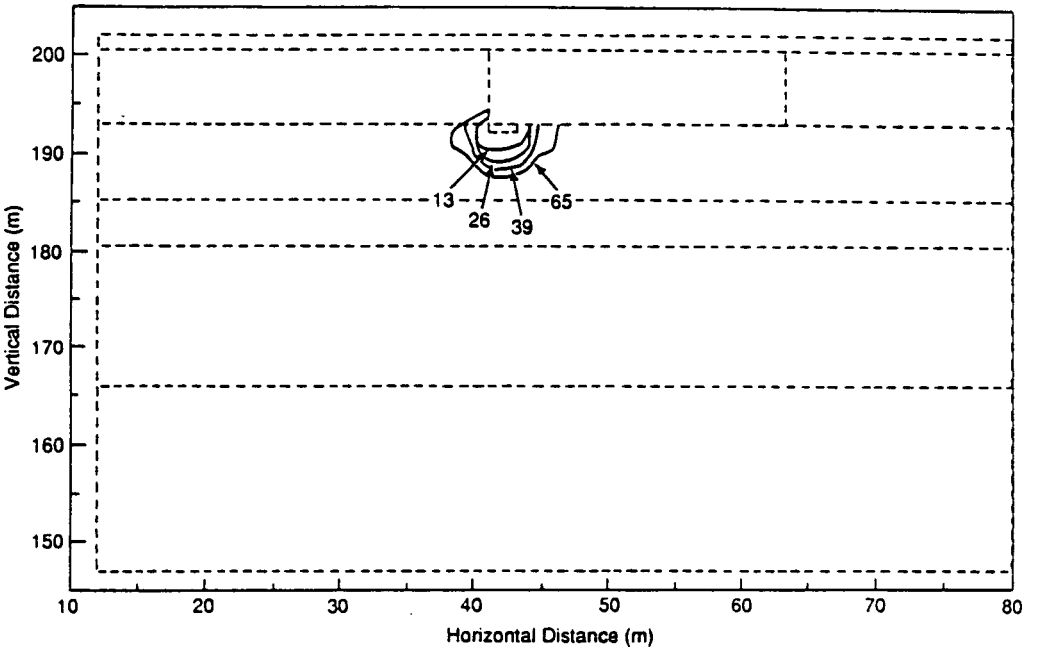

Figure 5-23. Calculated Vertical Extent of the ^{137}Cs 1-μCi/L Isopleth for Base Case Properties. Note: Times marked on the contours are in days.

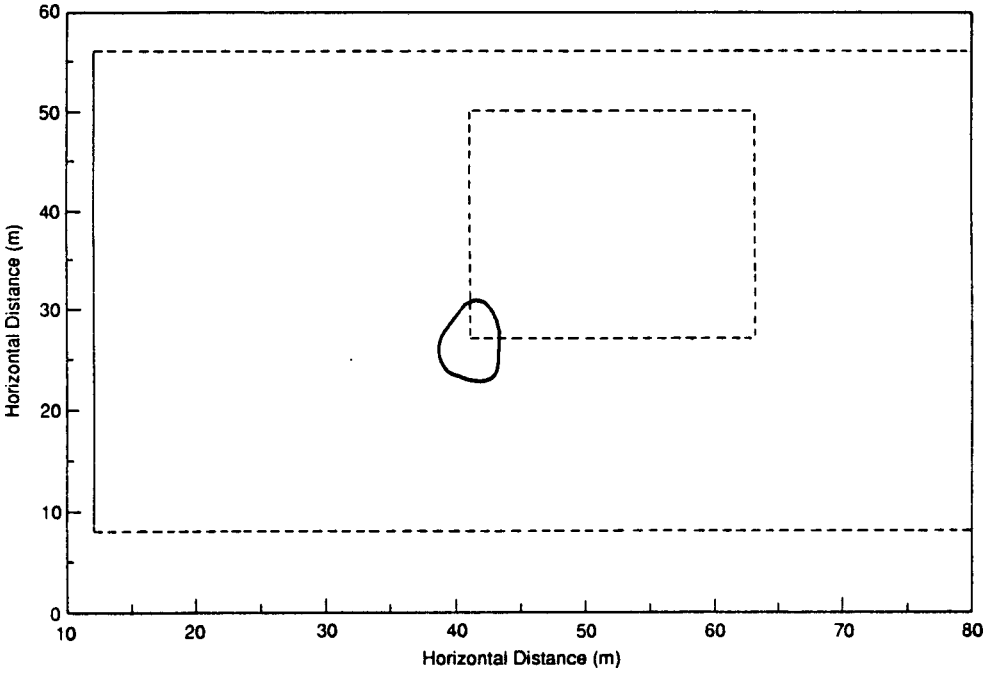

Figure 5-24. Calculated Horizontal Extent of the ^{137}Cs 1-μCi/L Isopleth for Base Case Properties. Note: Times marked on the contours are are in days.

The ^{137}Cs plume was approximated using a reasonable K_d. The model results indicate that the plume would penetrate only several meters below the base of the tank and would become essentially stationary within about a month after the tank was pumped out, stopping the leak.

Preliminary calibration results indicate that, for the first 150 days, convection was the dominant phenomena, and the plume migration was dominated by the large leak volume rather than the recharge rate. At later simulation times, reduction in the ^{106}Ru plume by radioactive decay was very evident.

5.2 EXAMPLE TWO: THREE-DIMENSIONAL FLOW IN THE PRESENCE OF LINEAR AND PLANAR FEATURES

5.2.1 Description of Simulation Scenario

The DOE is investigating the suitability of Yucca Mountain Site in Nevada for long-term containment of high-level nuclear waste (DOE 1989). The waste repository is expected to be located in the vadose zone above the water table in a welded tuff formation.

The exploratory shaft facility (ESF) forms an important part of the subsurface-based site characterization activities that are outlined in the Site Characterization Plan (DOE 1989). The ESF consists of surface facilities and underground excavations as depicted in the conceptual picture shown in Figure 5-25. The underground excavations include two 12-ft finished-diameter shafts (called ES-1 and ES-2), an upper demonstration breakout room off of ES-1, and about 10,000 ft of drifts in the repository horizon. While the construction and operation methods would be selected to minimize rock disturbances, some alterations in properties of rocks close to the excavations are to be expected. The objective of this application is to investigate the influence of these altered rock zones on moisture distribution. This example problem is limited to investigation of either short-term (on the order of 20 yr) or extremely long-term (steady-state) impacts of the ESF on the vadose zone moisture distribution. The short-term effects, if any, may be important in the planning and interpretation of the tests scheduled to be performed in the ESF. Where not available, parameter values are freely assumed to complete the simulation. The results, therefore, should be treated more as an illustration of model capabilities and not as a definitive study of Yucca Mountain ESF.

In order to study the spatial effects of the ESF, three-dimensional geometry is used in the simulations. The exploratory shafts and drifts and the altered property rock zones [called the Modified Permeability Zones (MPZ) in the context of hydrology] associated with them are represented as one-dimensional "line elements" that are embedded in the general three-dimensional elements. The Ghost Dance fault, one of the prominent structural and hydrological features at the site, also is included in the calculation domain. This fault is represented as a two-dimensional "planar element." Results of both steady-state and transient simulations are presented.

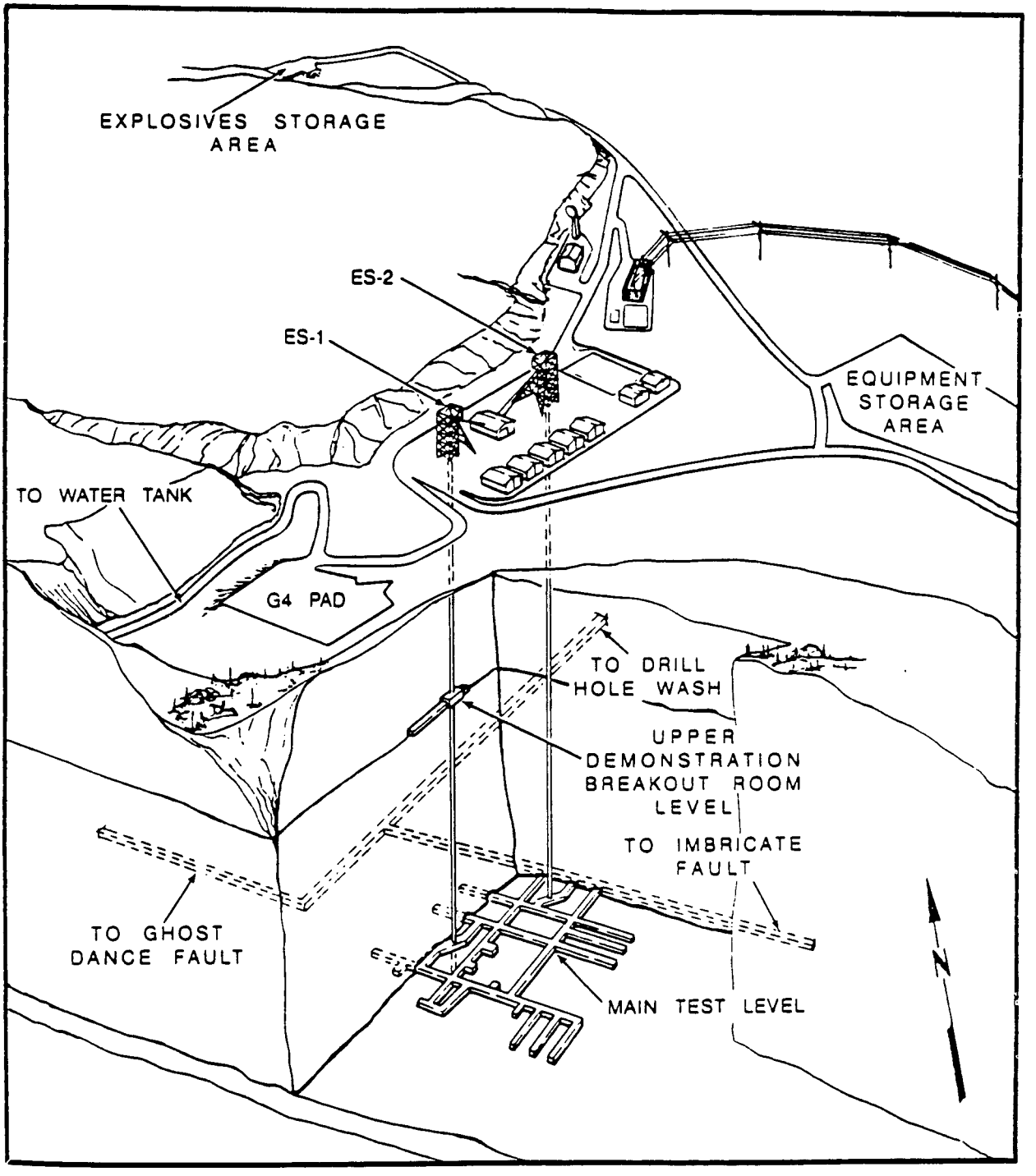

Figure 5-25. Conceptual Illustration of the Exploratory Shaft Facility (after DOE 1988).

5.2.2 Site Hydrogeology and Conceptual Model

For the purpose of these simulations, the lithologic units at Yucca Mountain have been depicted as the five hydrologic units shown in Figure 5-26. From top, these units are Tiva Canyon welded unit (TCw), Paint Brush nonwelded unit (PTn), Topopah Springs welded unit 1 (TSw1), Topopah Springs welded units 2 and 3 (TSw2-3) treated as a single composite unit, and Calico Hills nonwelded unit (CHn). The respective thicknesses of these units are 25, 40, 130, 205, and 190 meters. The relative elevations (rounded to whole numbers) of various units taken from Peters et al. (1986) also are indicated in Figure 5-26. These relative elevations of the units are based on the stratigraphy of drill hole USW-G4, which is located near the eastern edge of the prospective repository boundary. The decision to treat TSw2 and TSw3 as a single composite unit (TSw2-3) is based on the relatively small thickness of TSw3 (15 m) relative to that of TSw2, which is 115 m, and the similar hydrologic properties of the two units. Unit TSw3 is the prospective repository horizon.

Computations are performed in a three-dimensional Cartesian grid system. The axes of this system are aligned with east-west (x-axis), north-south (y-axis), and vertical (z-axis). The dimensions of the calculation domain are 615 m, 300 m, and 530 m in the x-, y-, and z-directions, respectively. A total of 25,056 nodes (29 in the x-, 16 in the y-, and 54 in the z-direction) discretize this domain for numerical calculations. This grid is shown in Figure 5-27. Within the domain, the Ghost Dance fault, which is located

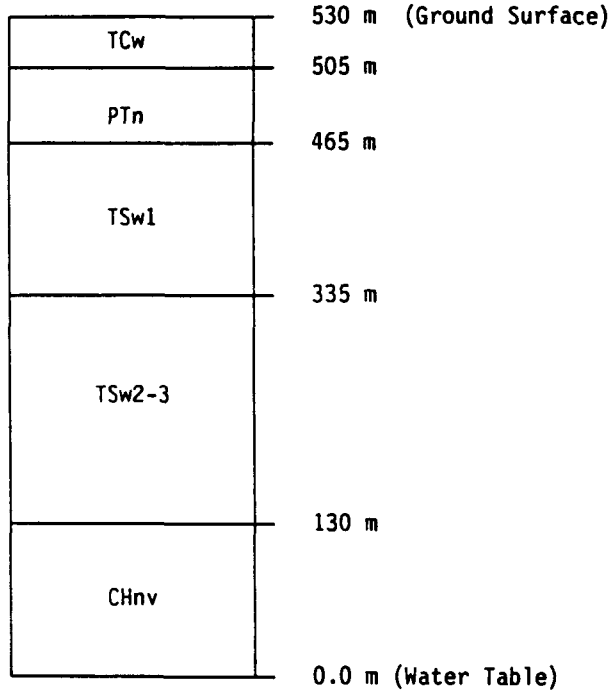

Figure 5-26. Hydrologic Units and Their Relative Elevations (after Peters et al. 1986).

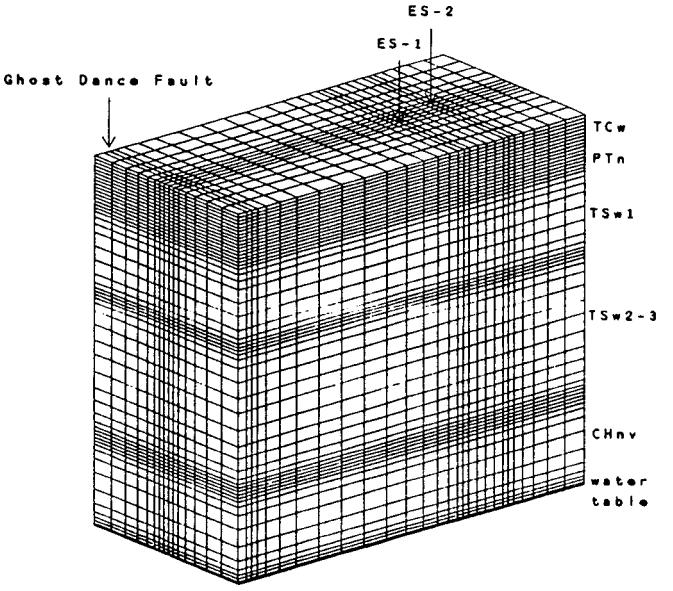

Figure 5-27. Three-Dimensional Computational Grid for Example Problem Two.

near the west boundary, is represented with a vertical planar (two-dimensional) element extending from the ground surface to the water table. The exploratory shafts (ES-1 and ES-2) are represented as vertical line (one-dimensional) elements extending from the surface to a depth of approximately 310 m into the repository horizon. The shaft elements are connected by horizontal line elements, representing connecting drifts, at the 310-m depth in unit TSw2-3. The shafts and fault are positioned within the model domain with reference to borehole USW-G4. The relative locations of these features with respect to USW-G4 were determined from a report by Fernandez et al. (1988) and the geologic map of Yucca Mountain by Scott and Bonk (1984).

The exploratory shafts and drifts are modeled as line elements with a diameter of 4.4 m. The shafts as well as the drifts are assumed to have zones of modified permeability around them. For the simulations reported here, the MPZs are assumed to extend 1 m past the edges of the shafts and drifts. As is evident from Figure 5-27, finer grids are used close to the shafts, drifts, and the Ghost Dance fault.

5.2.3 Hydrogeologic Parameters

The welded tuff units (TCw, TSw1, and TSw2-3) are distinguished hydrologically from the nonwelded units (PTn and CHn) by the number of fractures contained in them. Table 5-1 lists the fracture characteristics of the five tuff units.

Table 5-1. Fracture Characteristics of Hydrologic Units.

Unit	Sample Program	Fracture aperture (microns)	Fracture density[a] (no./m^3)	Fracture porosity[b]	Fracture conductivity (m/s)
TCw	G4-2F	6.74	20	14.0 E-5	3.8 E-05
PTn	G4-3F	27.00	1	2.7 E-5	6.1 E-04
TSw1	G4-2F	5.13	8	4.1 E-5	2.2 E-05
TSw2-3	G4-2F	4.55	40	18.0 E-5	1.7 E-05
CHn	G4-4F	15.50	3	4.6 E-5	2.0 E-04

[a]Based on a report by Scott et al. (1983).
[b]Calculated as fracture volume (aperture times 1 m^2) times number of fractures per m^3.

From Table 5-1, it is apparent that a large number of small fractures occur in the welded tuff units. The hydrologic properties of the rock matrix and the fractures may differ considerably. The parameters of the Van Genuchten (1978) water retention and hydraulic conductivity [using Mualem (1976) model] curves for the rock matrix of the five hydrologic units are in Table 5-2 (Peters et al. 1986).

Table 5-2. Van Genuchten Parameters for Matrix Hydrologic Properties.

Unit	Sample Program	Grain density (g/cm^3)	Porosity	Hydraulic conductivity (m/s)	S_r[a]	α[a] (1/m)	n[a]
TCw	G4-1	2.49	0.08	9.7 E-12	0.002	8.21 E-3	1.558
PTn	GU3-7	2.35	0.40	3.9 E-07	0.100	1.50 E-2	6.872
TSw1	G4-6	2.58	0.11	1.9 E-11	0.080	5.67 E-3	1.798
TSw2-3	G4-6	2.58	0.11	1.9 E-11	0.080	5.67 E-3	1.798
CHn	GU3-14	2.37	0.46	2.7 E-07	0.041	1.60 E-0	3.872

[a]The Van Genuchten water-retention curve is
$|\theta^*| = [1 + (\alpha\psi)^n]^{-m}$; $m = (1 - 1/n)$

The corresponding parameters for a fracture are estimated by Wang and Narasimhan (1985) to be $\theta r = 0.0395$, $\alpha = 1.2851/m$, $n = 4.23$.

In this analysis, rather than represent the fractures as discrete elements, an "equivalent continuum" is stipulated in which the fractured medium is considered as a continuum, which is assigned equivalent or composite properties. A weighting procedure is used by Klavetter and Peters (1986) to obtain the composite properties; i.e.,

$$K_C = K_m(1 - \phi f) + K_f\phi f,$$

where K_f, K_m, and K_c are, respectively, the fracture, matrix, and composite permeabilities, and ϕ_f is the fracture porosity. Because of the relatively few fractures in the two nonwelded units, their composite properties are assumed to be the same as those of the rock matrix. Thus, for the Paint Brush and Calico Hills nonwelded units, the properties listed in Table 5-2 are used directly. A graphical representation of properties of these two units is shown in Figures 5-28 and 5-29. In Figures 5-28A and 5-29A, hydraulic conductivity is plotted as a function of water tension. In Figures 5-28B and 5-29B, relative hydraulic conductivity and saturation are shown as functions of water tension. The curve of Figure 5-28b is used in the numerical model.

Figure 5-30A shows the hydraulic conductivity curves for the matrix and fractures for the Tiva Canyon welded unit. The composite hydraulic conductivity curve is also shown in this figure. A large jump in the value of the composite hydraulic conductivity at a specific value of the water tension ($\approx$ 1 m in Figure 5-30A) is a primary characteristic of the composite curve. In physical terms, it indicates that at a specific value of water tension (or equivalently at a specific value of moisture content), flow switches from the matrix to the fracture and vice versa. This abrupt change in the hydraulic conductivity introduces a large amount of nonlinearity in the problem, which can lead to numerical instabilities, as was observed in some of the solutions. Figure 5-30B shows the composite relative conductivity and moisture content as functions of the water tension for the Tiva Canyon unit. Figures 5-31 and 5-32 show the composite hydrologic properties of the Topopah Springs and Calico Hills units, respectively. In the numerical model, to accurately represent the abrupt changes, the hydrologic properties of the TCw, TSw1, and TSw2-3 are introduced in a tabular form (rather than the analytic Van Genuchten relation).

Calculations based on these properties assume each unit to be homogeneous and isotropic, except where hydraulic properties have been modified for the shafts, drifts, and MPZs associated with the ESF and the Ghost Dance fault. These calculations also assume isothermal conditions, although the program used also will solve nonisothermal flow and transport problems.

The water-retention curves for MPZs associated with the shafts and drifts in each unit are assumed to be the same as those of the rock matrix of that unit. However, the saturated hydraulic conductivities of the MPZs are assumed to be 40 and 80 times higher than those of the undisturbed matrix in units TSw1 and TSw2-3, respectively. These multiplying factors are based on a study reported by Case and Kelsall (1987) (Table 5-3) and corresponds to their upper-bound case.

The saturated hydraulic conductivity of the MPZ in unit TCw also was assumed as an upper bound to be 80 times higher than the matrix hydraulic conductivity of this unit. This assumption was based on the similarity of fracture densities and porosities between unit TCw and unit TSw2-3, as shown in Table 5-1. For the nonwelded units (PTn and CHn), the saturated hydraulic conductivities of the MPZs were assumed to be 20 times higher than the hydraulic conductivities of the matrix of each unit. The nonwelded units have a much higher porosity and lower fracture density than the welded units.

A

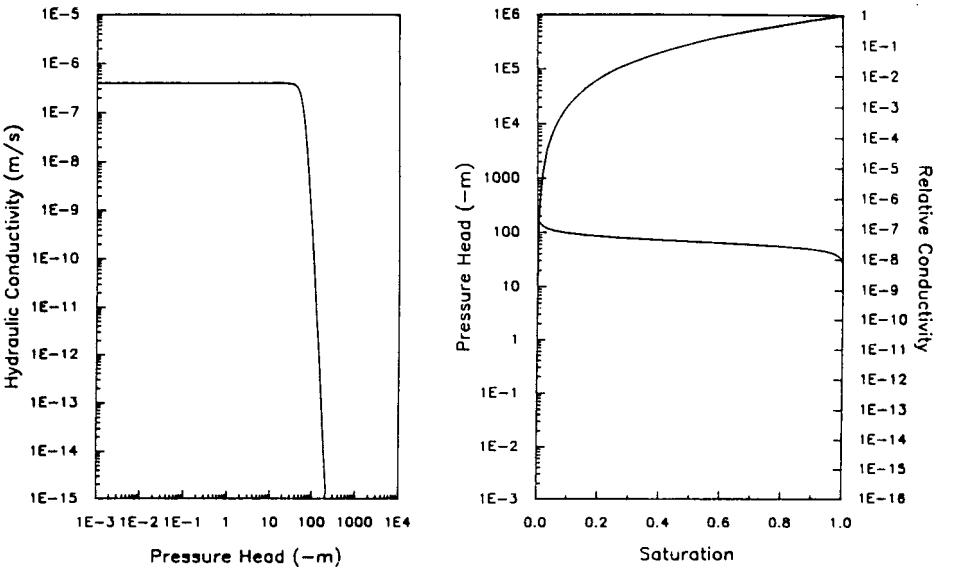

B

Figure 5-28. Characteristic Curves for the Paint Brush Nonwelded Tuff Unit. (A) Hydraulic Conductivity versus Moisture Tension (Peters et al. 1986). (B) Saturation and Relative Conductivity versus Moisture-Tension Curves Used in Computations.

A

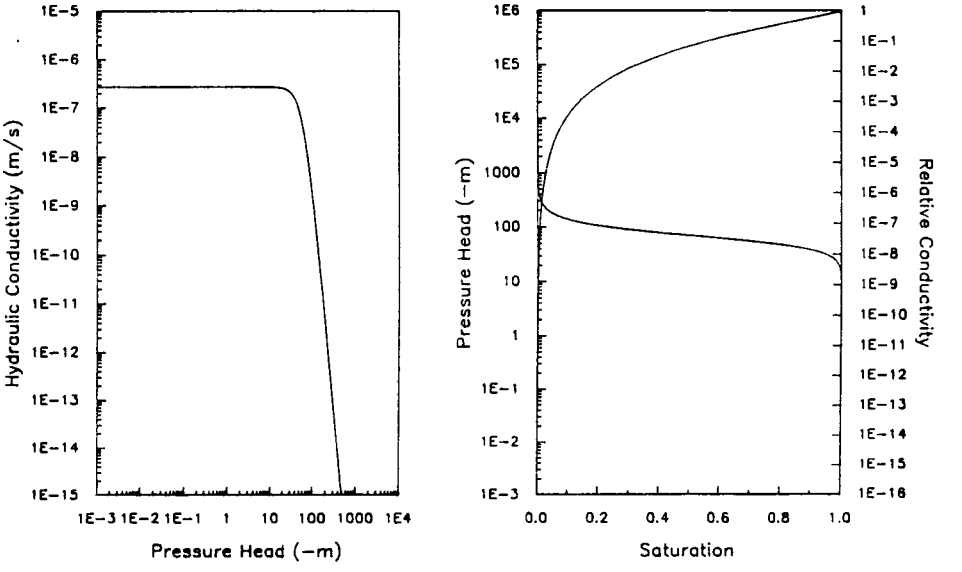

B

Figure 5-29. Characteristic Curves for the Calico Hills Nonwelded Tuff Unit. (A) Hydraulic Conductivity versus Moisture Tension (Peters et al. 1986). (B) Saturation and Relative Conductivity versus Moisture-Tension Curves Used in Computations.

A

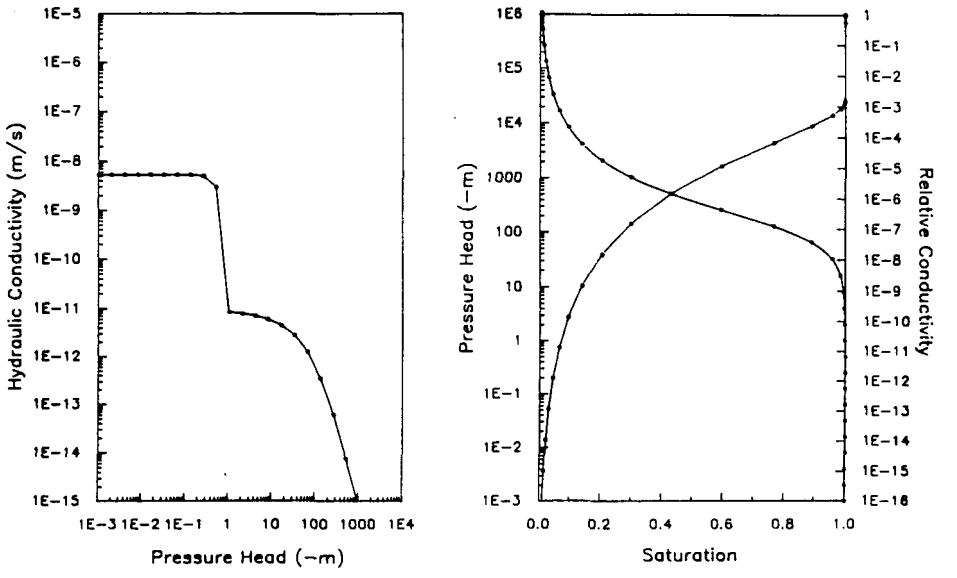

B

Figure 5-30. Characteristic Curves for the Tiva Canyon Welded Tuff Unit. (A) Hydraulic Conductivity versus Moisture Tension (Peters et al. 1986). (B) Saturation and Relative Conductivity versus Moisture-Tension Curves Used in Computations.

A

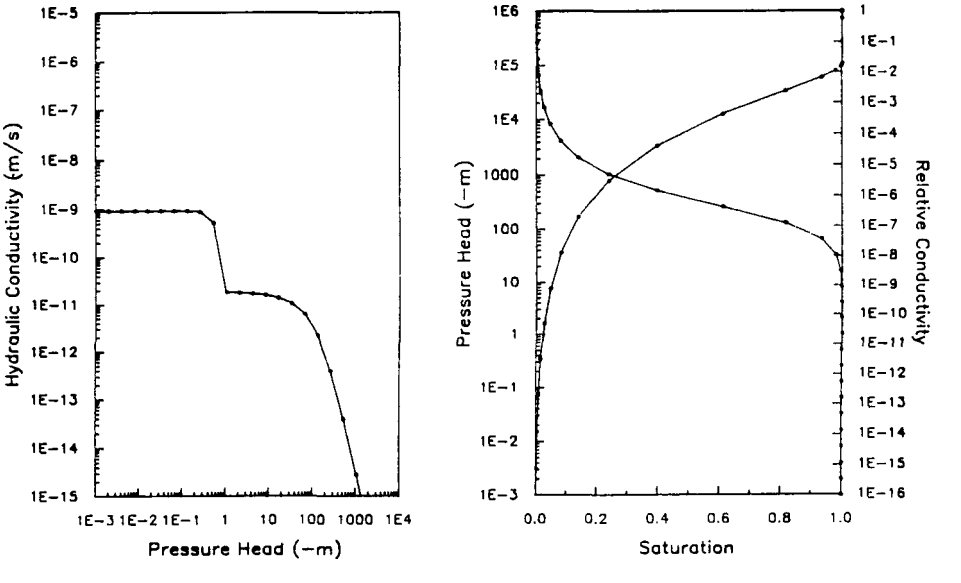

B

Figure 5-31. Characteristic Curves for the Topopah Springs Welded Tuff Unit. (A) Hydraulic Conductivity versus Moisture Tension (Peters et al. 1986). (B) Saturation and Relative Conductivity versus Moisture-Tension Curves Used in Computations.

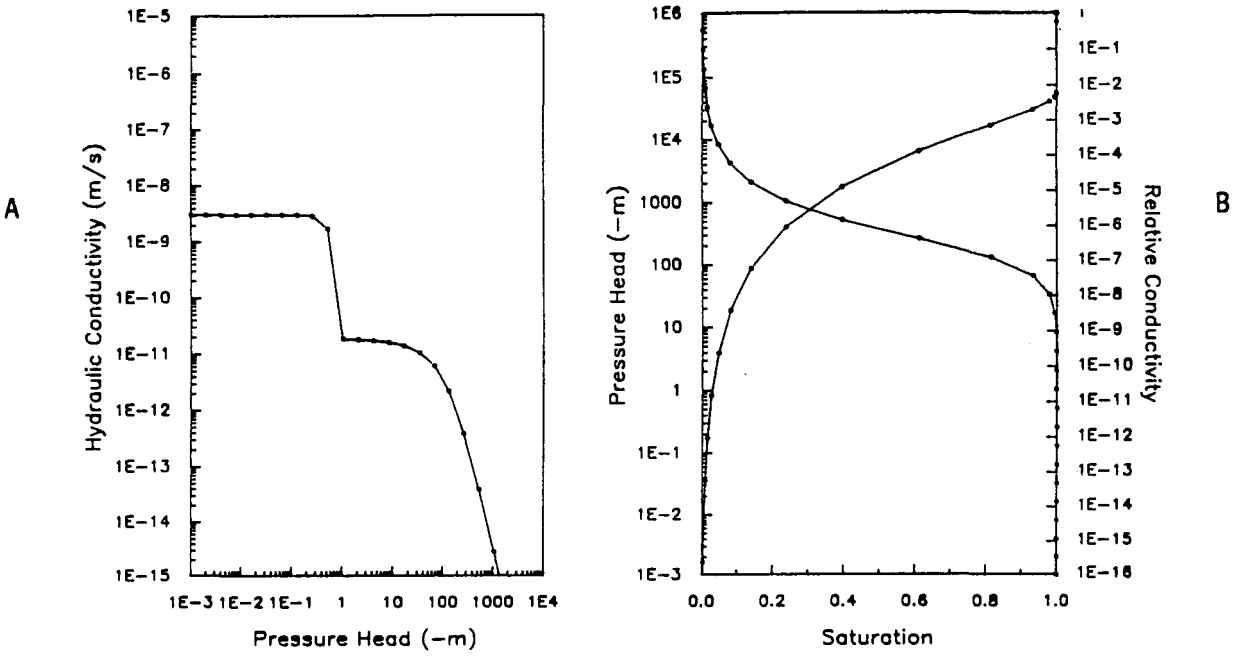

Figure 5-32. Characteristic Curves for the Calico Hills Welded Tuff Unit. (A) Hydraulic Conductivity versus Moisture Tension (Peters et al. 1986). (B) Saturation and Relative Conductivity versus Moisture-Tension Curves Used in Computations.

Table 5-3. Saturated Permeability of the Modified Permeability Zone.[a]

Depth (m)	Stress redistribution without blast damage		Expected[b] case	Upper-bound[c] case
	Elastic	Elastoplastic		
100	15	20	20	40
310	15	40	20	80

[a]Equivalent permeability is averaged over an annulus 1 radius wide around the 4.4-m (14.5-ft) diameter exploratory shaft.

[b]This is based on an elastic analysis with expected strength, in situ stress, sensitivity of permeability to stress, and a 0.5-m-wide blast-damage zone.

[c]This is based on an elastoplastic analysis with lower-bound strength, upper-bound stress, greatest sensitivity of permeability to stress, and a 1.0-m-wide blast-damage zone.

Therefore, it was assumed that permeability modifications resulting from shaft construction in these units would be less extensive than for the welded units.

The hydraulic properties of the shafts and drifts are represented with parameters describing the properties of a coarse-grained material such as gravel with a high porosity. The Van Genuchten moisture-retention curve parameters used are α = 1.0 and n = 6.2. Figure 5-33 shows these curves graphically. The water-retention characteristics described by these parameters create a capillary barrier that effectively restricts flow into the shafts and drifts until the surrounding MPZs are close to saturation. Each section of the shafts and drifts is assigned a saturated hydraulic conductivity value equal to that of the MPZ adjacent to it. Thus, the maximum rate at which water flows through the shaft and drift subdomain elements is governed by the saturated hydraulic conductivity of the adjacent MPZs.

No data regarding the hydraulic properties of the rubblized shear zone around the Ghost Dance fault are presently available. Therefore, the fault MPZ was modeled as a 0.5-m-wide zone with the matrix-retention properties of each unit and saturated hydraulic conductivities 40 times greater than that of the undisturbed saturated matrix of each unit.

5.2.4 Initial and Boundary Conditions

Saturation percentages determined from core samples from various units at the Yucca Mountain have been reported by Montazer and Wilson (1984). From these reported saturation percentages, using the matrix water-retention curves described in Section 5.2.3, initial capillary pressure heads are calculated to be input as initial conditions. These initial pressure heads for various hydrologic units are listed in Table 5-4. Within a unit, the initial

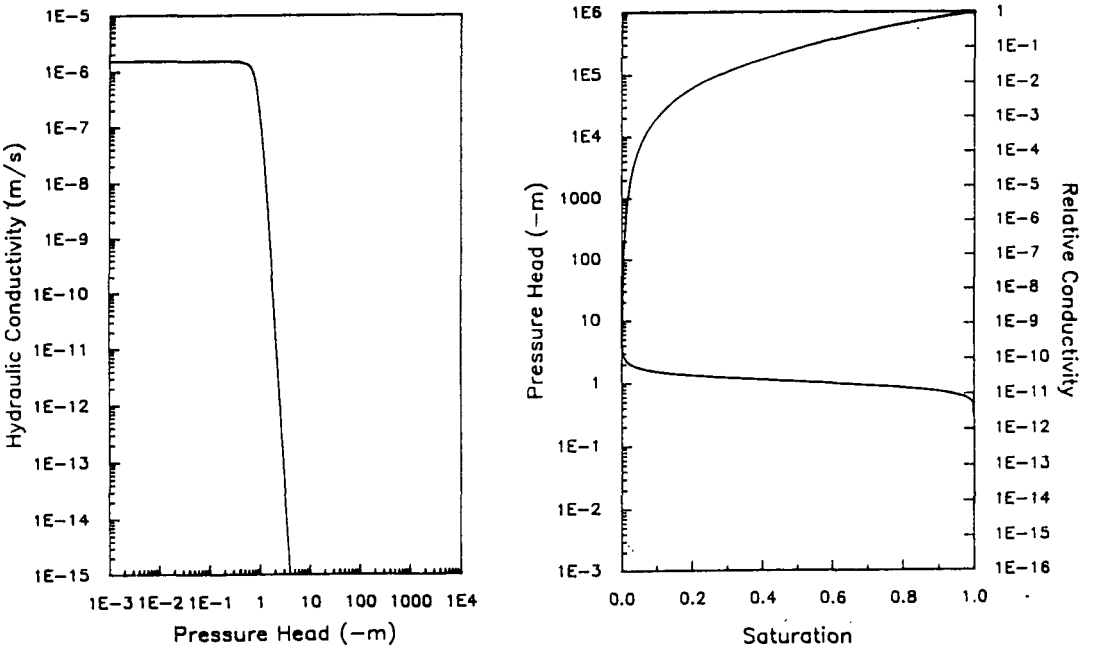

Figure 5-33. Characteristic Curves for the Shafts.

condition is assumed to be uniform. Because of the nonlinearity in the unsaturated flow problem, specification of representative initial conditions is critical in order to obtain reasonably accurate solutions. This will be discussed more thoroughly in the following section.

The regional dip of the units at Yucca Mountain is 5 to 7 degrees to the east (Scott and Bonk 1984). This creates a driving force in the lateral (down-dip) direction that is approximately 10% of gravity. This is not directly accounted for in the model. The left (west) boundary, however, is specified to be a "no-flow" boundary so that water cannot move up dip. The boundary condition at the ground surface is specified as a flux boundary with specified fluxes representing variable recharge rates. The lower boundary is specified as a fixed-pressure (atmospheric) boundary representing the water table. All other boundaries were fixed-pressure boundaries, with pressures corresponding to the initial conditions listed in Table 5-4.

5.2.5 Simulation Results

5.2.5.1 Steady-State Simulations. There are two possible strategies for obtaining steady-state solutions. In the first, solution is obtained by solving a transient problem until steady state is reached. In the second strategy, the storage term in the governing equation is set equal to zero and a direct steady-state solution is obtained without any time stepping. The second strategy was followed here because it was less computer-time intensive.

For the steady-state solution, the recharge rate at the ground surface was varied from 0.1 to 4.0 mm/yr. The direct steady-state solutions did not converge when the recharge fluxes were high (1 to 4 mm/yr). The primary cause of this divergence was found to be the abrupt change in composite hydraulic conductivity of the TCw (see Figure 5-30A). With large recharges, pressures develop that indicate beginning of fracture flow (i.e., saturation becomes close to 1), yet the recharge is not large enough to steadily sustain this fracture flow. The result is that the solution alternated between matrix and fracture flow between iterations and could not settle at a steady value. In experimenting further with the high recharge cases, increasing the saturated hydraulic conductivity of the TCw unit by a factor of 25 was determined to be sufficient for successful convergence. In the results presented for the steady state, the saturated hydraulic conductivity of the Tiva Canyon was assumed to be higher by a factor of 25. For the transient case, however, this factor was not used.

Table 5-4. Initial Conditions for Various Hydrologic Units.

Unit	Average relative saturation	Initial ψ(-m)
TCw	0.67	194
PTn	0.61	64
TSw-1	0.65	232
TSw2-3	0.65	232
CHn	0.90	38

By increasing the saturated hydraulic conductivity, higher recharge fluxes could pass through the Tiva Canyon unit and into the underlying Paint Brush tuff unit without alternating between the fracture and matrix flow between iterations. The same effect could potentially be achieved by modifying the initial pressures specified for the TCw unit so that the unit maintains saturated or near-saturated conditions. Otherwise, for direct steady-state simulations at high recharge fluxes, much finer spatial discretization in the vertical direction may be needed. Steady-state solutions converged without any hydraulic property modifications; however, when the recharge flux was sufficiently low, fracture flow in the TCw unit never occurred (i.e., < 0.3 mm/yr).

The following results represent steady-state simulations with upper-bound MPZ properties (see Table 5-4), at a recharge rate of 4.0 mm/yr. Relative saturation through a vertical cross section through the seventh y-plane (through ES-1) is shown in Figure 5-34. The relative saturation percentages of each of the units have changed considerably from the initial conditions, but no distinct patterns showing the effects of the ESF or Ghost Dance fault are evident from this cross section. If the specified initial conditions are assumed to represent a quasi-steady-state system (in the absence of the ESF), and the hydrologic properties are correctly specified, the higher moisture contents obtained in this solution indicate that the long-term infiltration rate at the Yucca Mountain should be lower than the 4 mm/yr assumed here. The bending of the contours on the right (east) side of the model domain, shown in Figure 5-34, indicates that the fixed-pressure boundaries are influencing the solution.

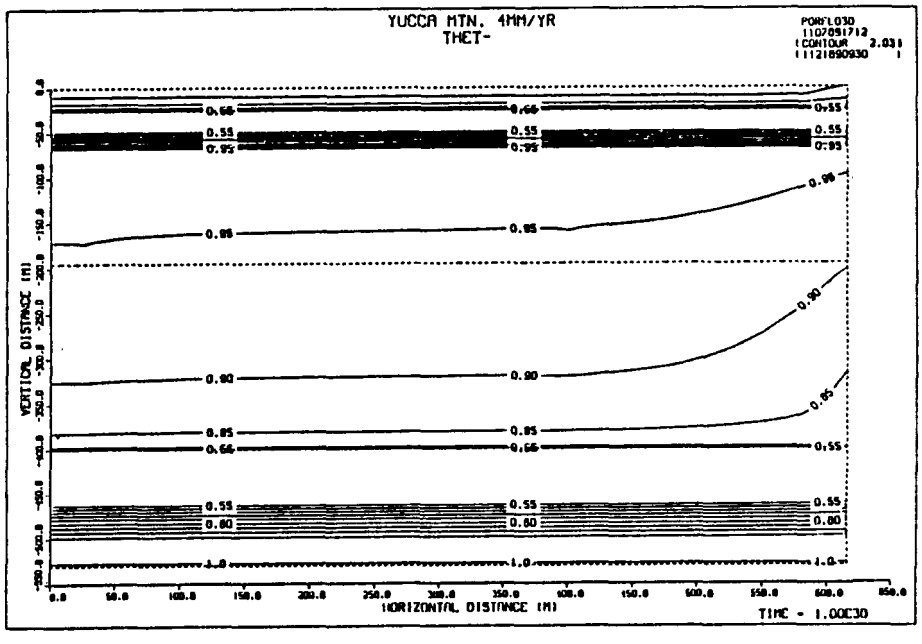

Figure 5-34. Relative Saturation at a Vertical Cross Section Through ES-1 (steady-state simulation with a 4-mm/yr recharge rate).

In Figure 5-35, a horizontal cross section of relative saturations through the proposed repository horizon (z-plane number 21) is shown. The relative saturation at this level (310-m depth in TSw2-3) has increased from an initial value of 0.65 up to a maximum of approximately 0.84. Again, no distinct patterns showing the effects of the ESF or Ghost Dance fault are evident from this section.

Figure 5-36 shows Darcy velocity vectors through the same vertical cross section shown in Figure 5-34 (y-plane number 7). No distinct patterns showing the effects of the shafts or drifts, or their associated MPZs, are evident. This steady-state solution does, however, indicate significant lateral flow above the interface between the PTn and TSw1 units. This lateral flow is consistent with the results of Rulon et al.(1986), and Wang and Narasimhan (1988), who show a potential for significant lateral flow above the repository horizon using two-dimensional cross sectional flow models.

Darcy velocity vectors in a horizontal cross section through the TCw unit (z-plane number 50) are shown in Figure 5-37. The effect of the shafts on the flow field above the interface with the PTn unit is evident from the circular pattern of the vectors around the cells in which the shafts are embedded. This figure also indicates significant lateral flow out of the model domain. These vectors represent scaled velocities so that relative, rather than absolute, differences in magnitude are shown.

Figure 5-38 shows a horizontal cross section of Darcy velocity vectors through the repository horizon (TSw2-3) at the 310-m depth. No effects of the shafts or drifts are evident. These figures imply that the fluxes at the repository level are much lower than the recharge flux of 4 mm/yr. This result is expected because of the lateral diversion of the vertical fluxes at material interfaces above the repository horizon. Estimates by Montazer and Wilson (1984) suggest that the average percolation flux within much of the TSw unit is probably less than 0.5 mm/yr.

Figure 5-39 depicts a plot of matrix saturation versus depth at steady-state condition. This profile extends vertically from the ground surface to the water table along the plane of the Ghost Dance fault, near the middle (N-S) of the model domain. The relative saturation in the upper part of unit TSw1 has increased from an initial value of 0.65 to approximately 0.96. This relative saturation decreases almost linearly with depth through unit TSw2-3. The relative saturation in the lower part of unit TSw2-3, just above the interface with unit CHn, has increased from an initial value of 0.65 to 0.82.

Figures 5-40 and 5-41 are plots of relative saturation versus depth through the same y-plane shown in Figure 5-39, but along lines through the middle (E-W) of the model domain and through ES-1, respectively. The relative saturations along these vertical axes are nearly identical to those shown in Figure 5-39. The maximum relative saturation in unit TSw1 also is approximately 0.96.

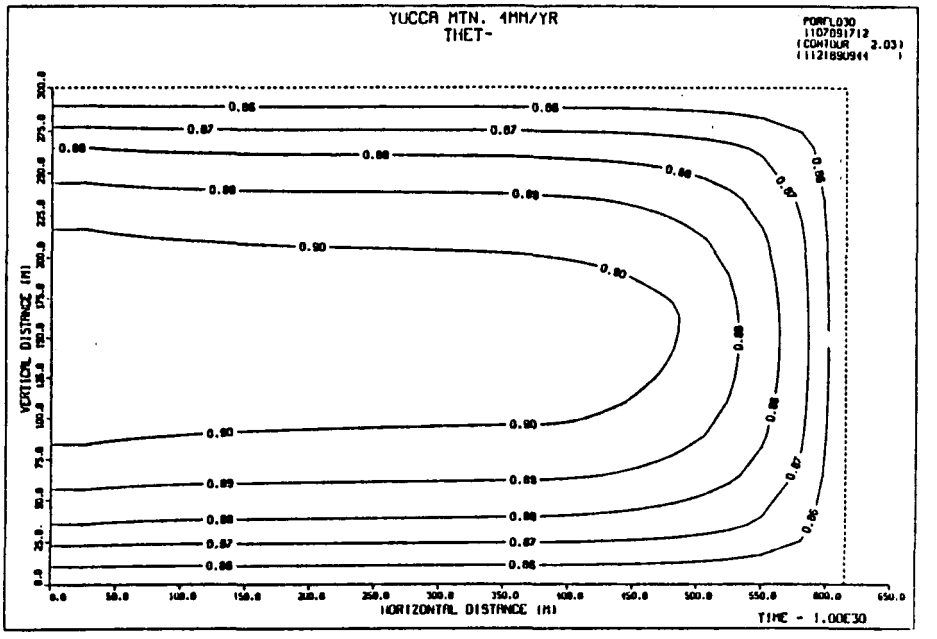

Figure 5-35. Relative Saturation at a Horizontal Cross Section Through the Repository Horizon (steady-state simulation with a 4-mm/yr recharge rate).

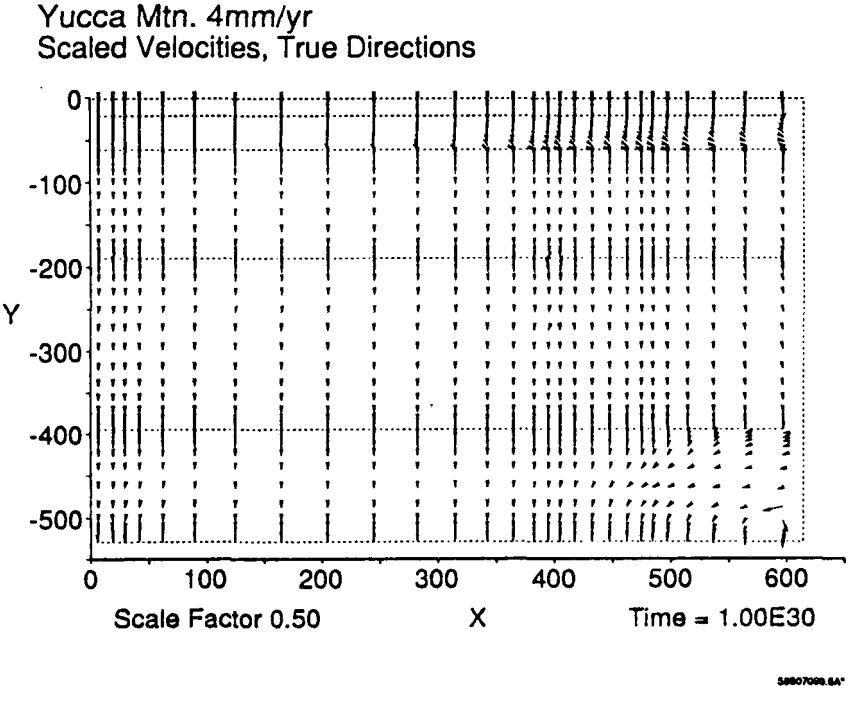

Figure 5-36. Darcy Velocities at a Vertical Cross Section Through ES-1 (steady-state simulation with a 4-mm/yr recharge rate).

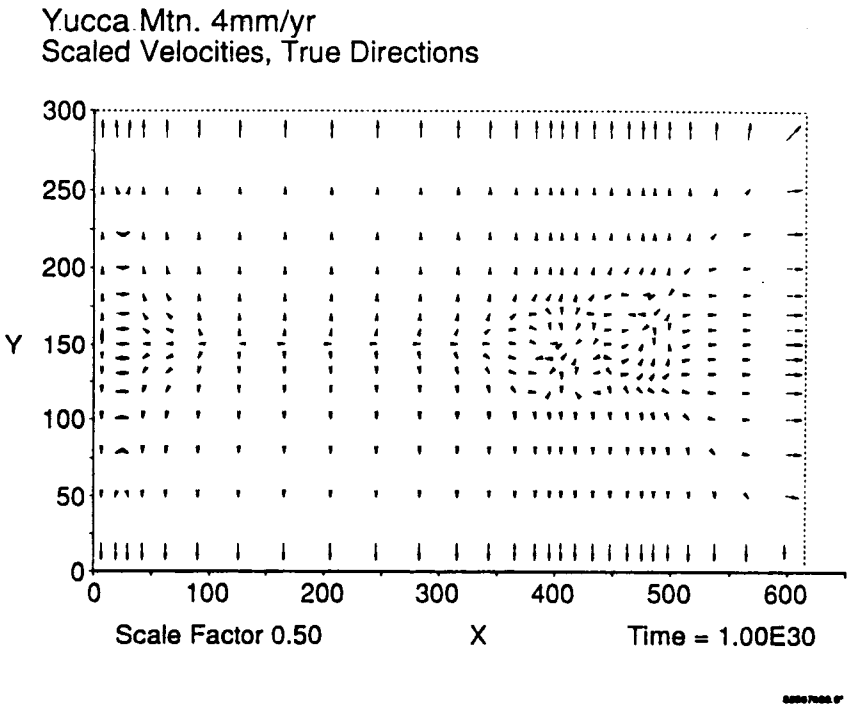

Figure 5-37. Darcy Velocities at a Horizontal Cross Section Through the Tiva Canyon Tuff Unit (steady-state simulation with a 4-mm/yr recharge rate).

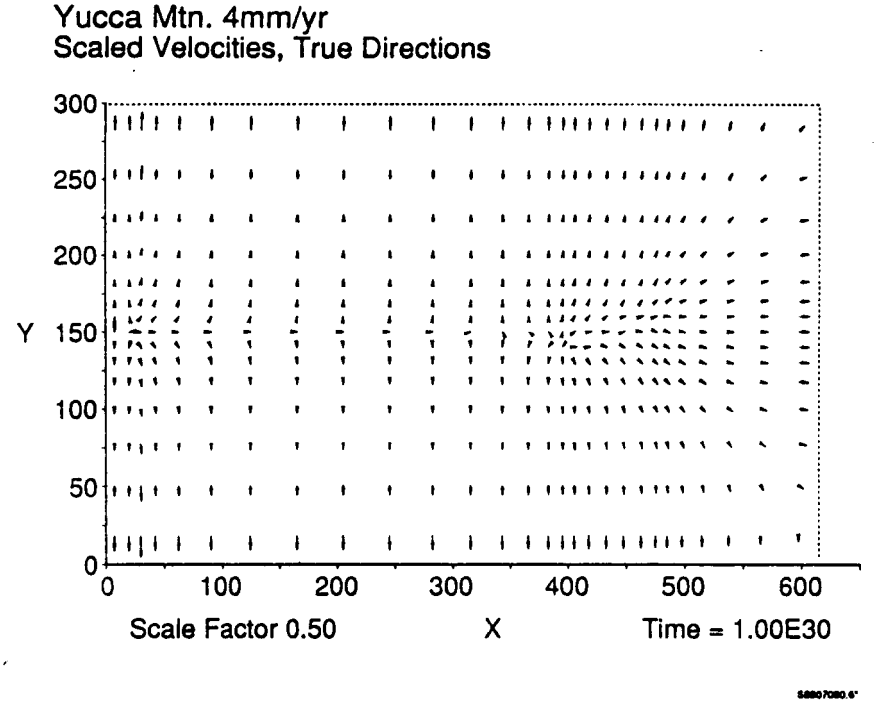

Figure 5-38. Darcy Velocities at a Horizontal Cross Section Through the Repository Horizon-Topopah Springs Tuff Unit (steady-state simulation with a 4-mm/yr recharge rate).

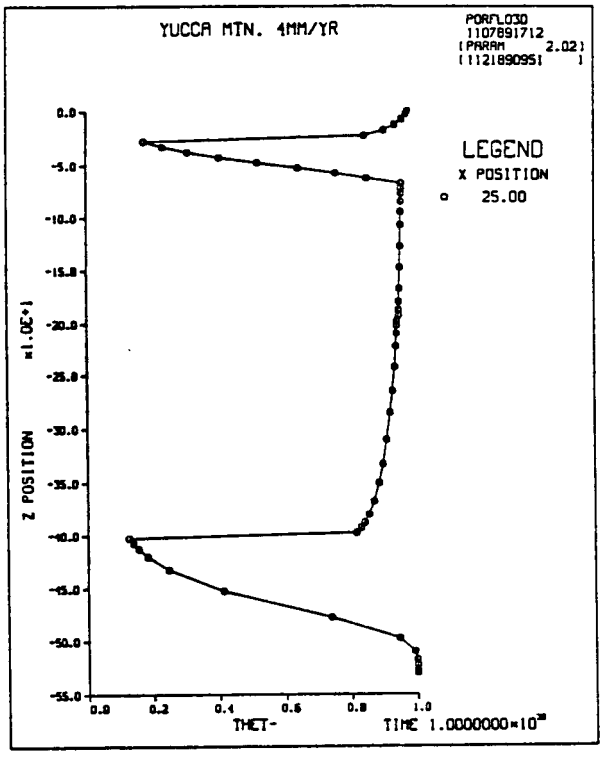

Figure 5-39. Relative Saturation Along a Vertical Axis in the Ghost Dance Fault for Steady-State Simulations with a 4-mm/yr Recharge Rate.

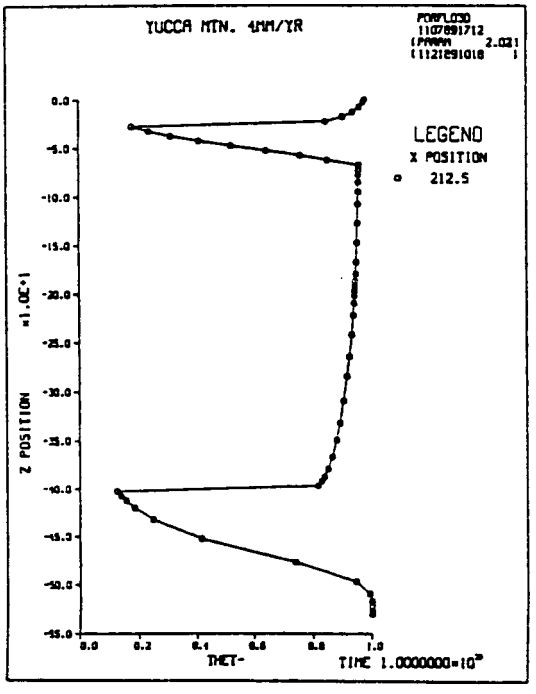

Figure 5-40. Relative Saturation Along a Vertical Axis in the Middle of Model Domain for Steady-State Simulations with a 4-mm/yr Recharge Rate.

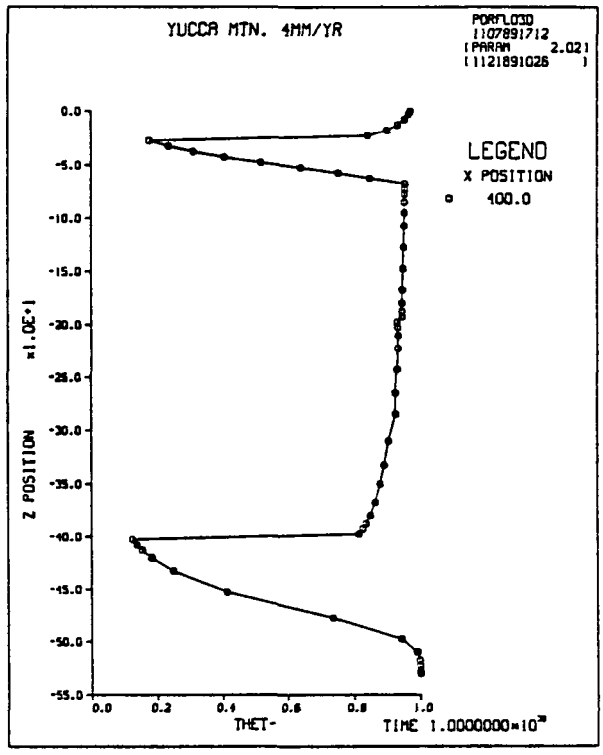

Figure 5-41. Relative Saturation Along a Vertical Axis in the ES-1 for Steady-State Simulations with a 4-mm/yr Recharge Rate.

At a relative saturation of approximately 0.984, the matrix of units TSw1 and TSw2-3 would become nearly saturated and significant amounts of fracture water would begin to exist. The relative conductivity curve shown in Figure 5-31B, indicates that water is still essentially immobile in the fractures at this saturation. Therefore, the results of these simulations suggest that if any fracture flow occurs in unit TSw1, it will be damped with depth so that no fracture flow will occur within unit TSw2-3 at a recharge rate of 4 mm/yr.

This result is different from the reported results of one-dimensional simulations, which show the TSw units to be saturated at steady-state conditions for recharge rates of 1 and 4 mm/yr (Dudley et al. 1988). Because one-dimensional models exclude the possibility of lateral flow, these should be expected to predict higher relative saturations than multi-dimensional models.

5.2.5.2 Transient Simulations. The primary objective of this study was to illustrate the effects of the ESF on the moisture distribution at Yucca Mountain, with emphasis on short-term characterization work at the repository level. However, transient simulations were also performed, using a time-varying recharge rate. The surface boundary flux for these transient simulations was changed so that a recharge rate corresponding to 4 mm/yr in 4 m (the rainy season) alternated with no recharge for 8 months. This seasonal recharge was maintained for a 20-yr simulation period.

The hydraulic properties discussed earlier were used for the transient simulations. No modifications to the saturated hydraulic conductivity of unit TCw were necessary for the transient case.

Transient relative saturations are presented in Figures 5-42 through 5-44. The relative saturations are plotted as functions of depth along the same contour lines for which steady-state solutions are shown in Figures 5-39 through 5-41. Figure 5-44 represents relative saturation profiles for ES-1 at times of 120 days (4 m) and 7305 days (20 yr). At the end of 20 yr, the relative saturation in the lower part of unit TCw, directly above the interface with unit PTn, increased from an initial value of 0.67 to approximately 0.85. The relative saturation of unit PTn decreased in the upper part of the unit and increased in the lower part of the unit in response to the pressure gradients. The relative saturation at the top of unit TSw1 increased from an initial value of 0.65 to a maximum of approximately 0.96. This saturation level decreases with depth so that the rest of unit TSw1 and all of unit TSw2-3 essentially remain at the initial saturation level of 0.65.

5.2.6 Summary of the Second Application Example

The exploratory shafts and drifts and the Ghost Dance fault are included as one- and two-dimensional features, respectively. While these features are assumed to have their own distinct properties, they are

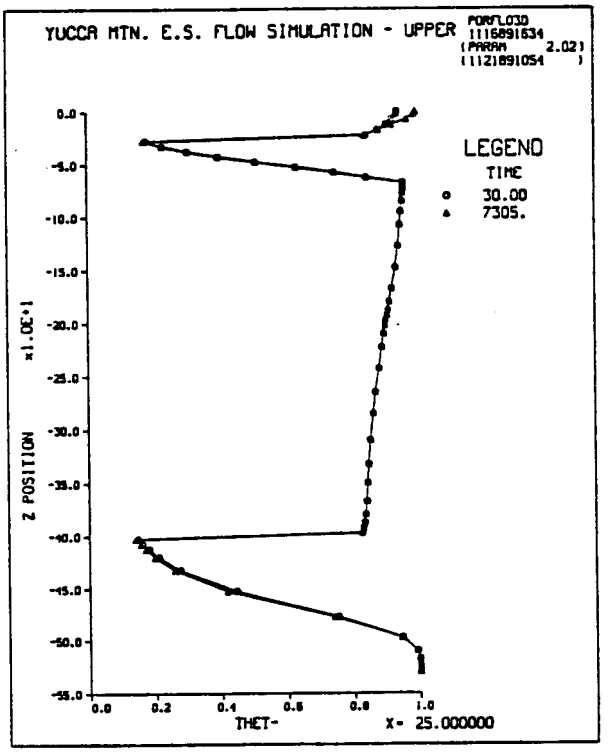

Figure 5-42. Relative Saturation Along a Vertical Axis in the Ghost Dance Fault for Transient Simulations with a 4-mm/yr Recharge Rate.

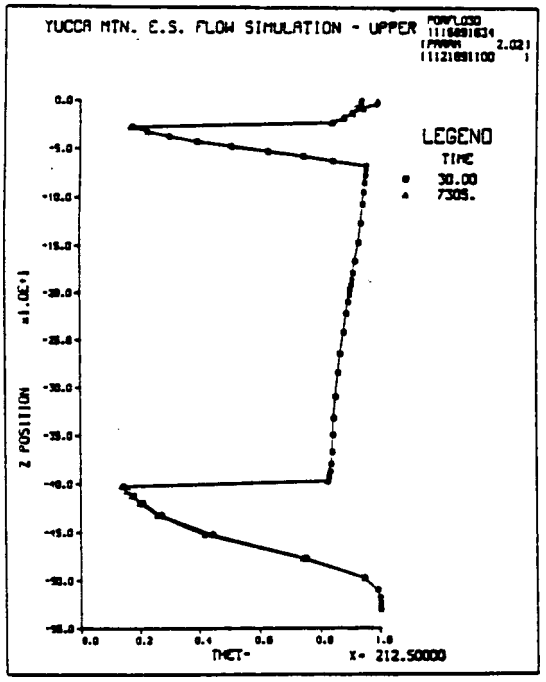

Figure 5-43. Relative Saturation Along a Vertical Axis in the Middle of Model Domain for Transient Simulations with a 4-mm/yr Recharge Rate.

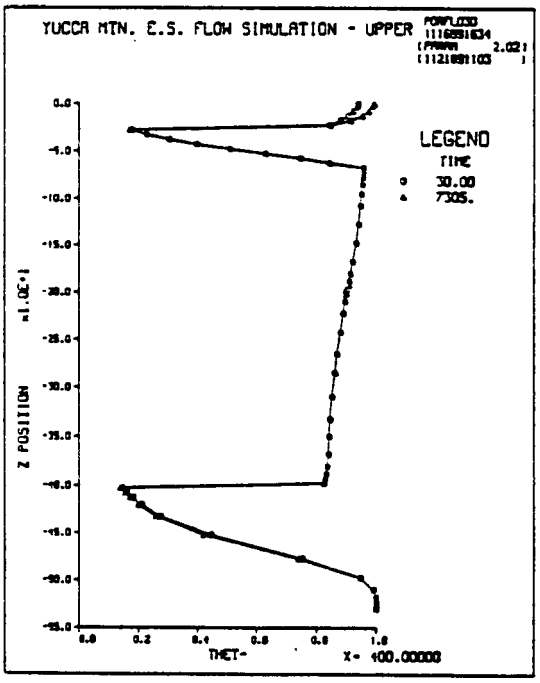

Figure 5-44. Relative Saturation Along a Vertical Axis in the ES-1 for Transient Simulations with a 4-mm/yr Recharge Rate.

nevertheless embedded in three-dimensional calculational elements. An additional limitation in this model is that these features must be aligned with the grid surfaces.

The basic assumption in this formulation in which one- and two-dimensional features are included in three-dimensional calculational domains is that the pressure values at grid nodes are common, for example, to a fracture and the adjoining rock. Thus, within an element, there is no transfer of fluid between the fracture and the rock. Such a transfer occurs only at element boundaries. As a result, calculated pressure values are not as accurate close to a fracture as they would be if the fracture was included as a full three-dimensional element. On the other hand, including a fracture or shaft as a three-dimensional element would be computationally expensive. Given the lack of data regarding properties of faults and MPZs, and the comparatively large calculational domain of the model, the results presented here should be reasonable.

These simulations suggest that fracture flow, as approximated by the equivalent continuum model (i.e., when hydrologic properties are represented, as in Figures 5-29 to 5-33), does not occur at the level of the proposed repository (i.e., in the Topopah Springs unit) even when the recharge rate is 4 mm/yr. This result is because of the three-dimensional nature of the flow field such that water can exit from the model domain through the lateral boundaries.

The results of the transient simulations reported here indicate that there will be no appreciable change in the moisture content distribution at the level of the proposed repository within 20 yr after the construction of the ESF.

5.3 VERIFICATION AND BENCHMARK TESTING OF PORFLO-3

The applications presented in Sections 5.1 and 5.2 illustrate the use of PORFLO-3 but do not represent its systematic testing. The need for systematic testing of computer programs arises from the fact that mathematical models and their resulting computer programs represent only approximately the actual behavior of the real system that they seek to represent. The assumptions that the porous medium and the migrating fluid are continua are fundamental to the derivation of the governing equations of PORFLO-3 and other such programs.

The stationary nature of the solid particles, the negligibility of the variation of the fluid density and viscosity due to pressure changes, omission of inertia terms that are implicit in the application of Darcy's law, instantaneous thermal equilibrium between fluid and solids, and the linear Freundlich isotherm distribution of species are some of the other important assumptions made in the derivation of governing equations, which form the basis of PORFLO-3. There are various reasons why these assumptions are made. These include a lack of precise knowledge about system behavior, insufficient field data for defining the parameters of a more complex model, and limitations imposed by the size and speed of the host computer. For obvious reasons, reality cannot be represented perfectly in a model.

As stated by Gleick (1987), "Only the most naive scientist believes that the perfect model is the one that perfectly represents reality. Such a model would have the same drawbacks as a map as large and detailed as the city it represents, a map depicting every park, every street, every building, every tree, every pothole, its specificity would defeat its purpose--to generalize and abstract." Yet for the model to serve its purpose, there has to be the belief that, for the problem under consideration, these assumptions do not affect the model results in an unacceptable way. Part of this belief may be based on physical reasoning and part on empirical factors.

In addition to the assumptions made in arriving at the governing equations, further assumptions are required in obtaining the numerical solution. These include discretization in space and time, approximation of media of arbitrary heterogeneity by elements of geometrically regular shapes, and an a priori assumption on the shape of the profile for the state variable. The finiteness of the "word" size of the computer on which all the arithmetic operations are performed also introduces what are known as "roundoff and truncation" errors.

The mathematical model described in Chapter 3.0 is implemented in the form of a computer program. The program dictates the logic and incorporates all the decision making required during computations. Before using the program for predictive purposes, it should be ensured by suitable tests that the cumulative effect of all the assumptions is acceptably small and that the program is free from any logic errors. Because PORFLO-3 is complex and, depending on the user-selected options, performs at various levels, no single problem can test all aspects of the program. Therefore, the premise of the testing is based on devising a number of problems, each one testing some aspect of the model.

The effect of the discretization and other assumptions made for obtaining the numerical solution is checked by comparing the model results with analytic solutions. This aspect of testing is called model verification. By comparing the output of a particular program with output from other independently developed programs, the correctness of complex logic can be checked. This process is known as benchmark testing. The size of the cumulative effect of all the assumptions only can be checked by comparing the model output against data from controlled experiments and actual site measurements. This last aspect, perhaps the most difficult, forms part of model validation.

PORFLO-3 will be verification and benchmark tested by an independent third party. Reports on these tests will be published separately.

6.0 REFERENCES

Abriola, L. M., 1984, "Multiphase Migration of Organic Compounds in a Porous Medium, A Mathematical Model," *Lecture Notes in Engineering*, C. A. Brebbia and S. A. Orszag (eds.), Springer-Verlag, New York, New York.

AEC-RL, 1973, *Report on the Investigation of the 106-T Tank Leak at the Hanford Reservation, Richland, Washington*, TID 26431, Atomic Energy Commission, Richland, Washington.

Ames, L. L. and D. Rai, 1978, *Radionuclide Interactions with Soil and Rock Media*, PB-292 460, U.S. Department of Commerce, National Technical Information Service, Springfield, Virginia.

ARHCO, 1973, *241-T-106 Tank Leak Investigation*, ARH-2874, Atlantic Richfield Hanford Company, Richland, Washington.

Averjanov, S. F., 1950, "About Permeability of Subsurface Soils in Case of Incomplete Saturation," *Eng. Collect.*, Vol. 7.

Bear, J., 1972, *Dynamics of Fluids in Porous Media*, American Elsevier, New York, New York.

Bird, R. B., W. E. Stewert, and E. N. Lightfoot, 1960, *Transport Phenomena*, John Wiley & Sons, Inc., New York, New York.

Bjornstad, B. N., 1985, "Late-Cenozoic Stratigraphy and Tectonic Evolution Within a Subsiding Basin, South-Central Washington," *Geological Society of America Abstracts with Program*, Vol. 17, No. 7, p. 524.

Brooks, R. H. and A. T. Corey, 1966, "Properties of Porous Media Affecting Fluid Flow," *Journal of Irrigation and Drainage Division*, American Society of Civil Engineers, Vol. 92, 3 (IR2), pp. 61-88.

Brutsaert, W., 1967, "Some Methods of Calculating Unsaturated Permeability," *Transactions of American Society of Agricultural Engineers*, Vol. 10, pp. 400-404.

Burdine, N. T., 1953, "Relative Permeability Calculations from Pore-Size Distribution Data," *Petroleum Trans.*, American Institute of Mining and Metallurgical Engineering, Vol. 198, pp. 71-77.

Buretta, R. J., 1972, *Thermal Convection in a Fluid Filled with Uniform Internal Heat Sources*, Ph.D. dissertation, Mechanical Engineering Department, University of Minnesota, University Microfilms International, Ann Arbor, Michigan.

Case, J. B. and P. C. Kelsall, 1987, *Modification of Rock Mass Permeability in the Zone Surrounding a Shaft in Fractured, Welded Tuff*, SAND86-7001, Sandia National Laboratories, Albuquerque, New Mexico.

Cheng, P., 1978, "Heat Transfer in Geothermal Systems," *Advances in Heat Transfer*, Academic Press, New York, New York, Vol. 14, pp. 1-105.

Childs, E. C. and N. Collis-George, 1950, "The Permeability of Porous Materials," *Proceedings of Royal Society*, Series A, Vol. 201, pp. 392-405.

Clifton, P. M., 1986, *Groundwater Travel Time Analysis for the Reference Repository Location at Hanford Site*, SD-BWI-TI-303, Rockwell Hanford Operations, Richland, Washington.

COE, 1970, *Columbia River, Washington: Water Surface Profiles RM 323 to RM 395*, U.S. Army Corps of Engineers, Seattle, Washington.

Coles, D. G. and L. D. Ramspott, 1982, "Migration of Ruthenium-106 in a Nevada Test Site Aquifer: Discrepancy Between Field and Laboratory Results," *Science*, Vol. 215.5, pp. 1235-1236.

DOE, 1988, *Site Characterization Plan, Reference Repository Location, Hanford Site, Washington, Consultation Draft*, Vol. 2, Chapter 3, DOE/RW-0164, U.S. Department of Energy, Office of Civilian Radioactive Waste Management, Washington, D.C.

DOE, 1989, *Site Characterization Plan, Yucca Mountain Site, Nevada Research and Development Area, Nevada*, Volume VIII, Part B., U.S. Department of Energy, Washington, D.C.

Dudley, A. L., R. R. Peters, J. H. Gauthier, M. L. Wilson, M. S. Tierney, and E. A. Klavetter, 1988, *Total System Performance Assessment Code (TOSPAC) Volume 1: Physical and Mathematical Bases*, SAND85-0002, Sandia National Laboratories, Albuquerque, New Mexico.

Ecology, EPA, and DOE, 1989, *Hanford Federal Facility Agreement and Consent Order*, Washington State Department of Ecology, U.S. Environmental Protection Agency, and U.S. Department of Energy, Olympia, Washington.

Eyler, L. L. and M. J. Budden, 1984, *Verification and Benchmarking of PORFLO: An Equivalent Porous-Continuum Code for Repository-Scale Analysis*, PNL-5044, Pacific Northwest Laboratory, Richland, Washington.

Fayer, M. J., G. W. Gee, and T. L. Jones, 1986, *UNSAT-H Version 1.0: Unsaturated Flow Code Documentation and Applications for the Hanford Site*, PNL-5899, Pacific Northwest Laboratory, Richland, Washington.

Fecht, K. R. and W. H. Price, 1977, *Granulometric Data 241-T Tank Farm Monitoring Well Sediments*, RHO-LD-19 Informal Report, Rockwell Hanford Operations, Richland, Washington.

Fernandez, J. A., T. E. Hinkebein, and J. B. Case, 1988, *Analyses to Evaluate the Effect of the Exploratory Shaft on Repository Performance of Yucca Mountain*, SAND85-0598, Sandia National Laboratories, Albuquerque, New Mexico.

Freeze, R. A. and J. A. Cherry, 1979, *Groundwater*, Prentice-Hall, Englewood Cliffs, New Jersey.

Gee, G. W., 1987, *Recharge at the Hanford Site: Status Report*, PNL-6403, Pacific Northwest Laboratory, Richland, Washington.

Gee, G. W., M. L. Rockhold, and J. L. Downs, 1988, *Status of FY 1988 Soil-Water Balance Studies on the Hanford Site*, PNL-6750, Pacific Northwest Laboratory, Richland, Washington.

Gephart, R. E., R. C. Arnett, R. G. Baca, L. S. Leonhart, and F. A. Spane, Jr., 1979, *Hydrologic Studies within the Columbia Plateau, Washington; An Integration of Current Knowledge*, RHO-BWI-ST-5, Rockwell Hanford Operations, Richland, Washington.

Gillette, R., 1973, "Radiation Spill at Hanford: The Anatomy of an Accident," *Science*, Vol. 181, pp. 728-730.

Gleick, J., 1987, *Chaos, Making a New Science*, Viking Press.

Goltz, M. N. and P. Roberts, 1988, "Simulations of Physical Nonequilibrium Solute Transport Models: Application to a Large-Scale Experiment," *Journal of Contaminant Hydrology*, Vol. 3, pp. 37-63.

Gosman, A., W. Pun, A. K. Runchal, D. B. Spalding, and M. Wolfshtein, 1969, *Heat and Mass Transfer in Recirculating Flows*, Academic Press, London.

Hageman, L. and D. Young, 1981, *Applied Iterative Methods*, Academic Press, New York.

Hassanizadeh, S. M., 1986a, "Derivation of Basic Equations of Mass Transport in Porous Media, Part 1., Macroscopic Balance Laws," *Advances in Water Resources*, Vol. 9, pp. 196-206.

Hassanizadeh, S. M., 1986b, "Derivation of Basic Equations of Mass Transport in Porous Media, Part 2., Generalized Darcy's and Fick's Law," *Advances in Water Resources*, Vol. 9, pp. 207-222.

Huyakorn, P. S. and G. F. Pinder, 1983, *Computational Methods in Subsurface Flow*, Academic Press, Inc., New York.

Jennings, A., 1977, *Matrix Computations for Engineers and Scientists*, John Wiley & Sons, New York.

Kincaid, D. R., J. R. Respess, D. M. Young, and R. G. Grimes, 1982, "ITPACK 2C: A Fortran Package for Solving Large, Sparse Linear Systems by Adaptive Accelerated Iterative Methods," *ACM Transactions on Mathematical Software*, Vol. 8, No. 3, pp. 302-322.

Klavetter, E. A. and R. R. Peters, 1986, *Fluid Flow in a Fractured Rock Mass*, SAND85-0855, Sandia National Laboratories, Albuquerque, New Mexico.

Kline, N. W., A. K. Runchal, and R. G. Baca, 1983, *PORFLO Computer Code: User's Guide*, RHO-BW-CR-138P, Rockwell Hanford Operations, Richland, Washington.

Lindberg, J. W., 1986, *Width and Infilling of Fractures in Four Grande Ronde Basalt Flows Beneath the Reference Repository Location*, SD-BWI-TI-282, Rockwell Hanford Operations, Richland, Washington.

Leonhart, L. S., R. J. Jackson, D. L. Graham, L. W. Gelhar, G. M. Thompson, B. Y. Kanihiro, and C. R. Wilson, 1985, "Analysis and Interpretation of a Recirculating Tracer Experiment Performed on a Deep Basalt Flow Top," *Bulletin of the Association of Engineering Geologists*, Vol. XXIII, No. 3, pp. 259-274.

Long, P. E. and WCC, 1984, *Repository Horizon Identification Report*, SD-BWI-17-001, Rockwell Hanford Operations and Woodward Clyde Consultants, Richland, Washington.

McGhan, V. L., P. J. Mitchell, and R. S. Argo, 1985, *Hanford Wells*, PNL-5397, Pacific Northwest Laboratory, Richland, Washington.

Montazer, P. and W. E. Wilson, 1984, *Conceptual Hydrologic Model of Flow in the Unsaturated Zone, Yucca Mountain, Nevada*, Water-Resources Investigations Report 84-4345, U.S. Geological Survey, Denver, Colorado.

Mualam, Y., 1976, "A New Model for Predicting the Hydraulic Conductivity of Unsaturated Porous Media," *Water Resources Research*, Vol. 12, No. 3, pp. 513-522.

Murthy K. S., L. A. Stout, B. A. Napier, A. E. Reisenauer, and D. K. Landstrom, 1983, *Assessment of Single-shell Tank Residual Liquid Issues at Hanford Site, Washington*, PNL-4688, Pacific Northwest Laboratory, Richland, Washington.

Patankar, S. V., 1980, *Numerical Heat Transfer and Fluid Flow*, McGraw-Hill, New York, New York.

Perry, R. H. and C. H. Chilton, 1973, *Chemical Engineers' Handbook*, 5th ed, McGraw Hill, New York, New York.

Peters, R. R., J. H. Gauthier, A. L. Dudley, 1986, *The Effect of Percolation Rate on Water-Travel Time in Deep, Partially Saturated Zones*, SAND85-0854, Sandia National Laboratories, Albuquerque, New Mexico.

Price, W. H. and K. R. Fecht, 1976, *Geology of the 241-T Tank Farm*, ARH-LD-135, Atlantic Richfield Hanford Company, Richland, Washington.

Reid, J., 1981, "The Use of Conjugate Gradients for Systems of Linear Equations Possessing Property A," *SIAM Journal of Numerical Analysis*, Vol. 9, pp. 325-332.

Routson, R. C. and K. R. Fecht, 1979, *Soil (Sediment) Properties of Twelve Hanford Wells with Geologic Interpretation*, RHO-LD-82, Rockwell Hanford Operations, Richland, Washington.

Routson, R. C., W. H. Price, D. J. Brown, and K. R. Fecht, 1979, *High-Level Waste Leakage from the 241-T-106 Tank at Hanford*, RHO-ST-14, Rockwell Hanford Operations, Richland, Washington.

Rulon, J., G. S. Bodvarsson, and P. Montazer, 1986, *Preliminary Numerical Simulations of Groundwater Flow in the Unsaturated Zone, Yucca Mountain, Nevada*, LBL-20553, Lawrence Berkeley Laboratory, Berkeley, California.

Runchal, A. K., 1969, *Transfer Processes in Steady Two-Dimensional Separated Flows*, Ph.D. dissertation, London University, U.K.

Runchal, A. K., 1972, "Convergence and Accuracy of Three Finite Difference Schemes for a Two-Dimensional Conduction and Convection Problem," *International Journal of Numerical Methods in Engineering*, Vol. 4, p. 541-550.

Runchal, A. K. and B. Sagar, 1989, *PORFLO-3: A Mathematical Model for Fluid Flow, Heat, and Mass Transport in Variably Saturated Geologic Media - Users Manual, Version 1.0*, WHC-EP-0041, Westinghouse Hanford Company, Richland, Washington.

Runchal, A. K., B. Sagar, R. G. Baca, and N. W. Kline, 1985, *PORFLO - A Continuum Model for Fluid Flow, Heat Transfer, and Mass Transport in Porous Media*, RHO-BW-CR-150P, Rockwell Hanford Operations, Richland, Washington.

Sagar, B. and A. K. Runchal, 1982, "Permeability of Fractured Rock: Effect of Fracture Size and Data Uncertainties," *Water Resources Research*, Vol. 18, No. 2, pp. 266-274.

Scheidegger, A. E., 1961, "General Theory of Dispersion in Porous Media," *Journal of Geophysical Research*, Vol. 66, pp. 3273-3278.

Scott, R. B. and J. Bonk, 1984, *Preliminary Geologic Map of Yucca Mountain with Geologic Sections, Nye County, Nevada*, U.S. Geological Survey Open-File Report 84-494, scale 1:12,000.

Scott, R. B., R. W. Spengler, A. R. Lappin, and M. P. Chornack, 1983, "Geologic Character of Tuffs in the Unsaturated Zone at Yucca Mountain, Southern Nevada," *Role of the Unsaturated Zone in Radioactive and Hazardous Waste Disposal*, J. Mercer (ed.), Ann Arbor Science, Ann Arbor, Michigan.

Snow, D. T., 1969, "Anisotropic Permeability of Fractured Media," *Water Resources Research*, Vol. 5, No. 6, pp. 1273-1289.

Spalding, D. B., 1972, "A Novel Finite-Difference Formulation for Differential Expressions Involving Both First and Second Derivatives," *Int. J. Num, Methods Eng.*," Vol. 4, p. 551-559.

Spry, A., 1962, "The Origin of Columnar Jointing, Particularly in Basalt Flows," *Geological Society of Australia Journal*, Vol. 8, pp. 191-216.

Sublette, W. R., 1983, *Rock Mechanics Data Package*, SD-BWI-DP-041, Rockwell Hanford Operations, Richland, Washington.

Sudicky, E. A. and E. O. Frind, 1982, "Contaminant Transport in Fractured Porous Media: Analytic Solutions for a System of Parallel Fractures," *Water Resources Research*, Vol. 18, No. 6, pp. 808-820.

Swanson, D. A., T. L. Wright, P. R. Hooper, and R. D. Bentley, 1979, *Revision in Stratigraphic Nomenclature of the Columbia River Basalt Group*, Bulletin 1457, U.S. Geological Survey, Washington, D.C.

Van Genuchten, R., 1978, *Calculating the Unsaturated Hydraulic Conductivity With a New Closed-Form Analytic Model*, Report 78-WR-08, Water Resources Program, Department of Civil Engineering, Princeton University, Princeton, New Jersey.

Waitt, R. B., Jr, 1980, "About Forty Last-Glacial Lake Missoula Jokulhlaups Through Southern Washington," *Journal of Geology*, Vol. 88, pp. 653-679.

Wang, J. S. Y. and T. N. Narasimhan, 1988, "Hydrologic Mechanisms Governing Fluid Flow in a Partially Saturated, Fractured, Porous Medium," *Water Resources Research*, Vol. 21, No. 2, pp. 1861-1874.